UNIVERSITÀ DEGLI STUDI DI TRIESTE
Sede Amministrativa del Dottorato di Ricerca

XX CICLO DEL
DOTTORATO DI RICERCA IN FISICA

Generation of VUV ultra-short coherent optical pulses using electron storage rings

(Settore scientifico-disciplinare FIS/03)

DOTTORANDO
Francesca Curbis

COORDINATORE DEL COLLEGIO
DEI DOCENTI
Chiar.mo Prof. Gaetano Senatore
Università degli Studi di Trieste

RELATORE
Chiar.mo Prof. Giovanni De Ninno
Università degli Studi di Nova Gorica

TUTORE
Chiar.mo Prof. Alfonso Franciosi
Università degli Studi di Trieste

April, 7 2008

Generation of VUV ultra-short coherent optical pulses using electron storage rings

Francesca Curbis

April, 7 2008

Abstract

The need of coherent and intense pulsed radiation is spread among many research disciplines, such as biology, nanotechnology, physics, chemistry and medicine. The synchrotron light from traditional sources only partially meets these characteristics. A new kind of light source has been conceived and developed in the last decades: the Free-Electron Laser (FEL).

The FEL process relies on the interaction between a relativistic electron beam and an electromagnetic wave in presence of a static and periodic magnetic field, produced by a device called undulator. This interaction generates coherent radiation at a fundamental frequency and its higher harmonics. In the standard configuration, the electron beam is generated by a linear accelerator and the interaction occurs in a single passage through one or several undulators. An alternative configuration can be obtained if the electrons are supplied by a storage ring.

This work has been carried out at the Elettra laboratory within the "new light sources" group. My thesis focuses on both numerical and experimental issues about the generation of coherent harmonics on storage-ring FELs.

The Elettra SRFEL has been originally designed to operate in "oscillator configuration" where the radiation is stored in an optical cavity (made of two mirrors). This process also drives the emission of radiation in the harmonics. In this work, different experimental methods have been implemented at Elettra to concentrate the power in giant pulses, both for the fundamental wavelength and its harmonics. Using this technique, it has been possible to generate fundamental radiation at 660 nm and 450 nm with (intra-cavity) power of few mJ and third harmonic radiation at 220 nm and 150 nm with few nJ of power. This process has been studied numerically by using a tri-dimensional simulation which also accounts for the re-circulation of the beam. The results of simulations are in good agreement with experimental measurements and allow to investigate the inner structure of the light below the picoseconds scale, where the instrumentation resolution reaches its limit. Structures of hundreds of femtoseconds inside the laser pulse have been found and this implies a higher peak power. Moreover, the numerical results have been confirmed by spectral measurements.

By removing the optical cavity and focusing an external laser in the first undulator, a "seeded single-pass" configuration has been implemented. In the first undulator, the interaction with the external laser ("seed") modulates the electron energy which is converted to spatial modulation ("bunching"). A Fourier analysis of the bunched electron-beam shows the presence of components at all harmonics (even and odd) and this explains why electrons in the second undulator can emit at any harmonic.

To implement this configuration a design and layout plus tri-dimensional simulations were performed. Followed by the installation of the seed laser (Ti:Sapphire, $\lambda = 796\,\mathrm{nm}$), the

timing and the diagnostics. The commissioning focused on optimizing the spatial overlap and the synchronization between the electrons and the seed laser. Coherent harmonic radiation has been obtained at 265 nm, the third harmonic of the seed laser. After the characterization of this light, the seed frequency has been doubled by means of a nonlinear crystal. With this setup, radiation down to 99.5 nm (the fourth harmonic of the seed) has been generated. The shot-to-shot stability is comparable to the stability of the synchrotron radiation (fluctuations of few %) but the number of photons per pulse ($\sim 10^9$) is about two-three orders of magnitude bigger than the synchrotron one. Thus this coherent radiation can be used for experiments similar to those suggested for the next generation FELs.

Summarizing, the light source developed during my thesis is a unique facility able to generate coherent radiation with variable polarization, variable duration (between 100 fs and 1 ps), with peak power of the order of mega-Watts in a wide spectral VUV range.

In the latest implementation, this radiation source has been used for two different kind of experiments, one in gas-phase, the other of solid state. The obtained results demonstrate the appealing of this source for user experiments.

In perspective, there is a plan to extend the wavelength range below 100 nm and to improve the tunability of the source.

Riassunto

Vari ambiti della ricerca scientifica, dalla biologia alle nanotecnologie, passando per la fisica, la chimica e la medicina, richiedono per le loro indagini una radiazione spazialmente coerente con un elevato numero di fotoni per impulso. Poiché la radiazione di sincrotrone non possiede queste caratteristiche, negli ultimi anni gli sforzi si sono concentrati nello sviluppo delle cosiddette sorgenti di quarta generazione: i laser a elettroni liberi (LEL).

Il processo LEL avviene per l'interazione di un'onda elettromagnetica con un fascio di elettroni relativistici in presenza di un campo magnetico. Tale campo, statico e periodico, viene generato da un dispositivo detto ondulatore. L'interazione produce emissione di luce coerente ad una frequenza fondamentale e alle sue armoniche superiori. La configurazione standard prevede che gli elettroni siano prodotti da un acceleratore lineare e l'interazione si risolve tipicamente in un singolo passaggio attraverso uno o più ondulatori. Una configurazione alternativa si ottiene quando gli elettroni sono forniti da un anello di accumulazione.

La tesi si è svolta presso il laboratorio Elettra, nel gruppo che si occupa dello sviluppo di nuove sorgenti di luce. La mia attività di ricerca comprende sia aspetti teorico-numerici che sperimentali relativi alla generazione di armoniche coerenti su LEL installati su anelli di accumulazione.

Storicamente il laser a elettroni liberi ad Elettra è nato in "configurazione oscillatore" (la radiazione è immagazzinata in una cavità ottica formata da due specchi). Ad ogni passaggio successivo gli elettroni interagiscono con l'onda electtromagnetica amplificandola fino all'instaurarsi dell'effetto laser. Questo processo guida anche l'emissione alle armoniche superiori. Diversi metodi sperimentali possono essere usati per concentrare la potenza in impulsi giganti, sia per la fondamentale che per le armoniche. Questa tecnica, che ho affinato durante il mio lavoro di tesi, ci ha permesso di generare potenze dell'ordine di alcuni mJ per la fondamentale (nella cavità) e di alcuni nJ alla terza armonica di 660 nm e di 450 nm, cioè 220 nm e 150 nm rispettivamente. Dal punto di vista numerico, per studiare questo processo abbiamo modificato un codice per simulare tridimensionalmente la nostra configurazione ed abbiamo aggiunto una parte che propaga gli elettroni lungo l'anello. Le simulazioni sono in ottimo accordo con i dati sperimentali e ci permettono di investigare più nel dettaglio l'impulso, nella scala temporale dei femtosecondi dove si arresta la risoluzione strumentale. Dalle simulazioni risulta che all'interno degli impulsi laser sono presenti delle substrutture della durata di alcune centinaia di femtosecondi. La presenza di tali strutture implica una potenza di picco maggiore. Abbiamo inoltre una conferma indiretta dei risultati numerici tramite le misure spettrali.

Rimuovendo la cavità ottica e focalizzando un laser esterno nel primo ondulatore si può passare alla cosiddetta configurazione in "singolo passaggio". Nel primo ondula-

tore, l'interazione con il laser esterno ("seed") produce una modulazione nell'energia degli elettroni, la quale viene trasformata in separazione spaziale ("bunching"). Un'analisi di Fourier del fascio di elettroni mostra componenti a tutte le armoniche (pari e dispari), per cui gli elettroni sono in grado di emettere a qualsiasi armonica nel secondo ondulatore. In questa configurazione la prima parte del lavoro di tesi è stata il design della linea e lo studio numerico dei risultati attesi. A questo studio preliminare è seguita l'installazione dell'esperimento, a partire dall'alloggiamento e la messa in funzione del laser esterno (Ti:Sapphire, $\lambda = 796\,\mathrm{nm}$) fino alla realizzazione del sistema di sincronizzazione del seed con gli elettroni. Prima di ottenere la radiazione armonica coerente e poter confrontare le aspettative con i risultati sperimentali abbiamo dovuto dedicare molti turni di fisica di macchina al perfezionamento della sovrapposizione spaziale e temporale tra elettroni e laser esterno. La prima radiazione armonica coerente è stata ottenuta alla terza armonica (265 nm) del laser esterno. Dopo una prima caratterizzazione della sorgente, abbiamo introdotto un cristallo nonlineare per generare la seconda armonica del laser esterno e usare questa come seed. Attualmente il LEL di Elettra è in grado di produrre radiazione fino a 99.5 nm (la quarta armonica del seed) con la stessa stabilità della radiazione di sincrotrone (flutuazioni dell'ordine del %). Queste caratteristiche, insieme al numero di fotoni per impulso ($\sim 10^9$) che supera di almeno due ordini di grandezza l'emissione di sincrotrone, permettono l'utilizzo della luce prodotta per esperimenti simili a quelli proposti per le sorgenti di quarta generazione.

Riassumendo, la sorgente sviluppata durante la mia tesi è attualmente l'unica in grado di fornire luce coerente di durata variabile tra 100 fs e 1 ps con potenze dell'ordine del mega-Watt e polarizzazione variabile (lineare-circolare) in un ampia gamma spettrale nell'ultravioletto. Negli ultimi turni, questa radiazione è stata usata su due diversi tipi di esperimenti, uno in fase gassosa l'altro di stato solido. I risultati ottenuti dimostrano che la radiazione emessa può essere appetibile per gli utenti. Le prospettive sono estendere il range di lunghezze d'onda sotto i 100 nm e migliorare la tunabilità della sorgente.

Contents

Introduction

0.1 Light sources: from synchrotron radiation to Free Electron Lasers

Synchrotron radiation was observed for the first time in 1947. Initially accelerator physicists considered the radiation emitted by accelerated electrons mainly as a problem of energy loss. Only in the 60's it has been realized that the light produced in this way has exceptional properties (high brightness, very good collimation, full tunability, ...) that can be used to probe the structure of a wide range of matter samples.

The first generation of synchrotron light sources relied on accelerators built for high-energy or nuclear physics and worked in parasitic mode. Then the machine operation changed from a repeated sequence of injection, acceleration and extraction into a beam that continuously circulates at fixed energy for many hours (storage rings). This in turn implied an improved beam stability and higher flux of emitted radiation.

Starting from the second generation of synchrotron light sources (80's), storage rings became dedicated sources of synchrotron radiation. In fact the requirement of high flux was not compatible with the parasitic operation. Besides, the light production, initially relying on simple bending magnets, was gradually committed to undulators, i.e. array of spaced dipole magnets of alternating polarity. Undulators allow to produce radiation with different polarizations (from planar to elliptical). The spectral brightness, i.e. the flux per unit area, unit solid angle and unit spectral bandwidth, is several orders of magnitude higher than the one provided by bending magnets.

In order to take full advantage of undulator's features, the third generation of synchrotron light sources (90's and still operational) was designed with long dedicated straight sections to incorporate these devices. Specific care was taken to optimize the synchrotron magnetic lattice with the aim of increasing the brightness. The extracted radiation is characterized by a considerable degree of spatial coherence and achievable wavelengths cover the range from hard X-rays to infrared light. The production of high-energy photons is provided by machines with quite high electron beam energies (several GeV) like ESRF (Grenoble), APS (Argonne) and SPring-8 (Japan). Sources optimized to provide lower photon energies (Vacuum Ultra Violet (VUV)) wavelengths operate at electron-beam energies of few GeV. This is, e.g., the case of Elettra (Trieste) and ALS (Berkeley).

Recently, the requirement of shorter wavelengths, shorter optical pulses, higher peak brightness and full coherence led to the investigation of new possible radiation sources. This because various issues (e.g., relatively large emittances, low currents) limited the performance of synchrotrons.

Free Electron Lasers (FEL) are considered the *fourth generation light sources* [1, 2]. They can provide a peak brightness many orders of magnitude above that of third-generation

light sources.
The evolution of synchrotron light sources in terms of brightness is shown in Fig. 1

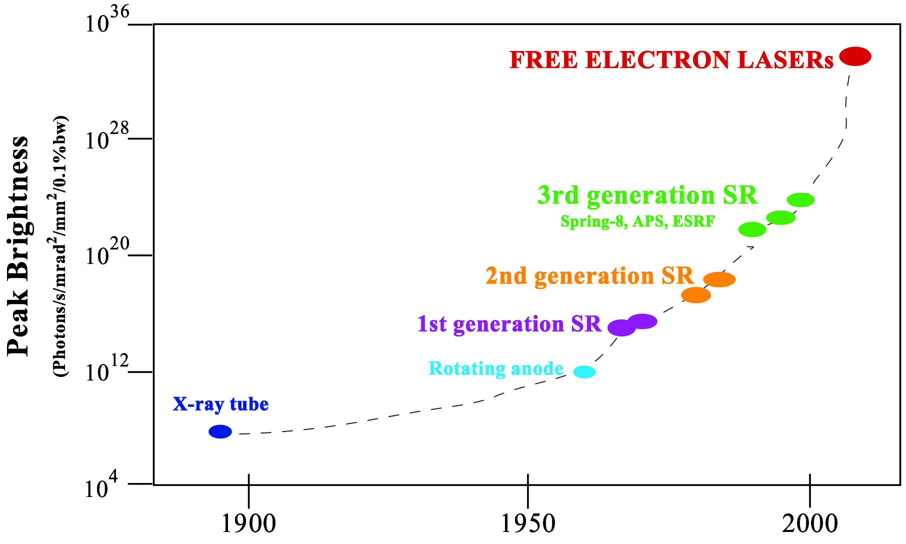

Figure 1: *Historical evolution of the peak brightness [3].*

0.2 FEL principle and generation of Coherent Harmonics

Potentially, the FEL radiation is temporally and spatially coherent, almost Fourier transform limited, has a high flux and can be tuned over a wide range of wavelengths(from angstroms to hundreds of micrometers/few millimeters). In some configurations this radiation has also a variable polarization as well as a stable temporal structure. These characteristics make the FEL suitable for applications in several domains, e.g., biology, nanotechnologies, physics, chemistry and medicine. The FEL principle relies on the stimulated emission of a relativistic electron beam propagating in the static and periodic magnetic field provided by an undulator. The wavelength of the stimulated emission is fixed by the electron beam energy and by the characteristics of the undulator field. The stimulated emission is induced when electrons interact with an electromagnetic wave that co-propagates with them through the undulator. If the wave that initiates the process (*seed*) is coherent, the electrons emit radiation which is also coherent.
In this thesis we explore the possibility of generating coherent harmonics of the electromagnetic field co-propagating with electrons. For this purpose, two different configurations have been used: the oscillator configuration and the single pass configuration. Both schemes have been implemented on the Elettra storage-ring FEL.

0.2.1 FEL configurations

Oscillator configuration

The oscillator configuration is characterized by an optical cavity that encloses the undulator (or a couple of undulators with a magnetic chicane in between, i.e., the optical klystron, see Section 1.2.2). Generally, the electron beam can be provided either by a linear accelerator or a storage ring. The first case is usually related to FELs that produce infrared radiation. The second option concerns FELs in the visible-UV range. This kind of devices have been developed since the second generation of storage-ring light sources. Figure 2 shows a storage-ring FEL in oscillator configuration.

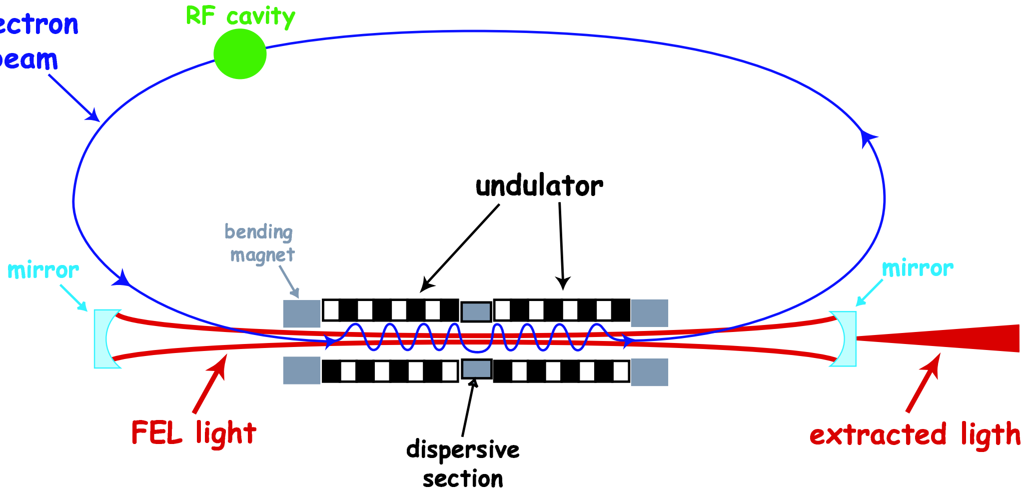

Figure 2: *SRFEL in oscillator configuration.*

The circulating electron bunches produce synchrotron radiation passing through the magnetic field provided by the optical klystron. The emitted radiation is stored into the optical cavity and amplified during many successive interactions with the electron beam until the lasing is achieved. The FEL radiation, being fully coherent, may act as a seed for the generation of high order harmonics of the fundamental wavelength which is stored in the optical cavity. These harmonics are not amplified turn after turn because they are not stored in the optical cavity. Indeed, the optical cavity mirrors have a narrow-band (few nm) high reflectivity, which is centered around the fundamental wavelength.
Since there is lack of materials with the required high reflectivity necessary to operate oscillator FELs below ∼170 nm, this kind of systems have a severe limitation in achieve very short wavelengths. Nevertheless, the possibility to produce FEL radiation at short wavelengths (VUV–X-rays) is guaranteed by *single pass* devices using the Self Amplified Spontaneous Emission (SASE) [4, 5] or the Harmonic Generation (HG) [6, 7, 8, 9, 10] from coherent seeds.

Single-pass configuration

In the SASE process (see Fig. 3) a linear accelerator (linac) provides the electrons that pass through a long (tens of meters) chain of undulators[1] The spontaneous emission produced by electrons at the entrance of the undulator couples to the beam itself and gets amplified.

SASE sources are relatively simple to implement (if compared to seeded FELs) and are characterized by very high brightness. However, they show an incoherent temporal structure, resulting from the envelope of a series of micro-pulses with random intensity

---

[1] The initial proposal was to use SASE in a ring. The use of a linac for SASE was considered in [11] and [12]. A detailed comparison between rings and FELs can be found in [13].

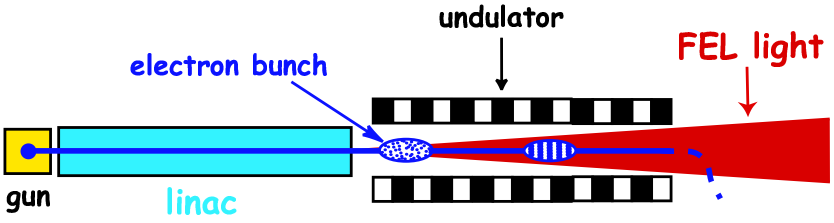

Figure 3: *FEL in single pass configuration.*

and duration.
The lack of temporal coherence can be overcome using a coherent seed to drive the process (Harmonic Generation (HG)). In this case the electrons behave as an active medium to generate radiation at the harmonics of the seed. The most efficient HG scheme relies on at least two independent undulators, the second one being tuned to one of the harmonics of the first. The external seed, e.g. a laser, is focused in the first undulator and synchronized with the incoming electron bunch. The laser-electron interaction produces energy modulation in the particle distribution. This modulation is converted in spatial separation (bunching) in a short magnetic section placed between the undulators, called dispersive section. Performing a Fourier analysis, the spatial bunch distribution shows harmonic components of the fundamental wavelength. Therefore, in the second undulator, the electron beam emits coherent radiation at the selected harmonic wavelength.
The higher the harmonic number, the lower the efficiency of the process. Therefore, in order to reach the VUV–X-ray spectral range, the seed laser wavelength has to be as short as possible. Unfortunately, below 200 nm there are no conventional lasers with enough peak power (∼100 MW) and the desired tunability. The next generation of seeded FELs will use two or three undulator cascades (as described before) to shorten the final wavelength. Another possibility is the direct seeding with High Harmonic Generation (HHG) in gas jets, but for the moment the required power and tunability have been demonstrated only above 50 nm[2].

The single pass configuration has been implemented on the Elettra SRFEL by removing the optical cavity (see Fig. 4). A Ti:Sapphire laser provides the seed for harmonic generation. The interaction with the seed laser (and the consequent emission) occurs in a single pass, as in a linear accelerator, but in this case the electron beam is re-circulated and, as a consequence, is the same in the successive interactions.

It is important to stress that new-generation single-pass FELs are based on linear accelerators [14]. Electron bunches delivered by such devices are generally characterized by higher peak current and lower relative energy spread compared to bunches circulating into a SR. As a consequence, linac-based FELs can be expected to produce optical pulses with energy three-four orders of magnitude larger than the ones produced by SR-based FELs. However, for SR based FELs, due to re-circulation of the beam, the mean energy and current distribution are “thermalized” by long-lasting periodic dynamics. Hence, in principle, these sources are characterized by an excellent shot-to-shot stability. Vice versa, successive electron bunches delivered by a linac are generally characterized by significant fluctuations of the mean electron-beam energy and current. This may result in

---

[2] Parametric amplifiers in the infrared domain are currently investigated but there is no proof of they can provide the required power.

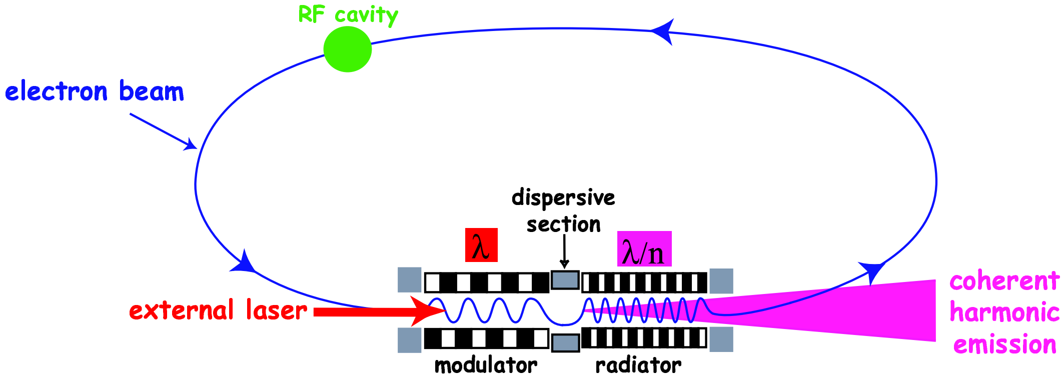

Figure 4: *SRFEL in single-pass configuration.*

a remarkable shot-to-shot fluctuations of the emitted harmonic power [15]. Moreover, SR allows to produce harmonic pulses at relatively high repetition rate (order of 1 kHz or even higher) to the benefit of average harmonic power. Only FELs based on superconducting linacs can reach analogous performance, while normal-conducting devices are limited to repetition rates of the order of 100 Hz. Finally, the coherent FEL light generated by a SR is naturally synchronized to the synchrotron radiation emitted by undulators and bending magnets. This makes easier the design and the realization of pump-probe experiments.

0.3 FELs: state of the art

In order to set a frame of reference for the experimental results presented in this thesis, the current status of the FEL-based sources is here described, focusing in particular on storage-ring FELs and next-generation single-pass FELs. For a detailed list of existing FEL projects see [16].

Figure 5 shows the performance (power vs. wavelength) of 4 active SRFEL facilities (Elettra, Duke, Uvsor and NIJI4) and of one (Super-ACO) which is no more operational.

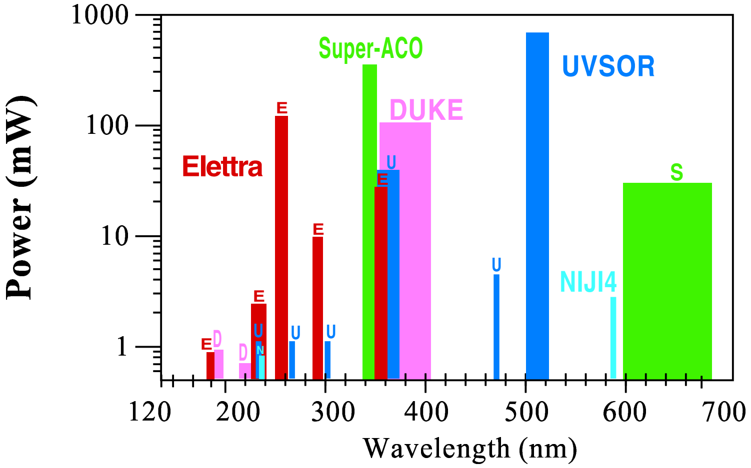

Figure 5: *Power produced by storage-ring Free-Electron Lasers at different wavelengths. Elettra FEL (Italy), Duke (USA), Uvsor (Japan) and NIJI4 (Japan) SRFELs are still active, Super-ACO has been dismissed.*

Linac-based FELs aim at providing radiation with pulse length of about 100 fs in the hard X-rays range. Some prototypes have been realized in the recent past in order to test both the SASE and the HG principles. The first SASE experiment to show high gain is described in [17]. Among experiments in SASE regime,LEUTL (Low Energy Undulator Test Line) (Advanced Photon Source, Argonne, USA) has reached the saturation at 530 nm; VISA (Visible to Infrared SASE Amplifier) at Accelerator Test Facility of Brookhaven National Laboratory, produced FEL radiation at 840 nm; TTF (Tesla Test Facility) [or FLASH (Free-electron LASer in Hamburgh)] at DESY (Germany), reached at 6 nm and SCSS (SPring-8 Compact SASE Source) at SPring-8 (Japan) down to 50 nm. The High Gain Harmonic Generation (HGHG) scheme has been tested at Deep Ultra Violet–FEL (National Synchrotron Light Source, BNL, USA) with the generation of the first coherent UV FEL radiation at 266 nm.
Most of the projects under development are based on SASE: Linac Coherent Light Source (SLAC, Stanford, USA) aims at reaching 0.15 nm, in 2009, SPARC (Frascati, Italy), 500 nm, in 2008, SCSS XFEL (SPring-8, Japan), 0.1 nm in 2011, European XFEL (DESY, Germany), 0.1 nm, in 2014). The only facility under construction which will be based on seeded HG is FERMI (Trieste, Italy). This FEL will cover the range from 100 to 10 nm; commissioning in foreseen in 2009.
Other proposed seeded-FELs are: Soft X-ray FEL (Berlin, Germany), shortest wavelength: 1.2 nm, SPARX (Frascati, Italy), shortest wavelength: 1.5 nm, Arc-en-ciel (Saclay, France), shortest wavelength: 1 nm.
An overview of th main projects is given in Fig. 6.

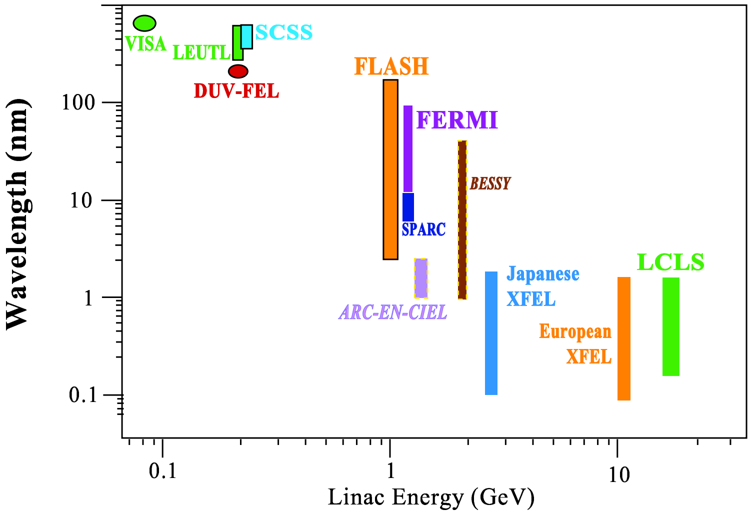

Figure 6: *Target wavelength and linac energy of present and future FELs in single-pass configuration. SASE: VISA (USA), SCSS (Japan), FLASH (Germany), SPARC (Italy), Japanese-XFEL, European-XFEL, LCLS (USA). Seeded HG: DUV-FEL (USA), FERMI (Italy), Arc-en-ciel (France), BESSY-FEL (Germany).*

The improvement in terms of peak brightness of the X-FEL projects with respect to a typical 3^{rd} generation synchrotron light source (such as Elettra) is of several orders of magnitude, as shown in Fig. 7. As it can be seen, SRFELs produce a radiation with intermediate brightness.

One of the key parameters for light sources is the pulse duration, which determines

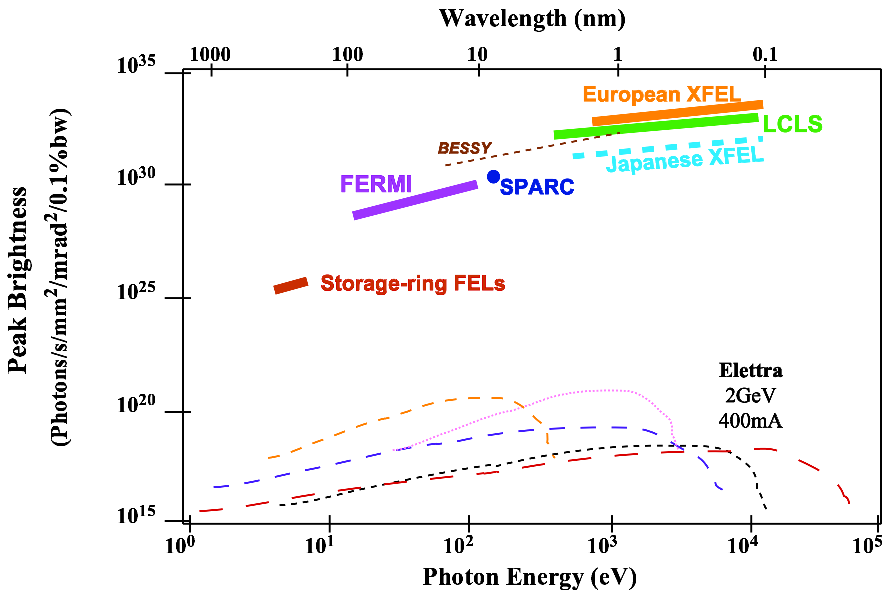

Figure 7: *Comparison between X-FEL projects and 3rd generation synchrotron light sources in terms of peak brightness [18].*

the temporal scale of the physical (or chemical, or biological) process that is possible to investigate. Figure 8 shows the evolution of the pulse duration of various light sources. Presently, the trend is to go below the femtosecond scale, approaching the attosecond range.

The seeded single-pass configuration has been implemented only two times on storage-ring FELs. Proof of principle of generation of coherent harmonic radiation at 355 nm was first performed at LURE (Orsay, France) [20] using a Nd:YAG laser. Recently, coherent emission at 260 nm, the third harmonic of the Ti:Sapphire laser, was observed at UVSOR (Okazaki, Japan) [21].

0.4 Review of obtained results

In this thesis we explore the possibility to extend the capabilities of the Elettra SRFEL towards shorter wavelengths by means of harmonic generation.
When operated in oscillator configuration, the Elettra SRFEL is able to produce coherent radiation in the spectral range from the visible to the VUV (660–176 nm), with pulse-length of tens of ps. By implementing different experimental techniques for producing harmonic radiation, coherent pulses at 220 and 150 nm have been generated.

In the last two years, a seeded "single-pass" configuration has been implemented at the Elettra SRFEL. The source developed is presently the only one which is able to produce coherent light with different pulse duration (100 fs – 1 ps), significant power (∼ 1 MW) and variable polarization in a wide VUV spectral range. The radiation has been used for two kind of experiments, one in gas phase, the other of solid state, demonstrating that this facility can be suitable for users. In the wavelength range will be extended and the tunability of the source will be improved. The source developed during the activity reported in this thesis can be also considered as an ideal test bed for the next generation of single-pass FELs. In fact, it offers valuable chance to test in advance the techniques

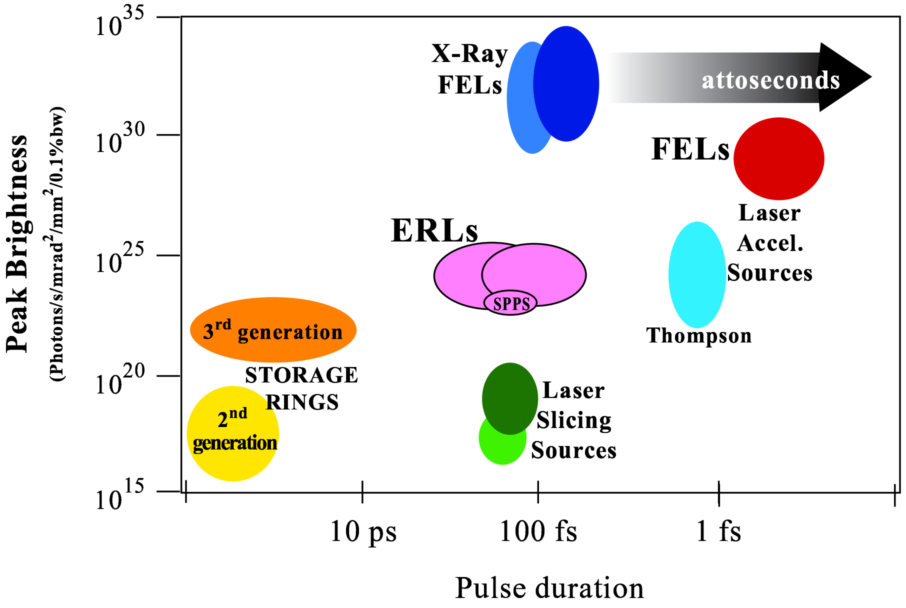

Figure 8: *Evolution of light sources in terms of Peak brightness vs. pulse duration. [19].*

and methods to be used in many of the experiments that will be realized on future FELs. The work presented here has been carried out within the "new light sources" group of Elettra at Sincrotrone Trieste. Part of the activity was supported by the European project EUROFEL through the Task 4, oriented to the "Seeding and harmonic generation". The working group involved 9 partners (BESSY and Hamburg Univ. (Germany), STFC and Strathclyde Univ. (UK), CEA-SPAM and Soleil (France), Elettra and ENEA (Italy), Max-lab (Sweden)). Ongoing collaborations: Duke University (Durham, NC, USA), Brookhaven National Laboratory (Upton, NY, USA), Lawrence Berkeley National Laboratory (CA, USA), Science Applications International Corp.-University of Maryland (USA).

The structure of this work is the following.
Chapter 1 reviews basic accelerators physics and synchrotron radiation notions, as well as all the knowledge required as a background for the following parts.
In Chapter 2 the FEL theory, both for oscillator and single-pass FEL configurations, is presented.
Chapter 3 is devoted to the description of the coherent harmonic generation.
In Chapter 4 we present an overview of the experimental layout of the Elettra FEL, describing the synchrotron source, the insertion devices, the seed laser system and the diagnostics.
Chapter 5 is dedicated to present the results of harmonic generation in oscillator configuration.
In Chapter 6 we report the full characterization of the source in seeded single-pass configuration.
Chapter 7 reports the results of experiments performed in the seeded configuration.
In Chapter 8 we conclude and give the perspectives of this facility.

Bibliography

[1] S. Milton *et al.*, *Science* **292**, 2037 (2001)

[2] L. H. Yu *et al.*, *Science* **289**, 932 (2000)

[3] T. Shintake, Proceedings of PAC07, Albuquerque, New Mexico, USA

[4] R. Bonifacio, C. Pellegrini and L. M. Narducci, *Opt. Comm* **50**, 373 (1984)

[5] B. Murphy and C. Pellegrini, "Generation of High Intensity Coherent Radiation in the Soft X-Ray and VUV region" *Journ. OSA;B2* **259**, 373 (1985)

[6] R. Coisson and F. De Martini, *Physics of Quantum Electronics* **9**, 939 Addison-Wesley, Reading, MA, 1982;

[7] L. H. Yu, *Phys. Rev. A* **44**, 5178 (1991)

[8] A. Doyuran *et al.*, *Phys. Rev. Lett.* **86**, 5902 (2001)

[9] L. H. Yu, *et al.*, *Phys. Rev. Lett.* **91**, 074801 (2003)

[10] A. Doyuran *et al.*, *Phys. Rev. S.T.-AB* **7**, 050701 (2004)

[11] C. Pellegrini, "Progress Toward a Soft X-Ray FEL" *Nucl. Instr. and Meth. A* **272**, 364 (1988)

[12] C. Pellegrini, "Linacs for Free Electron Lasers" *Proc. of the 1990 Linear Accelerator Conference*, p.273 (1990)

[13] C. Pellegrini, "Is the X-Ray FEL the 4th Generation Light Source?" *Proc. of the 1998 European Particle Accelerator Conference, Stockolm*, Inst. of Phys. Publisher, p.83-87 (1988)

[14] See http://www.elettra.trieste.it/FERMI/

[15] E. Allaria, G. De Ninno, M. Trovo, Proceedings of FEL 2006, BESSY, Berlin, Germany

[16] http://sbfel3.ucsb.edu/www/vl_fel.html

[17] M. Hogan *et al.*, "Measurements of Gain Larger than 10^5 at $12 \mu m$ in a Self-Amplified Spontaneous-Emission Free-Electron Laser" *Phys. Rev. Lett.* **81**, 4867 (1998)

[18] A. Renieri, Proceedings of the 27th International Free Electron Laser Conference, Stanford, California, USA

[19] W. Barletta and C. Rizzuto, “VUV and X-Ray Free Electron Lasers: The Technology and its scientific promise”, Rivista del Nuovo Cimento

[20] B. Girard *et al.*, *Phys. Rev. Lett.* **53**, 2405 (1984)

[21] M. Labat *et al.*, *Eur. Phys. J. D* **44**, 187 (2007)

Other related papers:

[22] J. Madey, *J.of Appl.Phys.* **42**, 1906 (1971)

[23] L. R. Elias *et al.*, *Phys. Rev. Lett.* **36**, 717 (1976)

[24] D. A. G. Deacon *et al.*, *Phys. Rev. Lett.* **38**, 892 (1977)

[25] I. Boscolo and V. Stagno, *Nucl. Instrum. Methods Phys. Res.* **198**, 483 (1982)

[26] M. Billardon *et al.*, *Phys. Rev. Lett.* **51**, 1652 (1983)

[27] M. Billardon *et al.*, *Europhys. Lett.* **3**, 689 (1987)

[28] R. Prazeres *et al.*, *Europhys. Lett.* **4**, 817 (1987)

[29] R. Bonifacio, L. de Salvo Souza, P. Pierini, E. T. Scharlemann, *Nucl. Instrum. Methods Phys. Res. A* **296**, 787 (1990)

[30] R. Bonifacio *et al.*, “Physics of the High-Gain FEL and Superradiance”, Il Nuovo Cimento, vol.13, N.9 (1990)

[31] R. Prazeres *et al.*, *Nucl. Instrum. Methods Phys. Res. A* **304**, 72 (1991)

[32] D. A. Jaroszynski, R. Prazeres, F. Glotin, O. Marcouille, J. M. Ortega, *Nucl. Instrum. Methods Phys. Res. A* **375**, 456 (1996)

Chapter 1

Accelerators Physics and Synchrotron radiation

The electron beam is generally created by a (thermo-ionic) gun, accelerated along a linear accelerator (linac) or a circular synchrotron (booster) and then injected in the storage ring where the beam stays for several hours at constant energy. While electrons circulate in the storage ring, they emit electromagnetic radiation wherever they pass through magnetic fields. This is called "synchrotron radiation".

1.1 Accelerator Optics

A storage ring (see Fig. 1.1) is basically composed of a series of straight sections, where there is space to accommodate insertion devices, a series of arc sections, where the beam is bended according to the Lorentz force, and a series of other magnets (quadrupoles) that maintain focused the beam in the transverse plane with respect to its motion.

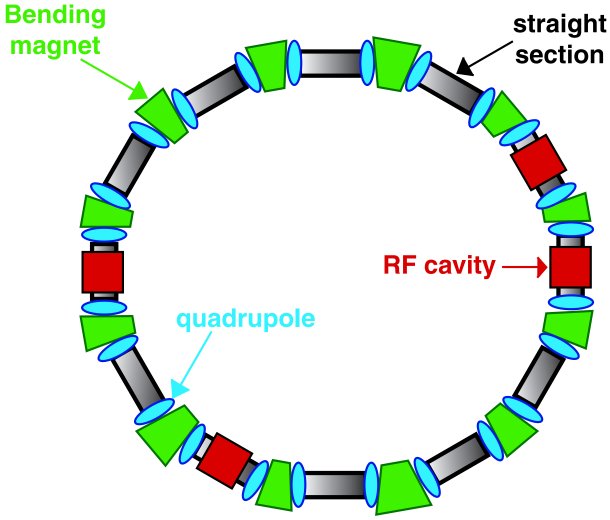

Figure 1.1: *Layout of a storage ring with main components.*

Electrons circulate in a metallic pipe, the vacuum chamber, where the air pressure is usually reduced to some 10^{-9} mbar, or lower, to prevent scattering between particles and residual gas atoms that can reduce the lifetime of the beam. This pressure is maintained by several vacuum pumps placed along the ring. In the longitudinal plane with respect to electrons motion, the RF cavities accelerate the particles providing the energy they have lost owing to synchrotron emission. Actually, there are different kinds of magnets that bend the electrons trajectory. Although bending magnets are mainly used to form a closed path, they are also sources of synchrotron radiation. Quadrupole magnets act as glass lenses in light optics focusing particles in the transverse plane with respect to their motion. Therefore their action is only on the transverse plane with respect to the electrons trajectory. As a first approximation, the electron motion can be basically considered decoupled in longitudinal and transverse components.

1.1.1 Transverse motion

Twiss functions, Beam Emittance and Phase Space Ellipse

Considering the reference frame in Fig. 1.2.

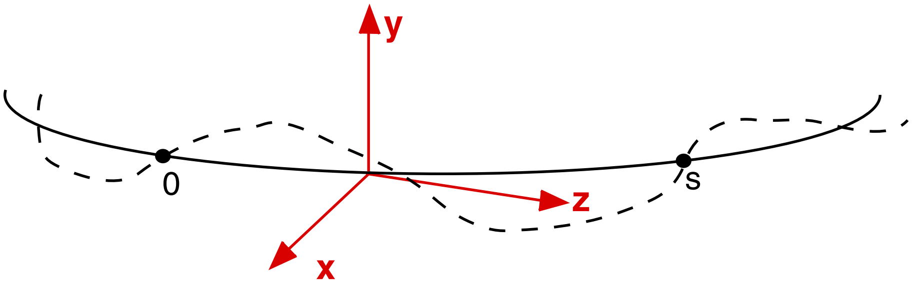

Figure 1.2: *Reference frame for the electron motion in a storage ring.*

In the transverse space (x,y), the electrons perform the so-called “betatron oscillations” about the ideal reference orbit. In the x axis (same considerations hold for the y direction) the amplitude of this oscillatory motion is given by

$$x = \sqrt{\epsilon}\sqrt{\beta(s)}\cos(\psi(s)+\varphi) \tag{1.1}$$

$$x' = -\frac{\sqrt{\epsilon}}{\sqrt{\beta(s)}}\Big[\alpha(s)\cos(\psi(s)+\varphi)+\sin(\psi(s)+\varphi)\Big] \tag{1.2}$$

where ϵ, φ are integration constant determined by initial conditions, $\beta(s)$ is a periodic function given by focusing properties of the lattice (i.e., quadrupoles), $\alpha(s) = -\frac{1}{2}\beta'(s)$ and $\psi(s) = \int_0^s \frac{\mathrm{ds}}{\beta(s)}$ is the phase advance of oscillation between point “0” and point “s” in the lattice. The phase advance calculated over one complete revolution gives the TUNE, i.e. the number of oscillations per turn $Q_y = \frac{1}{2\pi}\oint \frac{\mathrm{ds}}{\beta(s)}$.

From 1.1 we get $\cos(\psi(s)+\varphi) = \frac{x(s)}{\sqrt{\epsilon}\sqrt{\beta(s)}}$ that can be inserted into 1.2 and solving for ϵ one obtains

$$\epsilon = \gamma(s)x^2(s) + 2\alpha(s)x(s)x'(s) + \beta(s)x'^2(s) \tag{1.3}$$

where $\gamma(s) = \frac{1+\alpha^2(s)}{\beta(s)}$. The functions $\alpha(s), \beta(s), \gamma(s)$ are usually called Twiss functions. The quantity ϵ is a constant of the motion, independent of s, and it is called “beam emittance”. The Eq. 1.3 describes an ellipse in the phase space (x, x') with area $A = \pi\epsilon$ (see Fig. 1.3).

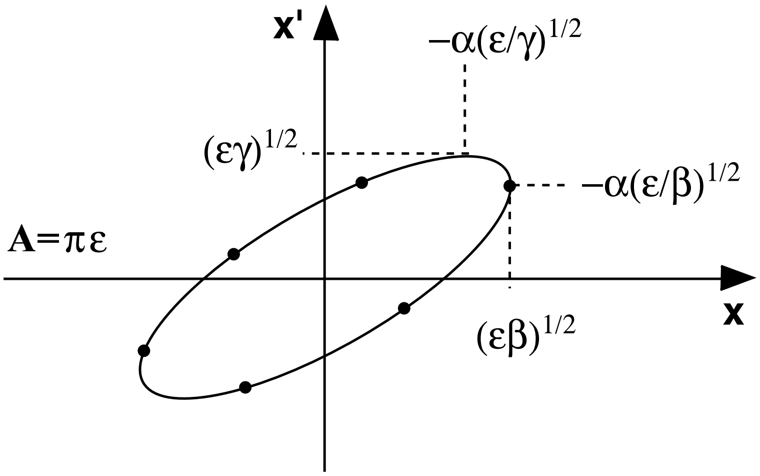

Figure 1.3: *Phase space ellipse.*

The transverse (betatron) motion between the point 0 and the point s is described in the matrix formalism by

$$\begin{pmatrix} x \\ x' \end{pmatrix}_s = M \begin{pmatrix} x \\ x' \end{pmatrix}_0, \qquad \begin{pmatrix} y \\ y' \end{pmatrix}_s = M \begin{pmatrix} y \\ y' \end{pmatrix}_0 \tag{1.4}$$

with

$$M = \begin{pmatrix} \sqrt{\frac{\beta_s}{\beta_0}}\,(\cos\psi_s + \alpha_0 \sin\psi_s) & \sqrt{\beta_s\beta_0}\,\sin\psi_s \\ \frac{(\alpha_0 - \alpha_s)\cos\psi_s - (1+\alpha_0\alpha_s)\sin\psi_s}{\sqrt{\beta_s\beta_0}} & \sqrt{\frac{\beta_s}{\beta_0}}\,(\cos\psi_s - \alpha_s \sin\psi_s) \end{pmatrix}. \tag{1.5}$$

For a Gaussian particle distribution (as an electron beam in a storage ring) the beam emittance is defined as

$$\epsilon_x = \frac{\sigma_x^2}{\beta_x(s)} \tag{1.6}$$

then the standard beam size and beam divergence are defined by

$$\sigma_x = \sqrt{\epsilon_x\beta_x} \qquad \sigma_y = \sqrt{\epsilon_y\beta_y} \tag{1.7}$$

$$\sigma_{x'} = \sqrt{\epsilon_x\gamma_x} \qquad \sigma_{y'} = \sqrt{\epsilon_y\gamma_y}. \tag{1.8}$$

1.1.2 Longitudinal motion

The RF acceleration cavity provides a longitudinal electric field, at an RF frequency of usually hundreds of MHz to accelerate electron beam. For a particle of charge e the energy gain/loss per passage through a cavity gap is $\Delta E = eV_{rf}$ where e is the electron charge, $V_{rf} = V_0 \sin(\omega_{rf}t + \vartheta)$ is the effective gap voltage, ω_{rf} is the RF frequency, V_0 is the effective peak accelerating voltage and ϑ is the phase angle. The RF frequency is matched with the particle velocity (synchronization) and the phase angle between the RF wave and the beam bunch is chosen to accelerate particles to high energies (phase focusing).

The instantaneous power radiated by electron through synchrotron radiation is given by

$$P_\gamma = \frac{cC_\gamma}{2\pi}\frac{E^4[GeV]}{\mathcal{R}^2[m]} \tag{1.9}$$

where $C_\gamma = \frac{4\pi}{3}\frac{r_c}{(m_e c^2)^3} = 8.8575 \cdot 10^{-5}\,\mathrm{m/GeV}^3$ (r_c is the electron classical radius, m_e the electron mass and c the speed of light) and $\mathcal{R}$ is the mean radius of the ring.

One can consider the total energy loss per turn for a ring composed of a set of equal magnets with the same curvature $1/\mathcal{R}$

$$U_0 = C_\gamma \frac{E^4[GeV]}{\mathcal{R}[m]}. \tag{1.10}$$

To recover this energy one or more RF cavities are distributed along the ring and they generate oscillating electric fields parallel to the beam path of accelerated electrons. Since the typical frequency for a RF cavity is order of 500 MHz, the critical parameter is the arrival time of particles in the cavity (see Fig. 1.4).

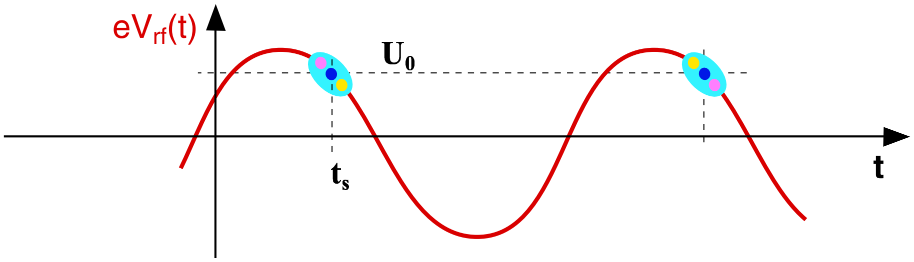

Figure 1.4: *RF-cavity voltage and electron bunch.*

Since we consider relativistic particles, the travel time depends on the electron energy because particles with higher energy then ideal cover a longer path while particles with smaller energy follow a path shorter than the ideal. This is expressed by the "momentum compaction" factor α_c defined by the following relation:

$$\frac{\Delta C}{C_0} = \alpha_c \frac{\Delta E}{E_0} \tag{1.11}$$

where ΔC is the relative change of the orbital path length, C_0 is the circumference of the ring, ΔE is the relative energy error and E_0 is the energy of the ideal particle.

The "phase focusing" is the extraordinary feature that allows to have a stable beam: the particles are forced to arrive at the cavity close to the synchronous phase/time. A particle with higher energy arrive at the cavity a bit in advance with respect to the ideal (synchronous) particle and experiencing a weaker field it will be accelerated less. Next turn the same particle will arrive in advance and will be accelerated more. And so on. All stable electrons stay essentially around the ideal particle performing the so-called "synchrotron oscillations".

Quantitatively, the total energy change per turn can be written as $\mathrm{d}E = eV_{rf}(t) - U(E)$ where $U(E)$ the energy loss per turn at energy E. Expanding at $t = t_s + \tau$ (where t_s is the synchronous time at which the ideal particle gain exactly the energy lost) and $E = E_0 + \epsilon$

and keeping only linear terms, one can found:

$$\begin{aligned}\frac{\mathrm{d}\epsilon}{\mathrm{d}t} &= \frac{1}{T_0}\left[eV_{rf}(t_s) + e\frac{\partial V_{rf}}{\partial t}|_{t_s}\tau - U(E_0) - \frac{\mathrm{d}U}{\mathrm{d}E}|_{E_0}\epsilon\right] \\ &= \frac{1}{T_0}\left[e\frac{\partial V_{rf}}{\partial t}|_{t_s}\tau - \frac{\mathrm{d}U}{\mathrm{d}E}|_{E_0}\epsilon\right]\end{aligned} \tag{1.12}$$

where T_0 is the revolution time and the relation $eV_{rf}(t_s) = T(E_0)$ has been used. If a particle has an energy deviation ϵ, its revolution time will be different from the ideal one T_0 and one can found that:

$$\frac{\Delta T}{T_0} = \frac{\mathrm{d}\tau}{\mathrm{d}t} = \left(\frac{1}{\gamma^2} - \alpha_c\right)\frac{\epsilon}{E_0} \equiv \dot{\tau}. \tag{1.13}$$

Differentiating Eq. 1.12 with respect to t one can derives the equation of motion for "synchrotron oscillations"

$$\frac{\mathrm{d}^2\epsilon}{\mathrm{d}t^2} + \frac{1}{T_0}\frac{\mathrm{d}U(E_0)}{\mathrm{E}}\frac{\mathrm{d}\epsilon}{\mathrm{d}t} + \omega_s^2\epsilon = 0 \tag{1.14}$$

where the synchrotron frequency ω_s is

$$\omega_s^2 = \frac{(\gamma^{-2} - \alpha_c)}{E_0 T_0}e\frac{\mathrm{d}V(t)}{\mathrm{d}t} = \omega_0^2\frac{h(\gamma^{-2} - \alpha_c)eV_0\cos\psi_s}{2\pi E_0} \tag{1.15}$$

with $\omega_0 = 2\pi/T_0$, $V_{rf} = V_0 \sin\omega_{rf}t$ and therefore $\dot{V} = \omega_{rf}V_0\cos\psi_s = 2\pi h/T_0 V_0\cos\psi_s$. h is the harmonic number, defined as $h = C_0/\lambda_{rf}$ and must be an integer. $\psi_s = \omega_{rf}t_s$ is the synchronous phase at which a particle with energy E_0 is accelerated exactly to compensate for the energy loss to radiation. The solution of the differential equation of motion is that of a damped harmonic oscillator

$$\epsilon(t) = \epsilon_0 e^{-\alpha_s t}e^{i\omega_s t}. \tag{1.16}$$

The damping time, defined as $\tau_s = 1/\alpha_s$ is of the order of milliseconds while the synchrotron oscillation period is much shorter, of order of 10–50 μs. This different time scale allows to neglect damping in the synchrotron oscillation treatment.

Large amplitude oscillations determine the energy "aperture" or "acceptance" of a ring. The separatrix curve in Fig. 1.5 divides the stable oscillations from unstable trajectories.

Particles performing stable oscillations are captured in small clusters called "bunches".

The maximum number of bunches circulating along the storage ring is given by the ratio between the RF frequency ω_{rf} and the revolution frequency ω_r. These two quantities are linked by the so-called harmonic number h:

$$\omega_{rf} = h\omega_r. \tag{1.17}$$

The harmonic number gives the number of "buckets", i.e., the maximum number of bunches into the ring.

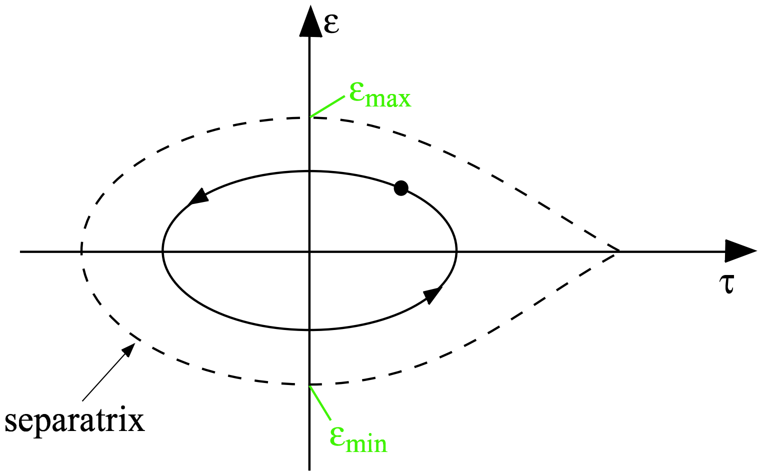

Figure 1.5: *Longitudinal Phase diagram.*

Damping and quantum effects

Synchrotron radiation causes damping of all coordinates in 6-dim $(x, x', y, y', \epsilon, \tau)$ phase space. The longitudinal energy loss is restored by RF cavities while in the transverse direction the particles perform betatron oscillations with lower and lower amplitude that scales as $A(t) = A_0(t)e^{-\alpha_s t}$ where $\alpha_s = (1/2T_0)\mathrm{d}U(E_0)/\mathrm{d}E$.

This damping effect is counterbalanced by the so-called "quantum effects" even if the synchrotron radiation is a process that can be described in a classical way. However, the emission of electromagnetic radiation occurs during such a short time that the particle cannot react adiabatically to the perturbation created by this radiation emission. The particle reaction time scales are actually the damping times. Therefore we have to deal with events that seem to happen suddenly.

Energy Fluctuations

For a storage ring with a constant radius $\mathcal{R}_0$ in the magnets, the relative energy spread may be written as

$$\left(\frac{\sigma_\epsilon}{E_0}\right)^2 = \frac{C_q \gamma_0^2}{J_\epsilon \mathcal{R}_0} \tag{1.18}$$

where $C_q = 3.84 \times 10^{-13}\,\mathrm{m}$, $J_\epsilon = 2 + \alpha R/\mathcal{R}_0$ with R the gross orbit radius.

The fluctuating energy oscillations are accompanied by associated fluctuations in the time displacement τ. The standard deviation of these fluctuations is connected to the standard deviation of energy oscillations σ_ϵ by

$$\sigma_\tau = \frac{\alpha}{\Omega E_0}\sigma_\epsilon \tag{1.19}$$

where $\Omega^2 = \frac{\alpha e \dot{V}_0}{T_0 E_0}$ is the angular frequency of small longitudinal oscillations.

Since the energy deviation has a Gaussian distribution (from the central limit theorem), also the temporal distribution has a Gaussian shape.

$$\sigma_\tau^2 = \frac{\alpha^2}{\Omega^2}\frac{C_q \gamma_0^2}{2\mathcal{R}_0 + \alpha R} = \frac{\alpha T_0 E_0}{e\dot{V}_0}\frac{C_q \gamma_0^2}{2\mathcal{R}_0 + \alpha R} = \frac{2\pi C_q}{(mc^2)^2}\frac{\alpha R}{2\mathcal{R}_0 + \alpha R}\frac{E_0^3}{e\dot{V}_0} \tag{1.20}$$

The Eq. 1.19 is true only when the interaction of electrons with the beam pipe is not strong (weak wake fields) and the electron motion is not perturbed.

The natural energy spread is energy spread at zero current.

Figure 1.6 shows two sets of measurements performed at Elettra. The energy-spread growth as a function of the current stored in the ring. Also the bunch-length increases with the accumulated current. The FEL is in competition with the instabilities since the latter grows with the energy spread.

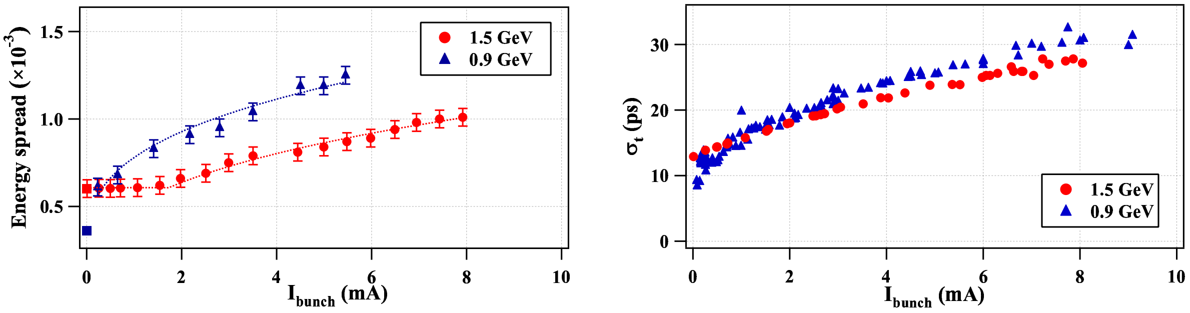

Figure 1.6: *Energy spread and bunch length vs. current at different energies. Experimental data of Elettra SR.*

At first order, parasitic electromagnetic fields (wake fields) on the beam pipe cause energy spread on the beam.

Longitudinal instabilities

Wakefields Figure 1.7 shows the image current induced by the circulating beam in the vacuum chamber.

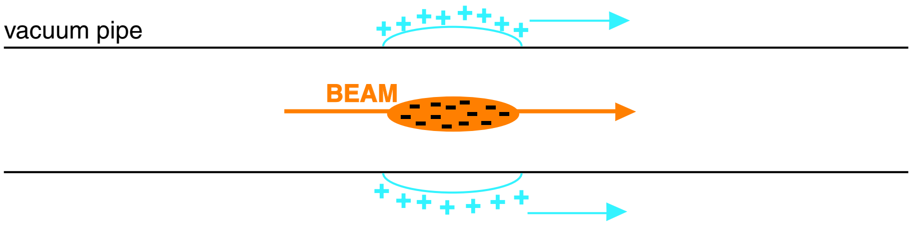

Figure 1.7: *Vacuum chamber image currents responsible for Wake fields).*

The image current creates the so-called “wake field”. The wake fields increase the energy spread and as a consequence the bunch length.

1.1.3 One-turn longitudinal map

Assuming decoupled longitudinal and transverse dynamics, the electron beam propagation at pass n in the longitudinal phase space can be described by [1]:

$$\begin{cases} t_{n+1} = t_n - \alpha_{cp} T_0 \dfrac{\gamma_n - \gamma_0}{\gamma_0} \\ \gamma_{n+1} = \gamma_n \left[1 + \dfrac{\gamma_n - \gamma_0}{\gamma_0} + \dfrac{eV_{rf}}{E_0} \sin(\omega_{rf} t_{n+1} + \varphi) - U_0 E_0 - \mathcal{D}(\gamma_n, t_n) + \mathcal{R}(\gamma_n, t_n) \right] \end{cases} \tag{1.21}$$

where t_n is the relative position of the electron with respect to the synchronous electron, γ_n is the normalized energy of the electron, γ_0 is the energy of the synchronous electron, T_0 is the revolution period, α_{cp} is the momentum compaction[1], $\mathcal{D}(\gamma_n, t_n)$ is the synchrotron damping term, that accounts for oscillation damping due to synchrotron emission, and $\mathcal{R}(\gamma_n, t_n)$ accounts for the stochastic process of photon emission.

1.1.4 Lifetime

After the injection in the storage ring, the electrons stay many hours at almost constant current. Without interactions between the electron beam and the environment, they would circulate in principle forever in the beam pipe, but it is obvious that in reality there are interactions causing the loss of some particles. Hence the electron beam has a limited "lifetime" due mainly to three phenomena:

- Interaction with the residual gas in the vacuum chamber,
- Quantum emission and transverse acceptance,
- Touschek effect.

The first phenomenon is mainly an elastic scattering that gives rise to bremsstrahlung radiation. The second effect depends on the transverse dimensions of the beam with respect to the beam pipe diameter. The electrons in the sidebands of the Gaussian distribution can be lost owing to the impact with the walls of the vacuum chamber. The Touschek effect consists on the interaction between electrons in the same bunch which causes diffusion of particles and then electrons loss. The higher the stored current, the higher this effect.

The total lifetime can be calculated accounting these three contributions:

$$\frac{1}{\nu_T} = \frac{1}{\nu_1} + \frac{1}{\nu_2} + \frac{1}{\nu_3} \tag{1.22}$$

Between the natural phenomena, the Touschek effect is dominant for high current and low energy of electrons, because it scales as $1/\gamma^3$. The electrons can be lost also because the betatron oscillations are too large and the amplitude of the transverse motion exceed

---

[1] The momentum compaction factor is defined by $\frac{\delta l_\epsilon}{L} = \alpha_{cp} \frac{\Delta p}{p}$ or by $\alpha_{cp} = \frac{1}{L} \oint \left(\frac{D(s)}{\mathcal{R}(s)} \right) \mathrm{d}s$ and combines via the dispersion function $D(s)$ the momentum spread Δp with the longitudinal motion of the particle (δl_ϵ is the elongation due to energy deviation, L is the circumference of the designed orbit, $\mathcal{R}(s)$ is the local radius of curvature).

the acceptance of the vacuum chamber. Nevertheless, one has to consider also the RF cavities acceptance.

The lifetime of the electron beam is a crucial parameter for a SRFEL. From the lifetime depends the stability of the emitted radiation in terms of intensity (or number of photons or brightness).

1.2 Synchrotron radiation

1.2.1 Electron motion in a periodic magnetic field

An undulator is composed of two arrays of magnetic material with alternating polarity. This device provides the static and periodic magnetic field that forces the electrons to follow an oscillating trajectory. If the phase between the two arrays is zero, the electrons are solicited to wiggle in a plane and they emit radiation linearly polarized in that plane. This case is illustrated in Fig. 1.8. If the phase is different from zero, electrons perform a helical trajectory and the resulting emission is in general elliptically polarized.

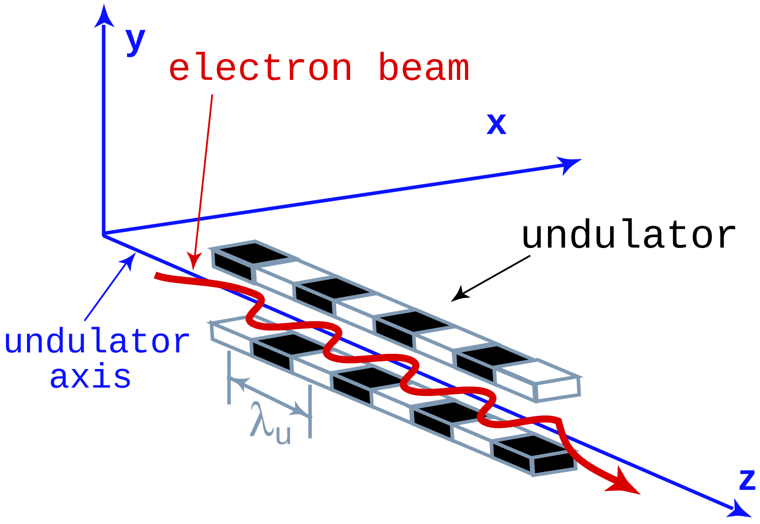

Figure 1.8: *Electron trajectory in a planar undulator.*

The most relevant features of light emission from planar and helical undulators will be discussed in some details in Ch. 6.

Here we describe the electron motion in a planar undulator.

The magnetic field has a sinusoidal profile inside the undulator:

$$\vec{B}(z) = B_0 \sin\left(\frac{2\pi}{\lambda_u} z\right) \hat{z} \tag{1.23}$$

where λ_u is the undulator period and B_0 the peak value of the magnetic field along z.

Considering the approximation of mono-energetic beam, perfectly collimated and with zero emittance, the electron motion in the magnetic field is driven by the Lorentz equation:

$$\begin{cases} \dfrac{\mathrm{d}\vec{v}}{\mathrm{d}t} = \dfrac{e}{m\gamma c}(\vec{v} \times \vec{B}) \\ \dfrac{\mathrm{d}\gamma}{\mathrm{d}t} = 0 \end{cases} \tag{1.24}$$

where m is the electron mass and c is the speed of the light. The second relation implies that energy losses due to radiation are neglected. The components of the first of the Eq. 1.24 are:

$$\begin{cases} \dfrac{\mathrm{d}v_x}{\mathrm{d}t} = \dfrac{eB_0}{\gamma mc} v_z \sin\left(\dfrac{2\pi}{\lambda_u} z\right), \\ \dfrac{\mathrm{d}v_y}{\mathrm{d}t} = 0, \\ \dfrac{\mathrm{d}v_z}{\mathrm{d}t} = \dfrac{eB_0}{\gamma mc} v_x \sin\left(\dfrac{2\pi}{\lambda_u} z\right). \end{cases} \tag{1.25}$$

Here one can defines the deflecting parameter a_u, that account for the magnetic field strength, as:

$$a_u = \frac{eB_u\lambda_u}{2\pi mc^2} \tag{1.26}$$

with $B_u = B_0/2$ for the planar undulator. If the field B_0 is not too strong, i.e. if the a_u is small, the solution of the system 1.25 is:

$$\begin{cases} x(t) = \dfrac{a_u\lambda_u}{2\pi\gamma} \sin\left(\dfrac{2\pi ct}{\lambda_u}\right), \\ y(t) = 0, \\ z(t) = \beta^* ct - \dfrac{a_u^2\lambda_u}{16\pi\gamma^2} \sin\left(\dfrac{4\pi ct}{\lambda_u}\right) \end{cases} \tag{1.27}$$

where $c\beta^* \simeq c\beta(1 - a_u^2/4\gamma^2)$ is the mean drift velocity of the electron and the factor a_u/γ represents the maximum angular deviation with respect to the undulator axis. The longitudinal motion is the combination of a linear part and a periodic oscillation. The oscillating term has a capital importance on the harmonic generation since is the source of the bunching. The spectral distribution of the undulator emission can be calculated form the well known retarded potentials and Lienard-Wiechert integral. The trajectory, $\vec{r}(t)$, defined by Eqs. 1.27 can be substituted in the fundamental formula for the synchrotron radiation:

$$\frac{\mathrm{d}^2 I}{\mathrm{d}\Omega \mathrm{d}\omega} = \frac{e^2\omega^2}{4\pi^2 c} \left| \int_{-\infty}^{+\infty} \vec{n} \times (\vec{n} - \vec{\beta}) \exp\left[i\omega\left(t - \frac{\vec{n}\cdot\vec{r}(t)}{c}\right)\right] \mathrm{d}t \right|^2 \tag{1.28}$$

where $\vec{n}$ is a unitary vector that identifies the instantaneous direction between the charge and the observer, Ω is the solid angle and ω is the frequency of the radiation. Integrating this relation one can derives the angular and spectral properties of the spontaneous emission. In the case of planar undulator, the energy emitted on-axis per unit of frequency and solid angle is given by:

$$\frac{d^2 I}{d\omega d\Omega} = \frac{e^2}{4\pi\epsilon_0 c} \left(\frac{a_u N \lambda_0}{\gamma}\right)^2 \sum_{n(impair)=1}^{\infty} \frac{A_n^2}{\lambda^2} \left(\frac{\sin(\delta_n)}{\delta_n}\right)^2 \tag{1.29}$$

with:

$$A_n \approx J_{\frac{n+1}{2}}\left(\frac{n a_u^2}{4 + 2a_u^2}\right) - J_{\frac{n-1}{2}}\left(\frac{n a_u^2}{4 + 2a_u^2}\right) \tag{1.30}$$

and

$$\delta_n = \pi N \left(n - \tfrac{\lambda_r}{\lambda}\right) \tag{1.31}$$

where J_n are the Bessel functions and N is the number of undulator periods.

The wavelength of the spontaneous radiation emitted by the undulator can be determined with simple calculations assuming, in the case of planar undulator, that the electron beam is an electric dipole oscillating along the transverse direction and moving along the undulator axis. Assuming a reference frame S' moving along z direction with the mean drift velocity of the electron:

$$c\beta^* \simeq c\beta\left(1 - \frac{a_u^2}{4\gamma^2}\right) \simeq c\beta\left(1 - \frac{a_u^2}{2\gamma^2}\right)^{1/2} \tag{1.32}$$

and in analogy

$$\gamma^* = (1-\beta^{*2})^{-1/2} = \left(\frac{\gamma^2}{1+\beta^2 a_u^2/2}\right)^{1/2} \simeq \frac{\gamma}{(1+a_u^2/2)^{1/2}}. \tag{1.33}$$

If $a_u \ll 1$ (weak undulator) the quadratic term in the third of 1.27 can be neglected and then in S' the electron perform a periodic oscillation following

$$x' = \frac{a_u \lambda_u}{2\pi\gamma} \sin(\omega' t) \tag{1.34}$$

and it emits dipole radiation at the frequency

$$\omega' = \frac{2\pi c}{\lambda_u'} = \frac{2\pi c \gamma^*}{\lambda_u}. \tag{1.35}$$

Back to the laboratory frame, the frequency ω' undergo a Doppler shift given by:

$$\omega = \frac{\omega'(1-\beta^{*2})^{1/2}}{1-\beta^* \cos\theta} \tag{1.36}$$

where θ is the observation angle whit respect to z axis. If $\theta \ll 1$ the emission is confined in a cone of aperture $1/\gamma$ around the light propagation axis. The observed frequency is:

$$\begin{aligned} \omega = \frac{2\pi c}{\lambda_u} \cdot \frac{1}{1-\beta^*\left(1-\dfrac{\theta^2}{2}\right)} &= \frac{2\pi c}{\lambda_u} \cdot \frac{2\gamma^{*2}}{\dfrac{2}{(1+\beta^*+\beta^*\gamma^{*2}\theta^2)}} \simeq \\ \simeq \frac{4\pi c\gamma^2}{\lambda_u\left(1+\dfrac{a_u^2}{2}\right)} \cdot \frac{1}{1+\dfrac{\gamma^2\theta^2}{\left(1+\dfrac{a_u^2}{2}\right)}} &= \frac{4\pi c \gamma^2}{\lambda_u} \cdot \frac{1}{1+\dfrac{a_u^2}{2}+\gamma^2\theta^2}. \end{aligned} \tag{1.37}$$

The radiation is then characterized by a wavelength defined by:

$$\lambda_s = \frac{\lambda_u}{2\gamma^2}\left(1+\frac{a_u^2}{2}+\gamma^2\theta^2\right). \tag{1.38}$$

This relation is also called resonance equation and can be generalized for the helical undulator just assuming $B_u = B_0$ in the definition of a_u. The maximum frequency is observed on-axis while the lower frequencies have a off-axis contribution. The spontaneous emission is not coherent with respect to the time because each electron emits independently.

As a consequence, the intensity of the radiation is proportional to the number of electrons involved in this process. The line bandwith depends on the number of oscillations that electrons perform passing through the undulator, i.e., is the inverse function of the number of undulator periods

$$\frac{\Delta\lambda}{\lambda} \propto \frac{1}{N_u}. \tag{1.39}$$

The number of photons emitted for solid angle unit and unitary frequency band is called "spectral distribution" and is defined as:

$$P(\nu) \propto \frac{\sin^2\nu}{\nu^2} \tag{1.40}$$

where $\nu = \pi N_u(\omega - \omega_s)/\omega_s$, N_u is the number of undulator periods and $\omega_s = 2\pi c/\lambda_s$ is the frequency of the spontaneous emission. The full width at half maximum (FWHM) of this distribution is:

$$\frac{\Delta\omega}{\omega} \simeq \frac{1}{N_u}. \tag{1.41}$$

In Fig. 1.9 it is shown the spectrum of the spontaneous radiation emitted by a single undulator.

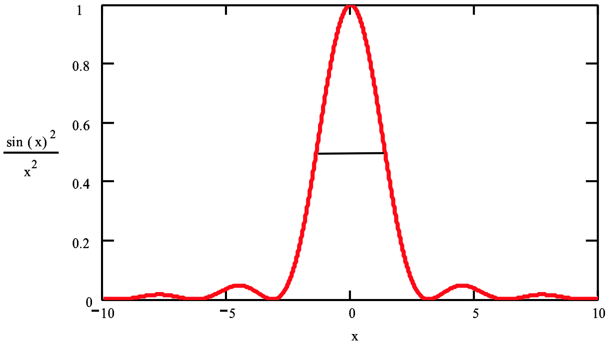

Figure 1.9: *Undulator spontaneous emission.*

1.2.2 Optical Klystron

In order to modify the spectral profile of the undulator radiation it is possible to use an optical klystron, that consists of two identical undulators separated by a dispersive section. The latter forces the electron into a large wiggle (see Fig. 1.10).

The dispersive section can be an electro-magnet which allows to vary continuously the dispersion into a certain range of values. The longer path that electrons perform through the dispersive section determines a delay respect to the spontaneous radiation emitted by the first undulator. The radiation produced in the second undulator will have a different phase and the resulting emission is the interference between the emissions of the two undulators. The intensity at the end of the optical klystron is defined as:

$$I_{OK} = 2I_{und}\left(1 + f\cos\alpha_d\right) \tag{1.42}$$

where α_d is the phase difference between the undulators emission given by:

$$\alpha_d = 2\pi\left(N + N_d\right)\frac{\lambda_r\gamma_r^2}{\lambda\gamma^2} \tag{1.43}$$

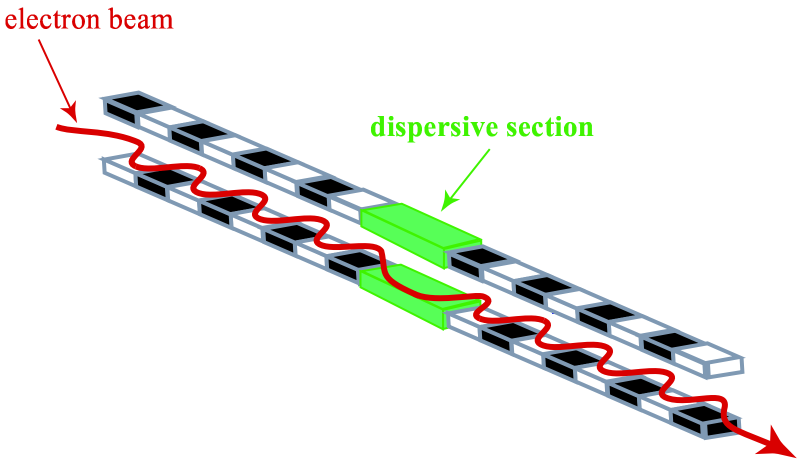

Figure 1.10: *Electron trajectory in a optical klystron.*

with N_d is the equivalent number of (undulator) periods for the dispersive section. The factor f, called modulation rate, is defined as:

$$f = \frac{I_+ - I_-}{I_+ + I_-} \tag{1.44}$$

where I_+ and I_- are respectively the maximum and the minimum intensity of interference fringes. For a Gaussian distribution the modulation rate is:

$$f = f_0 \exp - \left[8\pi^2 (N + N_d)^2 (\sigma_\gamma/\gamma)^2\right] \tag{1.45}$$

where f_0 is a factor very close to the unit that consider the effects of transverse dimensions of the electron beam.

The spectrum of the radiation emitted by an optical klystron is shown in Fig. 1.11.

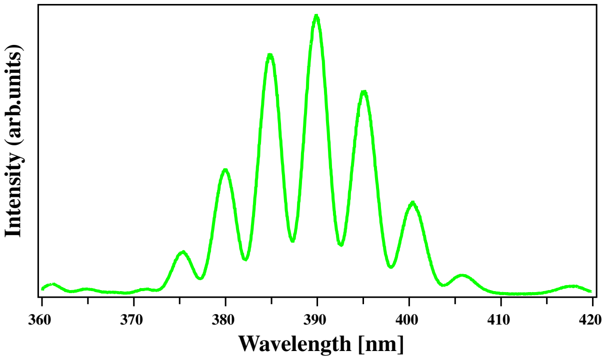

Figure 1.11: *Experimental spectrum of the Elettra optical klystron where are visible the interferential fringes.*

Bibliography

[1] M. Sands, SLAC Report No. 121, 1970 (unpublished)

[2] P. Elleaume, *Ph.D. thesis*, Université de Paris-Sud, Centre d'Orsay (1984)

Chapter 2

FEL theory

In this chapter we introduce the basic ingredients which are necessary for the description of the FEL process. We start with the theory of a single-pass FEL[1] and then we present the oscillator configuration.

2.1 Introduction

The basic principle of the FEL emission relies on interaction between a relativistic electron beam and a co-propagating electromagnetic wave in the presence of a static and periodic magnetic field. The magnetic field, provided by an undulator, induces electrons to move on an oscillating trajectory. The transverse component of the electron velocity is then coupled to the electromagnetic field propagating along the undulator axis. This interaction creates a force along this direction and, depending on their phase with respect to the electromagnetic field, electrons can gain or lose energy. As a consequence, the electron distribution inside the bunch is modified: particles distribute in micro-bunches separated by the wavelength of the co-propagating radiation. The FEL process starts when there is a net amplification of the electromagnetic wave to the detriment of the electrons' energy. FEL radiation occurs at the wavelength given by the resonant condition:

$$\lambda_s = \frac{\lambda_u}{2\gamma^2}\left(1 + \frac{a_u^2}{2} + \gamma^2\theta^2\right). \tag{2.1}$$

The FEL process can be also seen as stimulated emission/stimulated absorption process. The electromagnetic wave is amplified (net gain) when the electron beam is slightly out of resonance, because in case of perfect resonance half of electrons gain energy and half lose energy.

Two main configurations can be distinguished: the *single-pass* configuration, where the amplification of the electromagnetic wave occurs in one passage through the undulator, and the *oscillator* configuration, in which the electromagnetic wave is stored in an optical cavity and lasing is achieved as the results of a large number of light-electron interaction inside the undulator.

---

[1] For people who are not familiar with the FEL jargon, single-pass FELs are also called "amplifier" in the laser field.

2.1.1 Oscillator configuration

To enhance the emission, it is customary to use two undulators (few meters long) separated by a dispersive section, which provides a static magnetic field. The role of the dispersion section is to produce a bump in the electrons' trajectory, so that they perform a longer path and the emission from the second undulator is delayed with respect to that of the previous one. The resulting spectrum of the emitted radiation is shown in Fig. 1.11. As discussed in Section 1.2.2, the presence of interference fringes, which are absent in the case of single-undulator emission (see Fig. 1.9), enhances the gain of the amplification process. In FEL oscillators, the initial co-propagating field is provided by the spontaneous emission of electrons when they pass through the undulators. The electron beam can be provided either by a storage ring or a linear accelerator. The latter is well suited to produce radiation in the infrared range. When implemented on storage rings, the oscillator configuration allows to generate FEL radiation in the visible-VUV range. This is the case of the Elettra storage-ring FEL (SRFEL) that will be presented in the following.

The spectral width of the emitted radiation is determined by the mirrors of the optical cavity, which are characterized by a limited band (few percent around the central line) of high (95% or over) reflectivity. Also the pulse temporal duration is selected by the great number of successive interactions. As already remarked, the FEL radiation starts from the spontaneous emission, which has the same duration of the electron bunch. Due to the fact that the electron bunch has a Gaussian shape (see Section 1.1.2), the gain (Eq. 2.72) is maximum in the middle of the distribution. As a result, during successive interactions, the FEL pulse duration becomes shorter.

2.1.2 Single-pass configuration

Because of the lack of robust materials with high reflectivity in the VUV and X-rays range, there has been a great interest in developing single-pass FELs that do not need mirrors. In this configuration, the electron beam interacts with the electromagnetic field and amplifies it in a single pass through the undulator. When considering single-pass FELs, two different configurations can be distinguished, depending on the origin of the electromagnetic wave which co-propagates with electrons.

The first configuration, called Self Amplified Spontaneous Emission (SASE), takes advantage of the spontaneous emission of electrons propagating through the undulator. The electromagnetic wavelength which is amplified by the electrons is given by the resonance condition 2.1. Quite long undulators (tens of meters) are normally needed for this process to take place. Since it originates from spontaneous emission, the SASE radiation preserves the "noisy" characteristics of the latter: the emitted radiation will consist of a series of spikes with variable duration and intensity. The light characteristics strongly depends on the electron beam properties: for example, if different bunches have significant different currents also the radiation will display significant shot-to-shot fluctuations on the intensity or on the wavelength, respectively. The SASE output has very good spatial mode and is easily tunable, just changing the energy of the electrons and/or the undulator parameter a_u (see Eq. 2.1).

As an alternative, the electromagnetic wave necessary for initiating the FEL process can be provided by conventional laser or by High Harmonic Generation(HHG) source[2].

---

[2] The HHG systems use the interaction of an intense femtosecond lasers with gas jets to generate

From now we will concentrate on the configuration that is relying on the use of a conventional laser. In this case, the generation of coherent harmonics is based on the up-frequency conversion of the (high) power laser through the interaction with the relativistic electron beam.

The single-pass configuration is usually implemented on a linear accelerator (linac). At least two undulators are used, separated by a dispersive section. The laser induces energy modulation in the electron beam at its wavelength and higher harmonics in the first undulator (tuned at the laser wavelength). In the dispersive section, the energy modulation is converted in spatial separation (called "bunching"). Finally, the second undulator is tuned at one harmonic of the seed laser and the micro-bunched electron beam radiates coherently at the harmonic wavelength.

As the signal that initiates the emission is spatially and temporally coherent also the obtained radiation maintains the same properties. The electron beam properties may limit the stability and the reproducibility of the source (as in the SASE process).

Next generation of seeded FEL will be implemented in linear accelerator with high performance beam to be able to emit radiation in the VUV soft X-rays spectral range.

2.2 Theory of a single-pass FEL

In this section we will describe the FEL process staring from the Maxwell and Lorentz equations. The description will be done in a three dimensional framework but will be reduced to the one dimensional case applying some approximations to explain the FEL process.

2.2.1 3D model

We consider a mono-energetic electron beam moving through an undulator generating a static magnetic field $\vec{B_u} = \nabla \times \vec{A_u}$. In the same region, we assume the existence of a co-propagating electromagnetic field: $\vec{E} = -\frac{1}{c}\frac{\partial \vec{A}}{\partial t}$ and $\vec{B} = \nabla \times \vec{A}$. Then the total vector potential is given by the sum of the two components:

$$\vec{\mathcal{A}}_{tot}(z,t) = \vec{\mathcal{A}}_u(z) + \vec{\mathcal{A}}(z,t) \tag{2.2}$$

where $\vec{\mathcal{A}}_u(z)$ is the vector potential produced by the undulator and $\vec{\mathcal{A}}(z,t)$ is the vector potential of the electromagnetic wave. The undulator magnetic field can be written as

$$\vec{A}_u(z) = \frac{a_u}{\sqrt{2}}\left(\vec{e}\exp[-ik_u z] + c.c.\right) \tag{2.3}$$

where a_u is the undulator parameter defined by 1.26, $k_u = 2\pi/\lambda_u$ and $\vec{e} = (\hat{x} + i\hat{y})/\sqrt{2}$ with $\hat{x}$ and $\hat{y}$ the orthogonal unit vector along the x and y axes transverse to $\hat{z}$. Likewise, the radiation field is defined as

$$\vec{A}(z,t) = -\frac{i}{\sqrt{2}}\left(\vec{e}\,a_s(z,t)\exp^{i\phi_s}\exp[i(k_s z - \omega t)] - c.c.\right) \tag{2.4}$$

---

ultra-short, high intensity pulses at the laser wavelength and its harmonics. Harmonics are produced in the extreme ultraviolet or soft x-ray region of the spectrum.

where $k_s = 2\pi/\lambda_s = \omega_s/c$, ϕ_s is the phase of the radiation field and $a_s = e\lambda E/(2\pi mc^2)$ represents the amplitude of the electromagnetic field, being $E = |\vec{E}|$ and m the electron mass. Its dependence on transverse coordinates (x and y) is neglected in the plane-wave and paraxial approximation.

The Newton-Lorentz equations drive the momentum and energy evolution of each electron:

$$\begin{cases} \dfrac{\mathrm{d}(\gamma m\vec{v})}{\mathrm{d}t} = e\left[\vec{E} + \dfrac{\vec{v}}{c} \times (\vec{B}_u + \vec{B})\right], \\ \dfrac{\mathrm{d}(\gamma mc^2)}{\mathrm{d}t} = e\vec{E}\cdot\vec{v}_\perp. \end{cases} \tag{2.5}$$

Since $\vec{B}_u \gg \vec{B}$ inside an undulator, it is the undulator field that determines the electron trajectory.

The transverse electron velocity can be derived from the first of Eqs. 2.5

$$\frac{\mathrm{d}}{\mathrm{d}t}(\gamma\vec{\beta}_\perp) = -\frac{\mathrm{d}}{\mathrm{d}t}(\vec{A}_u + \vec{A}_s) = -\frac{\mathrm{d}}{\mathrm{d}t}\vec{A}_{tot} \tag{2.6}$$

which gives for $\beta_\perp(0) = 0$, i.e. on-axis injection of electrons, and negligible initial field

$$\vec{\beta}_\perp = -\frac{A_{tot}}{\gamma}. \tag{2.7}$$

The electromagnetic field obeys the wave equation:

$$\left[\nabla^2 - \frac{1}{c^2}\frac{\partial^2}{\partial t^2}\right]\vec{A}(z,t) = -\frac{4\pi}{c}\mathbf{J}_\perp \tag{2.8}$$

where $\mathbf{J}_\perp$ is the average over the electron beam cross section of the transverse current density

$$\mathbf{J}_\perp(\mathbf{x},t) = e\sum_{j=1}^{N}\vec{v}^{\,j}_\perp\delta(\mathbf{x} - \mathbf{x_j(t)}). \tag{2.9}$$

In the slowly-varying envelope approximation (SVEA)

$$\left|\frac{\partial a}{\partial z}\right| \ll |ka|, \qquad \left|\frac{\partial a}{\partial t}\right| \ll |\omega a| \tag{2.10}$$

the second-order derivatives can be neglected and the equation for the field can be simplified according to

$$\frac{\partial^2}{\partial z^2} - \frac{1}{c^2}\frac{\partial^2}{\partial t^2} \simeq 2ik_s\left[\frac{\partial}{\partial z} + \frac{1}{c}\frac{\partial}{\partial t}\right]. \tag{2.11}$$

Since $\vec{a}$ is slowly-varying on the scale of a radiator wavelength λ, the transverse current can be averaged over a longitudinal distance several λ's long.

The final expression for the wave equation is [1, 2]:

$$\left[\frac{\partial}{\partial z} + \frac{1}{2ik_s}\nabla_T^2\right]a_s e^{i\phi_s} = i\frac{eZ_0}{mc^2}\frac{[JJ]}{2k_s}\frac{I_0}{N} \times \sum_{j=1}^{N}\delta(x - x_j)\delta(y - y_j)a_u(x_j, y_j)\frac{e^{-i\theta_j}}{\gamma_j} \tag{2.12}$$

where $Z_0 = 377\,\Omega$ is the vacuum impedance and each of the N particles carries the partial current I_0/N. The Bessel factor $[JJ]$, defined by

$$[JJ] = \begin{cases} J_0\left[\frac{a_u^2}{2(1+a_u^2)}\right] - J_1\left[\frac{a_u^2}{2(1+a_u^2)}\right] & \text{for planar undulator} \\ 1 & \text{for helical undulator,} \end{cases} \tag{2.13}$$

has been introduced to take into account the shape of the magnetic field.

Considering the electron phase $\theta = (k_s+k_u)z-\omega_s t$, relative to the radiation+undulator field, which propagates in the z direction at the phase velocity $v_p = \omega/(k+k_u)$. This expression can be derived in order to get the evolution of the phase. From the second of 2.5, we get

$$\frac{\mathrm{d}\gamma}{\mathrm{d}t} = \frac{e}{mc^2}\vec{E}\cdot\vec{v}_\perp \tag{2.14}$$

and after some algebra

$$\frac{\mathrm{d}\gamma}{\mathrm{d}t} = \frac{1}{2\gamma}\frac{\partial|\vec{A}_{tot}|^2}{\partial t}. \tag{2.15}$$

Considering the definitions of vector potentials and using the paraxial approximation $\mathrm{d}/\mathrm{d}t \simeq c\mathrm{d}/\mathrm{d}z$, we can obtain the equations for the longitudinal evolution of electrons [1, 2]:

$$\begin{cases} \dfrac{\mathrm{d}\gamma}{\mathrm{d}z} = -\dfrac{k a_u a_s [JJ]}{\gamma}\sin(\theta+\phi_s) \\ \dfrac{\mathrm{d}\theta}{\mathrm{d}z} = k_u - k_s\dfrac{1+a_u^2+p_x^2+p_y^2+2a_u a_s[JJ]\cos(\theta+\phi_s)}{2\gamma^2} \end{cases} \tag{2.16}$$

where p_x and p_y are the transverse momentum normalized to mc, averaged over an undulator period to cancel out the fast wiggle oscillations.

In the case of a planar undulator, the pole faces shaped to produce equal focusing in both horizontal and vertical planes and the undulator parameter may be redefined to have the transverse profile

$$a_u^* = a_u[1+\tfrac{1}{4}k_u^2(x^2+y^2)]. \tag{2.17}$$

Then p_x and p_y evolve according to

$$\frac{dp_x}{dz} = -\frac{1}{2\gamma}\frac{\partial}{\partial x}a_u^2, \tag{2.18}$$

$$\frac{dp_y}{dz} = -\frac{1}{2\gamma}\frac{\partial}{\partial y}a_u^2. \tag{2.19}$$

The former equations of motion 2.12 and 2.16 are single-particle equations and allow to follow the evolution of a single electron inside the electro-magnetic field. These equations are used in three-dimensional codes to simulate the FEL process inside the undulators.

2.2.2 1D model

Although the 3D model described above is more general and accounts for the three dimensional effects, here we want to review the simplified model presented in [3][3], which neglect transverse dimensions but allows to capture the essential features of the FEL process.

---

[3] This paper is just one of many review papers and books written on this subject and it is given here for convenience of the reader and because it has been used by the author. The references to the original work can be found therein.

In one-dimensional (longitudinal) approximation, the evolution of the electrons energy is:

$$\frac{\mathrm{d}\gamma}{\mathrm{d}z} = -\frac{k}{2}\frac{a_u}{\gamma}(a_s \exp[i\theta] + c.c.) \tag{2.20}$$

and the evolution of the phase is:

$$\frac{\mathrm{d}\theta}{\mathrm{d}z} = k_u - k_s \frac{1 + a_u^2 + i a_u (a_s \exp[i\theta] - c.c.) - |a_s|^2}{2\gamma^2}. \tag{2.21}$$

In the equation for the field evolution we disregard the transverse interaction between electron and electromagnetic field:

$$\left(\frac{\partial}{\partial z} + \frac{1}{c}\frac{\partial}{\partial t}\right) a_s = \frac{k}{2}\left(\frac{\omega_p}{\omega}\right)^2 \left(a_u \left\langle \frac{\exp(-i\theta)}{\gamma} \right\rangle - i a_s \left\langle \frac{1}{\gamma} \right\rangle\right) \tag{2.22}$$

where $\omega_p = \sqrt{4\pi e^2 n/m}$ is the plasma frequency, with n the total electron number density. The symbol $\langle ... \rangle$ represents the average over a sample of N electrons of a given function: $\langle f(\theta, \gamma) \rangle \equiv \frac{1}{n}\sum_{j=1}^{N} f(\theta_j), \gamma_j$. It is important to stress that we have assume a perfect coupling between the electron beam and the radiation in the transverse plane. This means that we suppose a complete overlap of the electron beam with the co-propagating wave. In a more general case a filling factor should be considered in order to model the space matching. This factor accounts for the not perfect overlap between transverse size of the electron bunch and the transverse dimension of the radiation field.

The Pierce parameter and the scaling

The so-called fundamental FEL parameter or Pierce parameter ρ is defined as:

$$\rho = \frac{1}{\gamma_r}\left(\frac{a_u}{4}\frac{\omega_p}{c k_u}\right)^{2/3}. \tag{2.23}$$

One can express the system of coupled evolution equations 2.20, 2.21 and 2.22 in a dimensionless form by means of ρ. For this purpose, it is convenient to redefine variables in the following way:

$$\Gamma_j \equiv \frac{\gamma_j}{\rho \langle \gamma \rangle_0} \tag{2.24}$$

$$\tilde{A} \equiv \frac{\omega}{\omega_p \sqrt{\rho \langle \gamma \rangle_0}} \exp[i\delta\bar{z}] a \tag{2.25}$$

$$\tilde{\theta_j} \equiv \tilde{\theta}_j - \delta\bar{z} \tag{2.26}$$

$$\bar{z} \equiv 2\left(\frac{\gamma_r}{\langle \gamma \rangle_0}\right)^2 k_u \rho z \tag{2.27}$$

$$\bar{t} \equiv 2\left(\frac{\gamma_r}{\langle \gamma \rangle_0}\right)^2 k_u \rho t \tag{2.28}$$

$$\tag{2.29}$$

where $\langle \gamma \rangle_0$ is the mean electron energy at the undulator entrance, $\gamma_r = \sqrt{\dfrac{\lambda_u(1 + a_u^2)}{2\lambda}}$ is the resonant energy (the energy that satisfies the Eq. 2.1) and δ is the energy-detuning parameter defined as:

$$\delta = \frac{1}{\rho}\frac{\langle\gamma\rangle_0^2 - \gamma_r^2}{\gamma_r^2}. \tag{2.30}$$

In the regime we are interested in (i.e., the so called Compton regime), the energy of the electron beam is high and the charge density is low, i.e., $\rho \ll 1$. Assuming the relative energy variation of electrons is:

$$\left|\frac{\gamma_j - \langle\gamma\rangle_0}{\langle\gamma\rangle_0}\right| \ll 1, \tag{2.31}$$

and defining the variable "momentum":

$$\tilde{p}_j = \Gamma_j - \frac{1}{\rho} = \frac{1}{\rho}\frac{\gamma_j - \langle\gamma\rangle_0}{\langle\gamma\rangle_0} \tag{2.32}$$

the equation for the evolution can be rewrite as:

$$\begin{cases} \dfrac{\mathrm{d}\tilde{\theta}_j}{\mathrm{d}\bar{z}} = \tilde{p}_j \\ \dfrac{\mathrm{d}\tilde{p}_j}{\mathrm{d}\bar{z}} = -\tilde{A}e^{i\theta_j} - \tilde{A}^* e^{-i\theta_j} \\ \dfrac{\mathrm{d}\tilde{A}}{\mathrm{d}\bar{z}} = i\delta\tilde{A} + \langle\exp[-i\tilde{\theta}]\rangle = i\delta\tilde{A} + \dfrac{1}{N}\sum_j e^{-i\theta_j} \end{cases} \tag{2.33}$$

where $b \equiv \langle\exp[-i\tilde{\theta}]\rangle$ is the electron bunching parameter and the temporal variable has been defined as $\bar{t}' = \bar{t} - (\bar{z}/\bar{v}_\parallel)$ ($\bar{v}_\parallel$ is the mean velocity of electrons).

In the third equation the derivative respect to the time has been neglected. Actually, the general equation is

$$\left[\frac{\partial}{\partial\bar{z}} - \frac{1}{c\bar{\beta}_\parallel}(1-\bar{\beta}_\parallel)\frac{\partial}{\partial\bar{t}'}\right]\tilde{A} = \langle\exp[-i\tilde{\theta}]\rangle + i\delta\tilde{A} \tag{2.34}$$

but one can normalize $\bar{z}$ respect to the undulator length L_u and $\bar{t}$ respect to l_b/c (where l_b is the bunch length) and therefore the ratio between the temporal and spatial derivative coefficients in the third equation becomes:

$$\frac{L_u(1-\bar{\beta}_\parallel)}{\bar{\beta}_\parallel l_b} = \frac{N_u\lambda_u(1-\bar{\beta}_\parallel)}{\bar{\beta}_\parallel l_b} = \frac{N_u\lambda_s}{l_b} \tag{2.35}$$

where N_u is the number of undulator periods. The term $N_u\lambda_s$ represents the *total slippage*, i.e. distance between the electrons and the radiation due to their different velocities. When the total slippage $N_u\lambda_s$ is much smaller than the bunch length l_b, the time derivative can be neglected. This regime is called "steady-state regime" and its evolution depend only on the longitudinal coordinate. The spatial coherence of the radiation is due to the slippage, because by means of this mechanism the wavefronts can talk each other. The radiation emitted by electrons in the bunch tail interacts with electrons located as far as the total slippage length.

Linear stability

Starting from an equilibrium state characterized by no initial field ($\tilde{A}_0 = 0$), zero bunching ($\langle \exp[-i\tilde{\theta}] \rangle_0 = 0$) and cold beam ($(p_j)_0 = 0$), we want to follow the evolution of the system until the wave reaches saturation. Equations 2.33, can be linearized and twofold differentiated with respect to $\bar{z}$, obtaining the third order differential equation:

$$\frac{\mathrm{d}^3}{\mathrm{d}\bar{z}^3}\tilde{A} - i\delta \frac{\mathrm{d}^2}{\mathrm{d}\bar{z}^2}\tilde{A} - i\tilde{A} = 0. \tag{2.36}$$

Searching a solution in the form $\tilde{A}(z) \sim \exp[i\lambda z]$ we obtain the well-known cubic equation for λ:

$$\lambda^3 - \delta\lambda^2 + 1 = 0. \tag{2.37}$$

Two situations are possible: if the solution is made of three real roots, the system is stable, if the solution corresponds to one real root ($\lambda = \lambda_1$) and two complex-conjugate roots ($\lambda = \lambda_2 \pm i\lambda_3$) then the system is unstable. In the latter case the field amplitude grows exponentially along the undulator as

$$\tilde{A}(z) \propto \exp[\lambda_3 \bar{z}] \equiv \exp[gz] \tag{2.38}$$

where g is the exponential gain per unit length and can be write as:

$$g = \lambda^3 \frac{4\pi\rho}{\lambda_u} \left(\frac{\gamma_r}{\langle \gamma \rangle_0} \right)^2. \tag{2.39}$$

The exponential growth lasts until nonlinear effects become preponderant and the field intensity starts to saturate (see 2.2.4).

Combining the first two equations of the system 2.33 one obtains:

$$\frac{\mathrm{d}^2\tilde{\theta}_j}{\mathrm{d}\bar{z}^2} = -2|\tilde{A}| \cos\left(\tilde{\theta}_j + \phi\right). \tag{2.40}$$

The previous equation shows that electrons can be considered as an ensemble of N coupled pendula with frequency $\sqrt{2|\tilde{A}|}$. The derivative of the phase $\dot{\phi}$ is related to the energy transfer from electrons to electromagnetic field. In particular conditions (no initial field excitation, no detuning and cold beam) one can demonstrate that:

$$\dot{\phi} \geq \frac{|\tilde{A}|^2}{4} \tag{2.41}$$

and accordingly

$$\frac{|E|^2/4\pi}{n\langle\gamma\rangle_0 mc^2} \leq 4\rho\dot{\phi} = \frac{2}{k_u}\frac{\mathrm{d}\phi}{\mathrm{d}z}. \tag{2.42}$$

There is a upper limit on the maximum energy that electrons can transfer to the field.

Gain function

The gain function can be defined as:

$$\mathcal{G}(\bar{z}, \delta) = \frac{|\tilde{A}|^2(\bar{z}) - |\tilde{A}|_0^2}{|\tilde{A}|_0^2} \tag{2.43}$$

In the exponential gain regime (see also Eq. 2.39) and using the original variable z, the intensity can be written as

$$|A|^2(z) \propto \exp[gz]|A|_0^2, \tag{2.44}$$

where

$$g = \sqrt{3}\,\frac{2\pi\rho}{\lambda_u} \tag{2.45}$$

is the exponential gain per unit length.

The total gain (before saturation) can be write as:

$$\mathcal{G} = gL_u = \sqrt{3}\,4\pi\rho N_u. \tag{2.46}$$

The high-gain regime is characterized by $G > 1$. In our case $\rho \ll 1$, so that z should be large enough, i.e., the undulator should be sufficiently long.

2.2.3 Small signal gain

Assuming that the system is close to resonance (small detuning), the short undulator condition can be write as $\bar{z}/\sqrt{\delta} \ll 1$. From linear calculation, the emitted field is

$$|A|^2(\bar{z}) \simeq \left[1 + \frac{4}{\delta^3}\left(1 - \cos(\delta\bar{z} - \frac{\delta\bar{z}}{2}\sin(\delta\bar{z}))\right)\right]|A|_0^2, \tag{2.47}$$

that, inserted in 2.43, gives the small signal gain

$$\mathcal{G}(\bar{z},\delta) = \frac{4}{\delta^3}\left(1 - \cos(\delta\bar{z}) - \frac{\delta\bar{z}}{2}\sin(\delta\bar{z})\right) \tag{2.48}$$

where

$$\delta\bar{z} = \frac{4\pi}{\lambda_u}\frac{\gamma_0 - \gamma_r}{\gamma_r}z. \tag{2.49}$$

This asymmetric curve (see Fig. 2.1) is equal zero at the resonance ($\delta = 0$) in contrast with the high-gain regime in which the at resonance the gain is maximum.

The Eq. 2.48 can be rewritten as:

$$\mathcal{G}(\bar{z},\delta) = -\frac{\bar{z}^3}{2}\frac{\mathrm{d}}{\mathrm{d}(\delta\bar{z}/2)}\mathsf{sinc}^2(\delta\bar{z}/2) \tag{2.50}$$

where $\mathsf{sinc} \equiv \sin x/x$.

At the end of the undulator, i.e., when $z = N\lambda_u$, the factor $\delta\bar{z}$ becomes

$$\delta\bar{z} \simeq 4\pi N_u\frac{\langle\gamma\rangle_0 - \gamma_r}{\gamma_r} = 2\pi N\frac{\omega - \omega_s}{\omega_s} \tag{2.51}$$

so that the small gain equation :

$$\mathcal{G}(x) \propto \frac{\mathrm{d}}{\mathrm{d}x}\mathsf{sinc}^2(x) \tag{2.52}$$

where $x = \pi N\frac{\omega-\omega_s}{\omega_s}$.

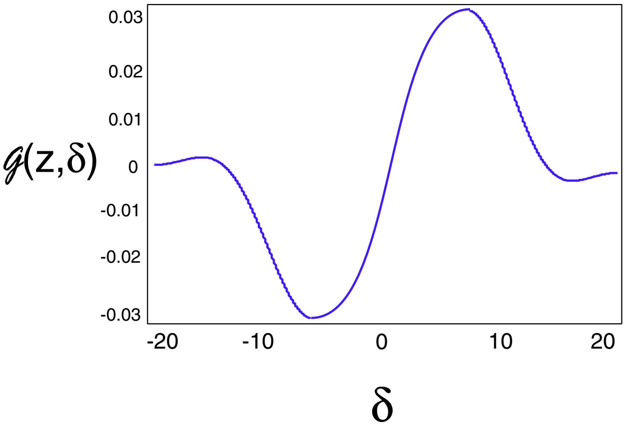

Figure 2.1: *Small signal gain at the end of the undulator.*

As the the spontaneous emission is characterized by the on-axis spectral distribution

$$\frac{\mathrm{d}^2 I}{\mathrm{d}\Omega \mathrm{d}\omega} \propto \mathsf{sinc}^2 \left(\pi N_u \frac{\omega - \omega_s}{\omega_s} \right) \tag{2.53}$$

peaked around the spontaneous frequency $\omega_s = 2\pi c/\lambda_s$ (where λ_s satisfied the usual resonance condition 2.1), one can argue that the small-signal gain is proportional to the derivative of the spontaneous emission spectrum, as found by Madey in [4]. Since the optical klystron spectrum has more fringes than the single undulator spectrum, it follows that in the first case the gain is bigger.

Bandwidths in small-signal gain and high gain regime

In the small signal gain regime the gain linewidth is of the order of the the spontaneous bandwidth $\Delta\omega/\omega \simeq 1/N_u$ (cfr. 1.41). Using the resonance condition (Eq. 2.1) one can see that $\Delta\omega/\omega = 2\Delta\gamma/\gamma_r$ and therefore that the energy dispersion of electron beam must be less than $1/(2N)$ to have an energy transfer from electrons to the field.

In the high gain regime, the gain linewidth is $\Delta\omega/\omega \simeq 4\rho$ [3].

2.2.4 Bunching

The resonance condition in small-signal gain is apparently in contrast with the high gain one. To solve this conflict we have to consider the longitudinal mean velocity of electrons ($\bar{v}_\parallel$) and the phase velocity (v_p) of the radiation+undulator field (ponderomotive field). An alternative picture of the resonance condition 2.1 is given by the following statement: for each undulator period where the electron passes through, the particle slippage with respect to the wave should be equal to one wavelength of the radiation. This is equivalent to:

$$\frac{\lambda_u (c - v_\parallel)}{v_\parallel} = \lambda_s. \tag{2.54}$$

Considering that $\frac{1}{\gamma^2} = 1 - \beta_\parallel^2 - \beta_\perp^2 = \frac{1}{\gamma_\parallel^2} - \frac{a_u^2}{\gamma^2}$ and $|\vec{\beta}_\perp| \simeq \frac{a_u}{\gamma}$ and assuming that $\lambda_s = \frac{\lambda_u}{2\gamma_\parallel^2}$ (that is true if $(1 - \beta_\parallel) \ll 1$), after some algebra one can find the resonance condition defined by Eq. 2.1.

When an electron beam starts to interact with an electromagnetic wave, all the particles are randomly distributed in phase with respect to the wave, as shown in Fig. 2.2a.

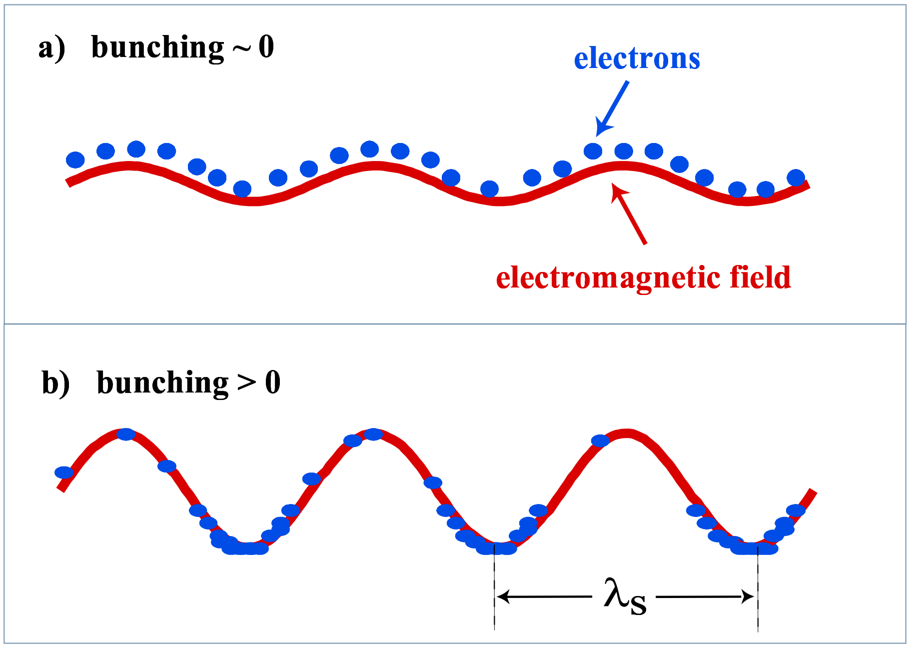

Figure 2.2: *Bunching evolution. a)electrons randomly distributed in phase (initial condition: weak electromagnetic field) b) electrons start bunching on a λ_s scale and the wave is amplified.*

As the resonance condition is satisfied, i.e. $\bar{v}_\parallel = v_p = \omega/(k + k_u)$, half of particles absorb energy from the electromagnetic wave and the other half transfer energy to the wave because the particles tends to cluster where the ponderomotive phase is zero (see Fig. 2.2b), and hence the amplification is zero.

But, when the electromagnetic field of the ponderomotive wave change remarkably, as in the high gain regime, also the phase velocity changes, according to

$$v_p = \frac{\omega - \dot{\phi}}{k + k_u} \tag{2.55}$$

where $\dot{\phi}$ satisfies the Eq. 2.41. As $\dot{\phi} > 0$, the latter relation states that the electrons act as a dielectric medium slowing down the phase velocity of the ponderomotive wave. The velocity of the resonant electrons is then $\bar{v}_\parallel > v_p$ and they bunch around a phase where there is positive gain.

Figure 2.3 explains the saturation mechanism, as it occurs in the electron phase space (γ, θ). The interaction with the ponderomotive wave induces a modulation of the electrons' energy. This energy modulation evolves in spatial modulation, also called bunching. When electrons exceed the wave of a phase equal to a quarter of the ponderomotrice force period there is maximum gain. As the beam proceeds further inside the undulator, the spatial modulation arises also where the ponderomotive force is positive and this causes "over-bunching". Here the process reaches the saturation because the electrons are not anymore able to transfer their energy to the wave. The saturation is not a stationary state because the system do not arrive in an equilibrium condition.

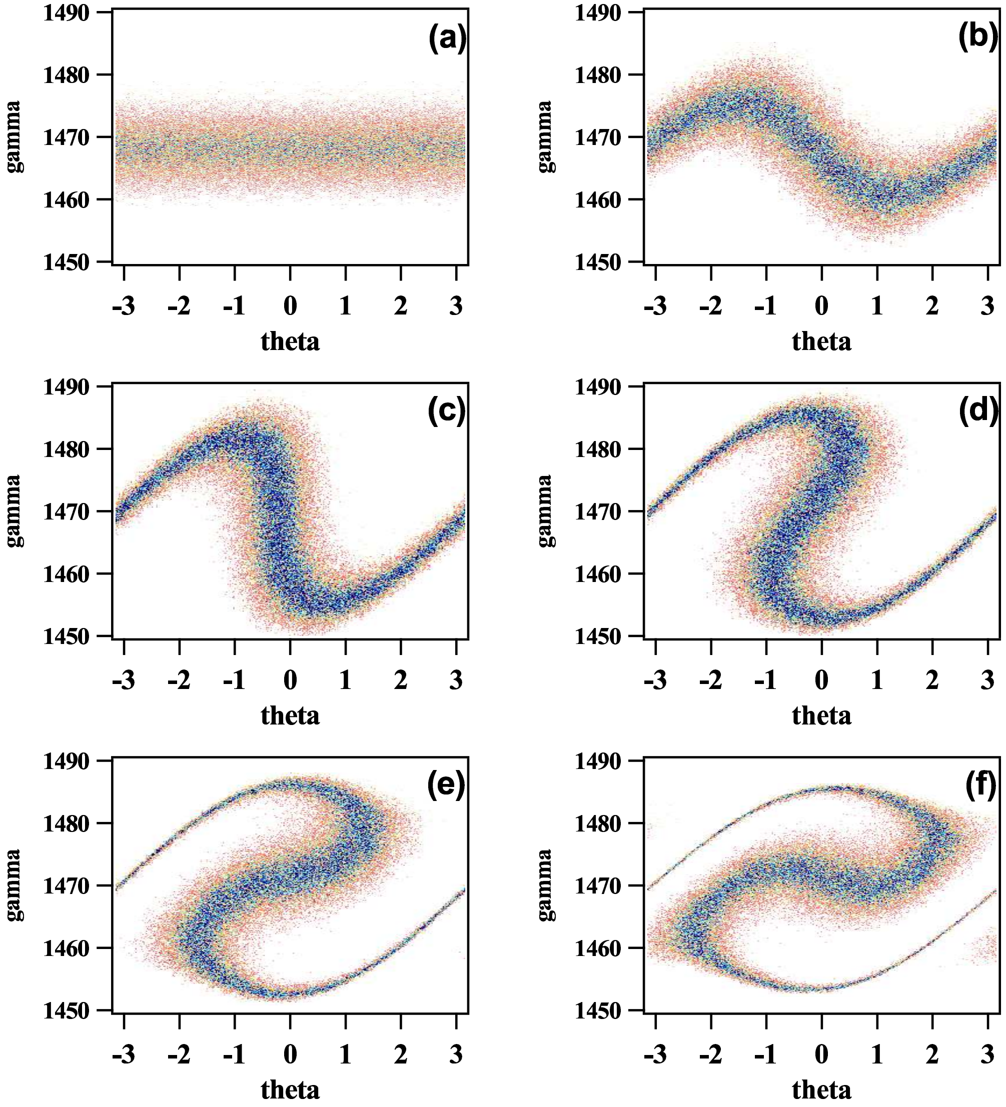

Figure 2.3: *Evolution of the electron-beam phase space. a) initial distribution, b) energy modulation c) spatial modulation (bunching) d) slightly overbunching e-f) overbunching.*

The evolution of the spatial separation of the electrons at the scale of the resonant wavelength is schematically shown in Fig. 2.4.

2.2.5 3D effects

So far the transverse dimensions of the electron beam and its angular divergence have been neglected, as well as the diffraction of the light. Besides, the hypothesis of monoenergetic beam (mentioned at the very beginning of the derivation of the equations) is far from reality: an electron beam has an intrinsic energy-spread and this affects the performance of the source.

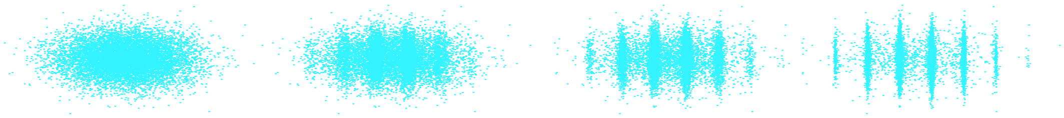

Figure 2.4: *How the spatial separation (bunching) evolves in an electron bunch.*

The emittance $\epsilon = r\Delta\theta$ is the quantity that takes into account the transverse dimension r and the angular dispersion $\Delta\theta$ of the electron bunch. According to the Liouville theorem, if the beam is not accelerated, the emittance is a constant of motion and can be defined as the area occupied by the beam in its phase space. When the transverse dimensions of the electron beam and the laser are equal, the coupling is maximum and all electrons participate at the wave amplification. Assuming a Gaussian laser beam mode, the diffraction can be neglected if the Rayleigh length (defined as the distance from the beam waist at which the transverse dimension is increased by a factor $\sqrt{2}$, $z_R = \dfrac{\pi w_0^2}{\lambda}$ where w_0 is the waist of the radiation) is significantly larger than the undulator length (L_u). The transverse dimension of the radiation is $w_0 \simeq \sqrt{\lambda L_u}$ and its angular divergence is $\Delta\theta \simeq \sqrt{\lambda/L_u}$ at the "diffraction limit", i.e. when the radiation dimensions dominate the electron beam dimensions. The transverse area is then $w_0\Delta\theta \simeq \lambda$ and the optimal overlap can be obtained if $\epsilon \leq \lambda$. This condition is more critical as the wavelength becomes shorter.

A real electron beam is also characterized by an energy distribution $f(\gamma)$. Solving the linearized evolution equations, the dispersion relation that determines the stability of the system can be write as:

$$\lambda - \delta + \int_{-\infty}^{\infty} \mathrm{d}\gamma \frac{f(\gamma)}{(\lambda+\gamma)^2} = 0. \tag{2.56}$$

Considering for example a rectangular distribution with half-width μ such as $f(\gamma) = \dfrac{1}{2\mu}$ if $-\mu \leq \gamma \leq \mu$ and $f(\gamma) = 0$ elsewhere, the cubic equation becomes:

$$(\lambda - \delta)(\lambda^2 - \mu^2) + 1 = 0. \tag{2.57}$$

When $\mu \geq 1$ the instability field becomes tighter around the maximum value $\delta = \mu$ and the maximum gain decreases proportionally to $(2\mu)^{-1/2}$. Therefore the width μ of the distribution strongly suppresses the exponential gain.

2.3 Oscillator configuration

In the spectral regions where high reflectivity mirrors are available, a FEL in oscillator configuration can in general produce radiation with high spectral purity and excellent temporal stability. Although the oscillator configuration can be implemented also with linear accelerator, several FELs has been installed in storage rings and in this section we present the general characteristics of this kind of device, which has a more complex dynamics than single-pass FELs because the electrons are recirculated. When the intracavity power grows, the amplification causes an increase in the electron beam energy-spread. As a consequence, during the interaction the gain decreases because it is an inverse function of the energy spread (see Section 1.2.2). The saturation is reached when the gain becomes equal to the cavity losses.

2.3.1 3D theory

The equations that can be used to describe the FEL process inside the undulator (or the optical klystron) are essentially the same as the single-pass theory. The additional ingredient is the optical cavity that has to be included in the equation for the space-time evolution of the electric field. Besides, in the case of the storage-ring FEL one has to take into account the electron beam dynamics during successive turns of the particles in the ring. This is possible considering both the longitudinal and the transverse motion of electrons after their passage through the undulators.

Evolution of the electromagnetic wave in the optical cavity

Starting from the usual wave equation

$$\left[\nabla^2 - \frac{1}{c^2}\frac{\partial^2}{\partial t^2}\right]\vec{A}(z,t) = \mu_0 \frac{\partial \mathbf{j}_\perp}{\partial t} \tag{2.58}$$

and applying the paraxial approximation ($\frac{\partial^2}{\partial z^2} - \frac{1}{c^2}\frac{\partial^2}{\partial t^2} \simeq 2ik_s\left(\frac{\partial}{\partial z} + \frac{1}{c}\frac{\partial}{\partial t}\right)$) one can derives the propagation of an electromagnetic wave:

$$\left(\Delta_\perp + 2ik_s\frac{\partial}{\partial z}\right)a_s e^{i\phi} + \frac{1}{c}\frac{\partial}{\partial t}a_s e^{i\phi} = \mu_0\frac{\partial \mathbf{j}_\perp}{\partial t} \tag{2.59}$$

that, neglecting the temporal derivative (because a_s is slowly varying with respect to the time) and considering that the right term is zero (because there are not sources), reduces to

$$\left(\Delta_\perp + 2ik_s\frac{\partial}{\partial z}\right)a_s e^{i\phi} = 0. \tag{2.60}$$

The reflected field from the mirrors is calculated as

$$a_{ref}(x,y,z_0) \approx a_{inc}(x,y,z_0)e^{2ik_s z_M} \tag{2.61}$$

where $a_{inc}(x,y,z_0)$ represents the incident field and $z_M = z_0 - r^2/2R_M$ with $r = \sqrt{x^2+y^2}$ and R_M is the radius of curvature of the mirror.

In fact, the expression 2.61 can be further simplified considering the two following approximations:

- for the first turns, we can consider that all the emitted radiation is collected by the mirrors of the optical cavity and is stored there. Actually the electron beam has a waist a factor about ten smaller than the radiation one. As a consequence, the divergence of the radiation emitted in one passage by electrons is bigger than the spontaneous emission (see Fig. 2.5). This approximation corresponds to overestimate the gain of the optical cavity for the first 20-30 turns.
- the phase information carried by the radiation emitted by electrons can be neglected to account for the light monochromatization operated by the optical cavity.

Although these two approximations are coarse for the first turns of electrons in the storage ring (or round trips of radiation in the optical cavity) after about 100 turns (typically) they become quite realistic.

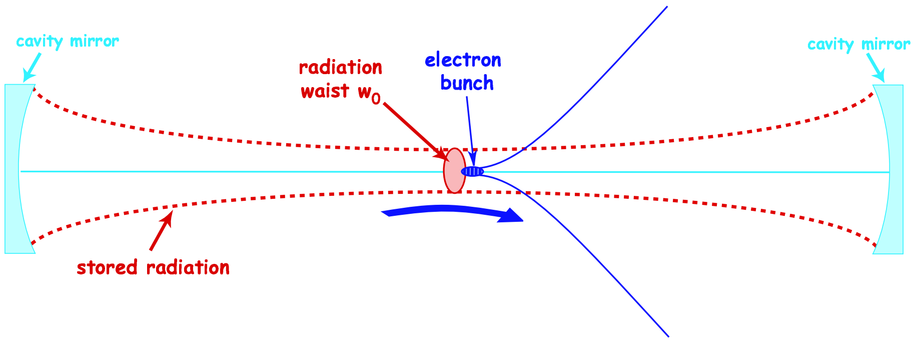

Figure 2.5: *Schematic representation of the bunch emission and the stored radiation in the optical cavity for the first interactions.*

Using a simplified approach we do not take into account the propagation of the mode, which is assumed to be fixed, its evolution in the optical cavity and the possibility of multi-mode creation in the cavity.

The equation that controls the evolution of the stored radiation can be then written, at pass n, neglecting the phase term and just considering the reflectivity R of the mirrors:

$$a_{n+1}(x, y, z_0) \approx a_n(x, y, z_0)R. \tag{2.62}$$

Evolution of the electrons along the ring

The electron beam propagation along the ring follows the Eqs. 1.21 for the longitudinal part and the Eqs. 1.4 and 1.5 for the transverse motion. Equations 1.21, 1.4 and 1.5 have been implemented in a single-particle code that simulates the evolution of the electron beam along the storage-ring. This code is coupled with a 3D FEL code (Ginger [5]) to simulate the whole process.

2.3.2 Dynamics on different time scales

In a storage ring the synchrotron radiation is naturally pulsed at the electron beam revolution period (i.e. usually hundreds of ns) because every single light pulse is produce by an electron bunch. Since the FEL process initiates from the spontaneous emission of electrons, it is pulsed at the same frequency. This temporal characteristic is shown in Fig. 2.6 where the pulsed structure of the radiation is detected using a streak camera. This temporal scale is called “micro-temporal” because the pulsed behavior of the FEL light can be appreciated on a time of the order of micro-seconds.

The micro-pulse is characterized by a Gaussian shape, as the spontaneous emission pulse. In reality, the Gaussian shape is the envelope of a spiky structure. The origin of the spikes comes from the initial emission of an electron bunch, that is not Gaussian but spiky, and in the evolution conserves its nature. This feature is in common with the SASE process, that starts from noise and preserves spiky structures. The case of the seeding is different: the emission comes from micro-bunches that are composed of electrons with the same phase. As a consequence the radiation inherits the pulse shape of the seed laser that is normally Gaussian.

On a longer (milliseconds) temporal scale, the FEL dynamics depends on the temporal overlap between the electron bunch and the light pulse at each pass inside the optical

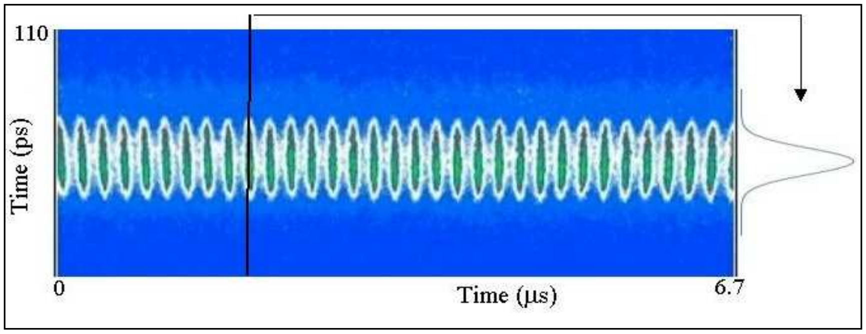

Figure 2.6: *Micro-temporal structure of the FEL radiation. A vertical cut on the picture shows the Gaussian profile of the light. On the horizontal scale one can follow the temporal evolution of the radiation.*

cavity. The temporal overlap is perfect when the electron beam revolution period matches the photons round trip into the optical cavity, as shown in Fig. 2.7. The temporal overlap can be modified either altering the electron-beam revolution period or changing the optical cavity length. The former is preferred because one can act a finer control on the RF frequency while moving the mirror positions usually allows only a coarse tuning.

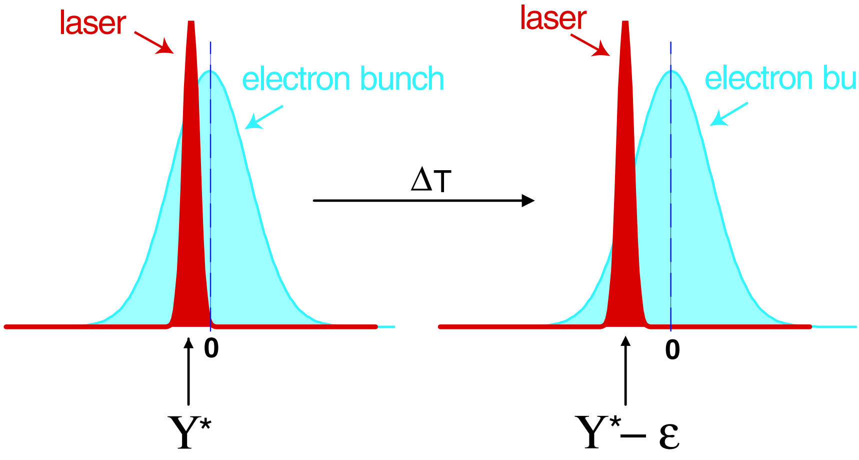

Figure 2.7: *Schematic layout of the pass-to-pass laser electron beam interaction.* ΔT *stands for the period between two successive interactions,* Υ^* *is the position of the laser centroid with respect to the peak of the electron density and* ϵ *accounts for the laser-electron beam delay at each pass.*

The intensity of the stored light is a function of the temporal overlap.Figure 2.8 shows the intensity as a function of the temporal overlap in the case of SuperACO SRFEL.

For an intermediate delay amount, the laser intensity appears with a pulsed behavior whereas for a small or big delay, the laser intensity shows a “continuous wave” (CW) trend. This curve is symmetric with respect to the perfect overlap and in the case of Fig. 2.8 the central CW zone is well visible.

Second generation SRFELs, like Super ACO and UVSOR, display the CW zone and have implemented feedback systems to keep the laser-electron beam synchronism and avoid jittering. In the CW regime the laser has the maximum average power and the

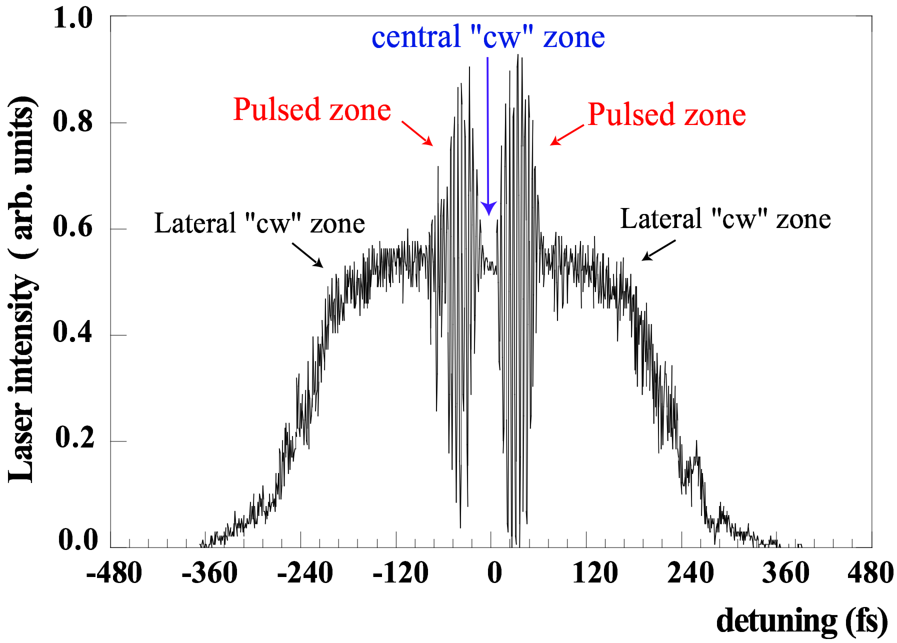

Figure 2.8: *Intensity as a function of the temporal overlap in the case of SuperACO SRFEL.*

signal is close to the Fourier limit. The transition between the CW and the pulsed regime is shown to be a Hopf bifurcation [6]. In the SRFELs (like Elettra) installed on third generation storage rings the CW zone is not visible (see Fig. 2.9) because these devices are very sensitive to electron beam instabilities. The sources of instability will be discussed in the next section.

2.3.3 Heuristic model for the SRFEL

The 3D model which includes the evolution equations for electrons and for the electromagnetic field plus the one-turn map, that account for the electron motion along the storage ring, describes the FEL process in oscillator configuration in detail and reproduces very carefully the laser evolution. Nevertheless, the micro-temporal dynamics of the FEL can be also described by means of a simpler model that account for the evolution of statistical macroscopic parameters and which is useful to explain some characteristics of a SRFEL.

In this model we include the presence of the optical cavity (with finite losses of mirrors) and we consider the emission of the optical klystron. Besides, the recirculation of the beam implies that the electron bunch heats up (increase its energy spread and bunch-length) progressively (gradually) during the interaction with the electromagnetic wave. The temporal overlap between electrons and photons fixes the dynamical regime (as will be shown soon) and as a consequence the level of intensity at saturation. The model presented in the follow is based on the evolution of the temporal profile of the laser intensity coupled with that of the electron-beam energy spread.

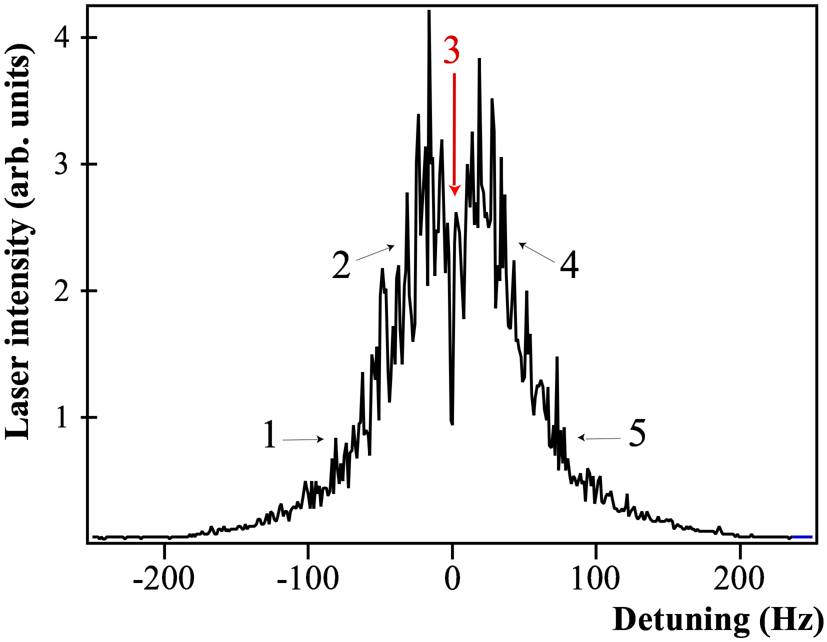

Figure 2.9: *Intensity as a function of the temporal overlap in the case of Elettra SRFEL. The* CW *zone (3) is not visible.*

Temporal evolution of the laser profile

In the ideal condition, the evolution of the light intensity $I(t)$ can be deduced assuming at the beginning an exponential trend for the intensity

$$I(t) \sim \exp\left(\frac{t}{\Upsilon_0(t)}\right) \tag{2.63}$$

where $\Upsilon_0(t) = \dfrac{T_0}{g(t) - L}$ is the variable growth parameter, T_0 is the round trip of photons in the optical cavity, L stays for the mirror losses and $g(t)$ is the gain in the amplification process, that has been defined in 2.72.

Using the equation 2.63 and neglecting the contribution of the gain variation due to a single interaction, one can write:

$$\frac{\mathrm{d}I}{\mathrm{d}t} \simeq \frac{I_{n+1} - I_n}{T_0} \simeq \frac{(g_n - L)}{T_0} I_n + i_s \tag{2.64}$$

where n and $n+1$ represent the interaction number and i_s is the initial intensity, i.e., the emission from the optical klystron. Now we introduce the variable Υ that accounts for the temporal position of the electron bunch centroid with respect to the laser centroid (see Fig. 2.7). Using this variable one can generalize the previous equation taking into account the evolution of the temporal distribution for the light pulse (of which the intensity is the integral) and, as a consequence, for the gain:

$$I_{n+1}(\Upsilon) = I_n(\Upsilon - \epsilon)[1 + g_n(\Upsilon) - L] + i_s(\Upsilon) \tag{2.65}$$

where ϵ accounts for the temporal delay between the the light pulse and the electron bunch that can eventually arise at each pass through the optical klystron. It is defines as $\epsilon = T_e - T_0$, with T_e the revolution period of electrons.

Assuming the losses in the optical cavity small enough, the latter equation can be written in the form:

$$I_{n+1}(\Upsilon) \simeq R^2 I_n(\Upsilon - \epsilon)[1 + g_n(\Upsilon)] + i_s(\Upsilon) \tag{2.66}$$

where R is the mirror reflectivity[4], i.e. the fraction of incident radiation reflected by the mirror surface and $R^2 = (1 - L)$.

Temporal evolution of the gain

The gain distribution ($g_n(\Upsilon)$) depends on the electron beam profile ($h_n(\Upsilon)$) and the modulation rate (f_n) of the optical klystron emission:

$$g_n(\Upsilon) = \alpha f_n h_n(\Upsilon) \tag{2.67}$$

with the constant α depending on the initial values of the modulation rate f_0 and the peak gain g_i in correspondence of the centroid ($\Upsilon = 0$) of the electron distribution h_0: $\alpha = g_i/[f_0 h(0)]$. It can be demonstrate that g_i is connected to the Pierce parameter ρ (defined by 2.23) by $g_i = \pi^2(4N\rho)^3$. The equation for the gain is then:

$$g_n(\Upsilon) = g_i \frac{f_n}{f_0}\frac{h_n(\Upsilon)}{h(0)}. \tag{2.68}$$

Omitting the details of the derivation, one can use the following results:

$$\frac{f_n}{f_0} = \exp\left[-\frac{\sigma_n^2 - \sigma_0^2}{2\sigma_0^2}\right] \tag{2.69}$$

and

$$\frac{h_n(\Upsilon)}{h(0)} = \frac{\sigma_0}{\sigma_n}\exp\left[-\frac{\Upsilon^2}{2\sigma_{\Upsilon,n}^2}\right] \tag{2.70}$$

where it has been assumed that the electron beam profile is Gaussian and σ_0 and σ_n are the initial[5] value of the energy spread and the value at the n-interaction respectively; $\sigma_{\Upsilon,n}$ is the standard deviation of the temporal distribution of the electron beam[6]. Using the latter equations, the gain can be write as:

$$g_n(\Upsilon) = g_i \frac{\sigma_0}{\sigma_n}\exp\left[-\frac{\sigma_n^2 - \sigma_0^2}{2\sigma_0^2}\right]\exp\left[-\frac{\Upsilon^2}{2\sigma_{\Upsilon,n}^2}\right]. \tag{2.71}$$

Optical klystron Gain

One can defines the gain as the proportional energy increase of the electromagnetic wave (assuming a Gaussian mode TEM00). In practical form, the maximum gain obtained by an optical klystron is expressed by [7]:

$$G = 2.22 \cdot 10^{-13} a_u^2 (N\lambda_u)^2 [J_1(\xi) - J_0(\xi)]^2 F_f \frac{(N + N_d) f I_{tot} T_0}{\gamma^3 e (2\pi)^{1.5} \sigma_x \sigma_y c \sigma_\tau} \tag{2.72}$$

---

[4] The mirrors of the optical cavity are optimized to reflect a narrow band around a central wavelength and satisfy the condition R+T=1 where T is the transmission

[5] Before to start to accumulate light in the cavity

[6] In case of weak wake fields (see next paragraph), this parameter is linearly proportional to the energy spread

where $\xi = a_u^2/(4+2A_u^2)$, J_1 and J_0 are the Bessel functions, F_f is the filling factor, I_{tot} is the total current stored in the ring, T_0 is the inter-bunch period, $\sigma_{x(y)}$ are the transverse dimensions of the beam (calculated from the beam emittance ϵ and the β-functions as $\sigma = \sqrt{\epsilon\beta}$) and σ_τ is the bunch duration in time.

Temporal evolution of the energy spread

There are two contribution to the energy spread: the initial value σ_0 when the laser is off (that for low current corresponds to the natural energy spread) and the amount induced by the light amplification process σ_i.

These two contributions are sum up as:

$$\sigma^2 = \sigma_0^2 + \sigma_i^2. \tag{2.73}$$

Two phenomena are in competition in the evolution of the induced energy spread. One is the interaction with the light stored in the optical cavity, that increases the energy-spread, and the relaxation due to synchrotron radiation in the whole ring, that is responsible for an energy-spread reduction. If Υ_s is the characteristic time for the relaxation process, a differential equation can be write for the energy spread evolution:

$$\frac{\mathrm{d}\sigma_i^2}{\mathrm{d}t} = -\frac{2}{\Upsilon_s}\sigma_i^2 + \hat{\alpha} I \tag{2.74}$$

or

$$\frac{\mathrm{d}\sigma^2}{\mathrm{d}t} = -\frac{2}{\Upsilon_s}(\sigma^2 - \sigma_0^2) + \hat{\alpha} I. \tag{2.75}$$

Imposing the equilibrium condition (saturation) $\mathrm{d}\sigma^2/\mathrm{d}t = 0$, one can derive the constant $\hat{\alpha}$:

$$\alpha = \frac{1}{I_e}\frac{2}{\Upsilon_s}(\sigma_e^2 - \sigma_0^2) \tag{2.76}$$

where I_e is the intra-cavity intensity and σ_e is the energy spread at the equilibrium. Transferring into a discrete equation one gets:

$$\sigma_{n+1}^2 = \sigma_n^2 - \frac{2\Delta T}{\Upsilon_s}\left[\sigma_n^2 - \sigma_0^2 - (\sigma_e^2 - \sigma_0^2)\frac{I_n}{I_e}\right]. \tag{2.77}$$

Summarizing, the longitudinal dynamics of a SRFEL can be described by the system made of Eqs. 2.66, 2.71, 2.77, that account for the coupled evolution of the electromagnetic field and of the longitudinal parameters of the electron bunch. What is left is the single particle evolution and the so-called “phase space refreshment” due to synchrotron motion. This mechanism plays, as it will be described in the following, an important role on the giant pulses regime that will be described in the next chapter.

Saturation

As already mentioned, the phenomena concurring at the saturation process in an oscillator FEL are actually two:

- the growth of the electron beam energy spread
- the non-perfect temporal overlap between the electron beam and the laser pulse

When the energy spread increases, the gain decreases (Eq. 2.71) until it matches the cavity losses $g_n(\Upsilon^*) = P$ and the time derivative of the intra-cavity intensity (Eq. 2.65) becomes zero. If the temporal overlap is such that the system is in the central or lateral CW zones, the equilibrium is stable. On the other hand, if the system is in the pulsed zones (see Fig. 2.8), the equilibrium is instable.

Besides, the typical delay ϵ is on the order of few fs but it induces a cumulative delay between the electron bunch and the laser pulse corresponding to some ps. Because the gain is maximum when the total delay is zero ($g_n(\Upsilon^*) < g_n(0)$), from the equation 2.66 it is clear that also the stationary intensity is greater near the perfect tuning with respect to worse temporal overlap.

In conclusion, the evolution of FEL statistical parameters (such as the intensity, the centroid position and the standard deviation of the radiation, the energy spread of the electron beam) can be follows using Eqs. 2.66, 2.71, 2.77. The different dynamical regimes are determined by the ϵ parameter and can be simulated implementing the equations of the model, as reported in Fig. 2.10

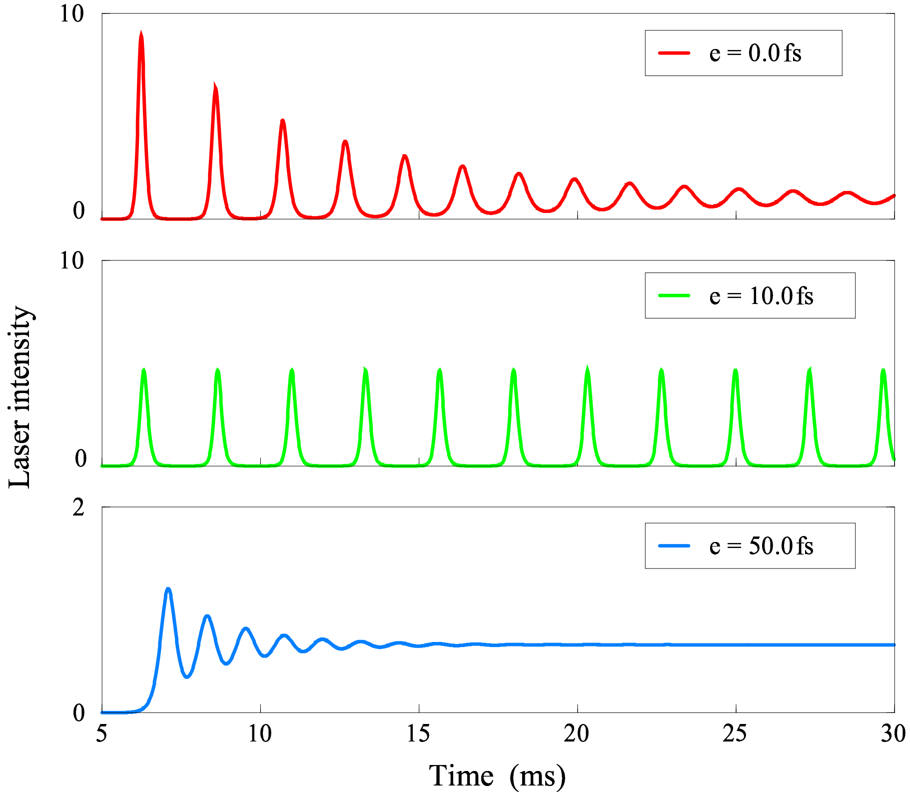

Figure 2.10: *Numerical simulation performed for the case of SuperACO SRFEL. The different regimes displayed in Fig. 2.8 are reproduced.*

2.3.4 Instabilities

A non-exhaustive list of instabilities that can affect a SRFEL includes:

- white noise from the RF system

- periodic noise at 50 Hz and its harmonics
- wakefields
- periodic instabilities from magnets power supplies

The interaction of the electron beam with the vacuum chamber is one of the main source of instabilities. Especially in a SRFEL operation, when the charge per bunch is quite big, the electrons interact with the metallic beam pipe, producing the so-called wake fields. These fields react on the beam perturbing its trajectory and also the bunch shape. The wake fields are stronger in presence of low-gap vacuum chambers and discontinuities in the beam pipe (valves, bellows and so on). Also mechanical vibrations are sources of perturbation as well as the electric supplies, that induce the 50 Hz perturbation on the beam. This effect is more pronounced when the storage ring is operated at the lowest energy (0.75 GeV) because the power supplies of magnets (especially the bending magnets) are at the lower limit of their operational range.

2.3.5 Renieri limit

The maximum power that a SRFEL can be extracted from an electron beam can be calculated using the so-called "Renieri limit". In the case of an optical klystron the predicted output power is:

$$P_{sLaser} = \eta_c 8\pi (N + N_d) f \Delta \left(\frac{\sigma_\gamma}{\gamma} \right)^2 P_s \tag{2.78}$$

where η is the ratio between the transmission and the total losses of the optical cavity and $\Delta \left(\frac{\sigma_\gamma}{\gamma} \right)$ is the variation of the energy spread square due to the saturation. P_s is the total synchrotron emission radiated by the electron bunch along the whole ring and in practical units can expressed as:

$$P_s(W) = 6.04 \cdot 10^{-9} \frac{\gamma^4 I(A)}{\rho_0(m)}. \tag{2.79}$$

where ρ_0 is the radius of the bending magnets.

The Renieri limit is valid in the "free running" regime

Bibliography

[1] S. Krinsky and L. H. Yu, *Phys. Rev. A* **35**, 3406 (1987)

[2] L. H. Yu, *Phys. Rev. A* **44**, 5178 (1991)

[3] R. Bonifacio, F. Casagrande, G. Cerchioni, L. De Salvo Souza, P. Pierini and N. Piovella, *"Physics of the High-Gain FEL and Superradiance"*, Il Nuovo Cimento, vol.13, N.9 (1990)

[4] J. Madey, *J.of Appl.Phys.* **42**, 1906 (1971)

[5] W. Fawley, Report No. LBNL-49625, LBL, 2002

[6] G. De Ninno and D. Fanelli, *Phys. Rev. Lett.* **92**, 094801 (2004)

[7] P. Elleaume, *Ph.D. thesis*, Université de Paris-Sud, Centre d'Orsay (1984)

Chapter 3

Harmonic Generation

The generation of coherent harmonics using a FEL is possible either in single pass or in oscillator configuration.

In the single pass case, the usual configuration for Harmonic Generation relies on the seeding technique (i.e., the use of an external laser) and makes use of two undulators: the first undulator is tuned at the same wavelength of the external laser and the second one is tuned at the selected harmonic.

In the oscillator configuration both undulators are tuned at the same (fundamental) wavelength and the (fundamental) field stored in the optical cavity acts as a seed for harmonic generation. The optical cavity stores only the fundamental radiation while the harmonics are produced in a single-passage interaction.

In this chapter we discuss the fundamental principles of the Harmonic Generation (HG) process both in single-pass and oscillator configurations.

3.1 Harmonic Generation in single pass configuration

In Ch. 2 we have introduced the system of Eqs. 2.33, which account for the evolution of a single-pass FEL in the case of a single (fundamental) optical wavelength. As shown in [1], such a model can be simply generalized to account also for the evolution of the optical field at the harmonics of the fundamental. In the case of a planar undulator and observing the radiation along the propagation axis (i.e., considering only odd-order harmonics), one can find:

$$\begin{cases} \dfrac{\mathrm{d}\theta_j}{\mathrm{d}\bar{z}} = p_j \\ \dfrac{\mathrm{d}p_j}{\mathrm{d}\bar{z}} = -\sum_h F_h(\xi)(A_h \exp[ih\theta_j] + c.c.) \\ \dfrac{\mathrm{d}A_h}{\mathrm{d}\bar{z}} = F_h(\xi)\langle\exp[-ih\theta]\rangle \equiv F_h(\xi) b_h \end{cases} \tag{3.1}$$

where h runs over the harmonic components of the field and F_h is the difference of Bessel functions defined as

$$F_h(x) = (-1)^{(h-1)/2}\left[J_{(h-1)/2}(hx) - J_{(h+1)/2}(hx)\right] \tag{3.2}$$

and $\xi = a_u^2/(1+a_u^2)2$ where a_u is the undulator parameter defined by 1.26. The parameter $b_h \equiv \langle\exp[-ih\theta]\rangle$ is the electron bunching at the h-th harmonic field component. Figure 3.1 shows the phase space (γ, θ) of a modulated electron distribution where the buckets with different periodicity are represented for the fundamental, the third and the fifth harmonic.

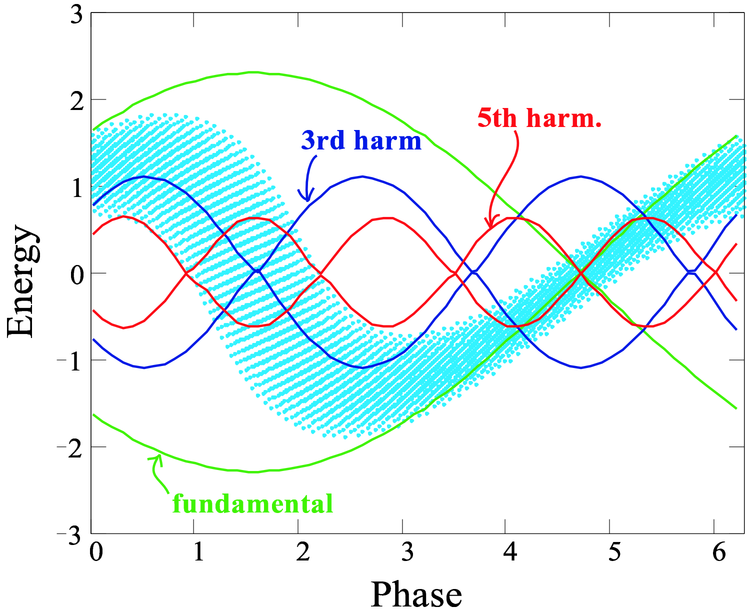

Figure 3.1: *Phase Space of the electron beam distribution. The harmonic buckets are shown together with the fundamental.*

The bunching at the h-th harmonic is related to the fundamental bunching b_1 by:

$$|b_h(\bar{z})| \approx |b_1(\bar{z})|^h \, . \tag{3.3}$$

Numerical integration of Eqs. 3.1 shows that, at saturation, the fundamental and harmonic components of the bunching reach almost identical values, of the order of unity. On the other hand, the harmonic radiation reaches a power level substantially smaller than the fundamental and becomes smaller and smaller as the harmonic number increases[1]. A much more efficient configuration is obtained when the harmonic bunching created in the first undulator is exploited in a subsequent stage. This configuration is discussed in the next Section.

3.1.1 Seeded Harmonic Generation

The possibility to use a configuration with two undulators has been considered for the first time in [2]. In this configuration, the first undulator is long enough to reach almost saturation at the fundamental wavelength. The electron beam is extracted from the first undulator (caller modulator) when the energy modulation and the spatial bunching (with its components) are maximum. The second undulator (called radiator) is tuned at one harmonics of the fundamental wavelength in the first undulator. Since the bunch is already prepared to emit, the saturation is reached in a relatively small number of

---

[1] Harmonics, and harmonic bunching generated in a single pass SASE amplifier have been measured in many experiments and in fact they could be amplified using the fresh bunch technique in a second undulator tuned to the new frequency.

undulator periods. The emission process that occurs when the electron beam is already bunched is called *superradiant* emission. In [3] L.H.Yu has introduced some modifications to the former scheme:

- an external laser induces the energy modulation and allows to control it remaining far away from saturation;
- as a consequence, the modulator can be shorter and one can make the energy modulation comparable to the energy spread;
- a dispersive section, placed between the two undulators, helps the conversion of the energy modulation in bunching;
- the radiator is much longer than the modulator and the growth of the radiation is initially quadratically (superradiance) and then becomes exponential (up to saturation);
- in the last portion of the radiator, the magnetic field can be modified (tapering) in order to maintain the resonance condition (see Eq. 1.38) and enhance the extracted power.

The induced energy modulation is controlled in the first undulator in order to avoid two unwanted effects: if the energy modulation is too small, there is no enough harmonic components in the bunching; on the other hand, if the energy modulation is too large, it acts like energy spread in the second undulator spoiling the FEL emission.

The Harmonic Generation principle [4, 5, 6, 1] in a single-pass FEL can be explained dividing the process in three steps, ideally separated. A schematic picture of the scheme under investigation is reported in Fig. 3.2.

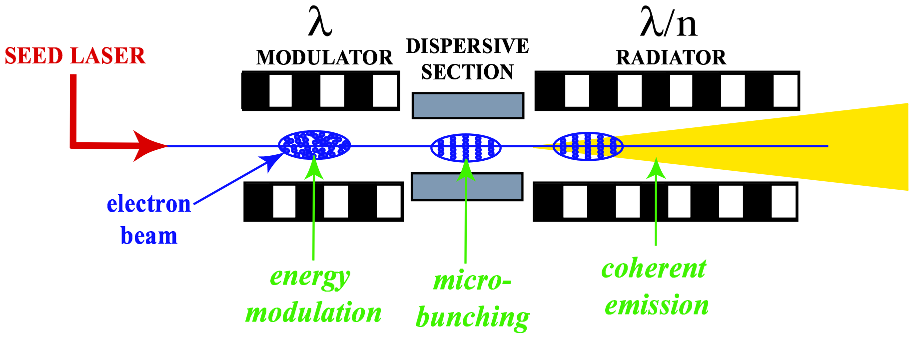

Figure 3.2: *Seeded Harmonic Generation scheme.*

In the first undulator the interaction between the seed laser and the electron beam produces a modulation in the energy distribution of electrons at the wavelength of the external laser. At the beginning (Fig. 3.3a), the electron-beam energy distribution is random in phase with respect to the electromagnetic field provided by the seed laser and characterized by an initial energy spread. During the interaction with the seed, some electrons lose kinetic energy and some others gain energy. As a consequence, the energy distribution is clearly modified, as shown in Fig. 3.3b. The magnetic field of the dispersive section forces electrons with different energies to follow different paths. Therefore, the passage through the dispersive section converts the energy modulation in spatial bunching. Performing a Fourier analysis, the spatial structure of the bunch reveals that there are also components at harmonics of the fundamental wavelength. The corresponding phase space is also shown in the third of Fig. 3.3c. Finally, in the second undulator, that is tuned at one of the harmonics, the electrons produce coherent light because each "micro-bunch" emits radiation as a macro-particle.

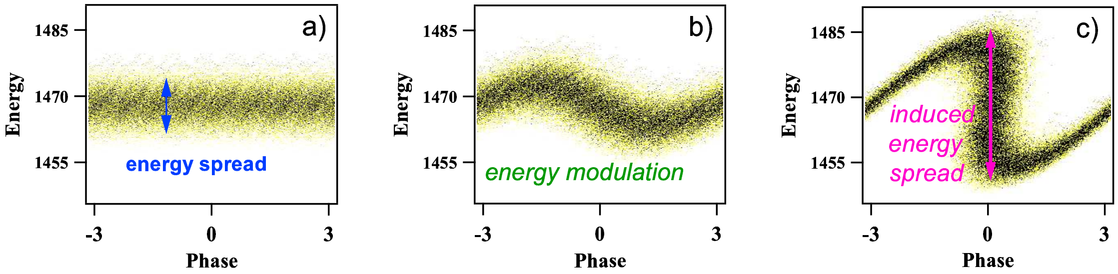

Figure 3.3: *Phase space (γ, θ) evolution. a) initial distribution, b) energy modulation, c) micro-bunching.*

If the electron beam is flat in current and energy, e.g., no quadratic (or higher order) chirp in the two energy distributions, the spectrum of the extracted radiation can be expected to be close to the transform limit. With a single stage of laser-seeded HG (i.e. modulator, dispersive section, radiator) one can achieve about 20 nm (if the beam emittance satisfy the condition on the wavelength $\epsilon \leq \lambda$). To extend the wavelength range (to few nm and less), it is necessary to use at least two HG stages repeated in cascade. In this case, the FEL going out from the first radiator acts as a seed for the second modulator.

As the electron beam has a pulsed structure, the seed pulse has to be not only focused into the first undulator but also synchronized with the electron bunch. The pulse duration at the exit of the radiator is determined by the duration of the seed pulse.

This makes a remarkable difference with respect to SASE. In fact, in the latter case, the duration of the extracted pulse is only determined by the electron bunch length.

3.1.2 One-dimensional analytical model

Now we introduce an analytical model that can be useful to explain the HG process and can be used to predict the output power of a real device.

When the initial energy spread is very small (with respect to the Pierce parameter ρ defined by Eq. 2.23), the dispersive section is able to create a strong microbunching without introducing a significant energy modulation. When the energy spread is comparable or larger than ρ, one has to use a tri-dimensional code to take into account the effects due to the convolution between initial energy spread and induced energy modulation. On the contrary, in the limit of small energy spread, it is possible to use a simple analytical model.

Dispersion section

An ideal dispersion section can be represented as a 3-pole magnet with total length L_d and with the field defined as:

$$B(z) = \begin{cases} B_0, & 0 \leq z < \frac{L_d}{4} \\ -B_0, & \frac{L_d}{4} < z < \frac{3L_d}{4} \\ B_0, & \frac{3L_d}{4} < z < L_d \end{cases} \tag{3.4}$$

The form of the magnetic field is such that at the end of the dispersive section the electrons do not have any transverse or angular displacement with respect to the entrance. This magnetic field induces different paths for particles having different energies. As a consequence, energy separation, $\Delta\gamma$, is transformed in the time separation, Δt [3]:

$$\Delta t = \frac{dt}{d\gamma}\Delta\gamma. \tag{3.5}$$

Here

$$\frac{dt}{d\gamma} = -\frac{e^2}{m^2c^3\gamma^3}\frac{B_0^2L_d^3}{48}. \tag{3.6}$$

The previous relations show the conversion of the energy modulation in bunching. To describe the process one can also make use the electron phase instead of the time. At the end of the first undulator ($z = z_1$) the phase of the jth particle is

$$\theta_j = (k_{s1} + k_{u1})z_1 - \omega_{s1}t_{j1} \tag{3.7}$$

where t_{j1} is the time of arrival at the end of the first undulator, $k_{s1} = 2\pi/\lambda_{s1} = \omega_{s1}/c$ is the wave number relative to the fundamental wavelength in the first undulator and $k_{u1} = 2\pi/\lambda_{u1}$ is the wave number relative to the first undulator (with λ_{u1} the period of the first undulator). At the entrance of the second undulator ($z = z_2$) the phase is

$$\psi_j = (k_{s2} + k_{u2})z_2 - \omega_{s2}t_{j2} \tag{3.8}$$

where $k_{s2} = 2\pi/\lambda_{s2} = \omega_{s2}/c$ is the wave number relative to the fundamental wavelength in the second undulator and $k_{u2} = 2\pi/\lambda_{u2}$ is the wave number relative to the second undulator (with λ_{u2} the period of the second undulator). The arrival time at the entrance of the second undulator is given by

$$t_{j2} = t_{j1} + \frac{dt}{d\gamma}(\gamma_j - \gamma_0) + t_0 \tag{3.9}$$

where t_0 is a constant depending on the position of the second undulator. From the previous relations one can write the the phase-energy relation at the entrance of the second undulator

$$\psi_j = \frac{\omega_{s2}}{\omega_{s1}}\left[\theta_j + \frac{d\theta}{d\gamma}(\gamma_j - \gamma_0) + \theta_0\right] \tag{3.10}$$

The term $\frac{d\theta}{d\gamma} = 2k_u\frac{\Delta\gamma}{\gamma}z$ represents the dispersion section strength and depends on the length and the magnetic field strength. It can be also written as

$$\frac{d\theta}{d\gamma} = \frac{2\pi R_{56}}{\lambda\gamma_0} \tag{3.11}$$

being R_{56} the dispersive section strength. The role of R_{56} will be explained in the next Section.

Limit of small energy spread

We suppose that the electron beam distribution at the entrance the first undulator (modulator) has a uniform distribution in the phase θ (see Eqs. 3.1) and a Gaussian distribution in energy:

$$f_0(\delta\gamma) = \frac{1}{\sqrt{2\pi}\sigma_\gamma} e^{-\delta\gamma^2/2\sigma_\gamma^2}, \tag{3.12}$$

where $\delta\gamma \equiv \gamma - \gamma_0$ and σ_γ is the initial energy spread.

At the end of the modulator, there is an energy modulation $\Delta\gamma \sin\theta$ (where $\Delta\gamma$ is the energy modulation, induced by the seed laser and θ is the electron phase), so that the distribution function at the entrance to the dispersion section is

$$f_0(\delta - \Delta\gamma \sin\theta). \tag{3.13}$$

The passage through the dispersive section, which have a strength $d\theta/d\gamma$, changes the electron phase from θ to $\theta + \delta\gamma(d\theta/d\gamma) + \theta_0$ (see Eq. 3.10) and, as a consequence, the distribution function becomes:

$$f(\gamma, \theta) = f_0 \left[\delta - \Delta\gamma \sin\left(\theta - \frac{d\theta}{d\gamma}\delta - \theta_0 \right) \right]. \tag{3.14}$$

Integrating this distribution over the energy one can found the phase distribution and performing a Fourier analysis of the latter, one gets the bunching parameter:

$$b = 2 \exp\left[-\frac{1}{2} n^2 \sigma_\gamma^2 \left(\frac{d\theta}{d\gamma} \right)^2 \right] J_n \left[n\Delta\gamma \frac{d\theta}{d\gamma} \right], \tag{3.15}$$

where n is the harmonic number, i.e. it defines λ/n the harmonic radiation wavelength, and J_n is the Bessel function of the nth order. The Bessel function represents the micro-bunching and the factor $\Delta\gamma \frac{d\theta}{d\gamma}$ is the phase shift due to energy modulation in the dispersive section. If this factor if much smaller than 1, the micro-bunching scales as its nth power. Hence $d\theta/d\gamma$ must be comparable to $1/\Delta\gamma$. Considering the first exponential factor, when $\sigma_\gamma d\theta/d\gamma \approx \sigma_\gamma/\Delta\gamma > 1$ the energy spread erases the microbunching. Hence the energy modulation $\Delta\gamma$ must be larger than or equal to the energy spread to have large harmonic components: $\Delta\gamma \geq \sigma_\gamma$. The efficiency of the process relies on this relation since the ratio between the energy spread and the induced modulation is crucial for the bunching.

In practice, once the electron beam energy and the energy spread are fixed, the relation 3.15 states that one can choose to optimize the bunching at different harmonics changing the dispersive section strength R_{56}. This is true if one assumes, as in the classical scheme, that inside the modulator only energy modulation is created but no bunching. To have a significant bunching at higher harmonics, the energy modulation $\Delta\gamma$ induced in the modulator should be large, but this in turn would degrade the amplification in the radiator. This explains the need of more the one cascade to reach very short wavelengths.

We concentrate in the following on the process occurring in the radiator, where the electron bunch arrives after the interaction with the seed laser in the modulator and after the passage through the dispersive section.

Limit of zero energy-spread

If the energy spread is much smaller then ρ, one can induce an energy modulation comparable to the energy spread, which is still smaller then ρ. In this specific case the equations can be linearized [3].The solution show two different regimes, i.e. superradiance (when $\rho k_u z \ll 1$) and the exponential growth (when $\rho k_u z \gg 1$). We skip here the derivation, that can be found in [3]. The solution for the vector potential reads:

$$a_s = \begin{cases} 4A_0 \rho k_u z & (\rho k_u z \ll 1) \\ \frac{2}{3} A_0 e^{\sqrt{3}\rho k_u z} & (\rho k_u z \gg 1) \end{cases} \tag{3.16}$$

where

$$A_0 = \frac{2k_u(\rho\gamma_0)^2 \exp\left[-\frac{1}{2}n^2\sigma_\gamma^2\left(\frac{d\theta}{d\gamma}\right)^2\right] J_n\left[n\Delta\gamma\frac{d\theta}{d\gamma}\right]}{k_s a_u [JJ]}. \tag{3.17}$$

When $\rho k_u z \ll 1$ the field grows linearly with z and the harmonic electric field along the undulator is:

$$E = 4\sqrt{2}\frac{mc^2}{e}\, k_s\, k_u\, A_0\, \rho\, z. \tag{3.18}$$

As a consequence, the peak power, defined as

$$P = \frac{\pi}{2} w_0^2 c \epsilon_0 E^2 \tag{3.19}$$

where w_0 is the waist of the FEL laser beam and ϵ_0 is the vacuum permittivity, grows quadratically with z. The quadratic growth of the power can be explained because the electron distribution does not change very much over a short distance (few meters) and the process can be approximated as many rigid micro-bunches that radiate coherently. The distance $\rho k_u z$ is also called gain length. After some gain lengths, the distance between micro-bunches cannot be considered as rigid anymore and the light is amplified exponentially, until saturation is reached.

In the case of the Elettra SRFEL in seeded single-pass configuration, we compared the analytical model with tri-dimensional simulations performed using the GENESIS [7] code. Being the undulator very short (2 m), we are in the limit $\rho k_u z \ll 1$, i.e. quadratic growth, and the radiator is tuned at the third harmonic of the seed laser. Figure 3.4 shows the comparison between the analytical prediction (see Eq. 3.16) and the numerical calculations. Assuming natural energy spread and bunch length, the simulations confirm the analytical prediction, namely the lower the energy, the higher the power. In a physical case (i.e., energy spread and the bunch length corresponding to 6 mA), one observes less harmonic output power since the amplification gain decreases (see Section 2.3.3). Besides one can expect an inversion of the trend predicted by the Yu's model since the energy spread is higher at lower energies (see Section. 1.1.2). Nevertheless, we observe that the power obtained at 0.9 GeV overcomes the one obtained at 1.5 GeV.

The total energy spread $\sigma_{\gamma,tot}$ of the electron beam at the entrance of the radiator is given by the contribution of the initial energy spread combined quadratically with the energy modulation induced by the interaction of the electron beam with the seed:

$$\sigma_{\gamma,tot} = \sqrt{\sigma_\gamma^2 + \frac{(\Delta\gamma)^2}{2}}. \tag{3.20}$$

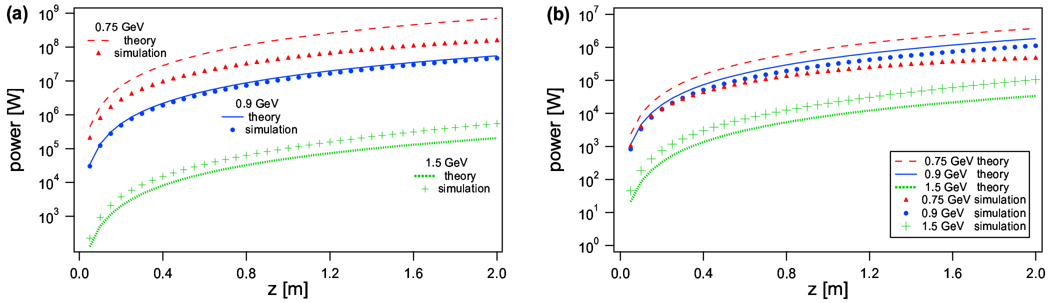

Figure 3.4: *Power vs. radiator length assuming natural energy spread and bunch length (a) and values corresponding to an electron beam current of 6 mA (b). For the parameters used in* GENESIS *simulations see Table 6.1*

To have an efficient coherent harmonic generation, the ratio between the energy modulation induced by the seed laser and the energy spread of the electron beam has to be comparable to the harmonic number [8]. To have an optimum performance

$$\Delta\gamma \geq n\sigma_\gamma. \tag{3.21}$$

This means that if we want to produce the third harmonic, we have to induce an energy spread with the seed laser at least three times larger than the initial energy spread of the electron beam.

3.2 Harmonic generation in oscillator configuration

As already mentioned, the FEL emission is naturally accompanied by harmonic radiation and this is true in all configurations. In the oscillator configuration the fundamental FEL radiation acts as a seed for the harmonic. Besides, while the fundamental power is stored into the optical cavity, the harmonic power is emitted in a single-pass because the mirrors are optimized to reflect only wavelengths in a small interval (few nm) around the fundamental.

The dynamics is more complicated when electrons are recirculated, as in a storage ring. The electron beam keeps memory of previous interaction, that is the energy spread induced by the interaction with the electromagnetic wave piles up turn after turn. Moreover, since the light pulse is shorter then the bunch length, the increase of the energy spread is localized in a portion of the bunch. For the first turns, the synchrotron motion (see Ch. 1) takes away from the heated bunch slice (i.e., the portion that has interacted with the light) the particles with higher energy spread and brings new particles with lower energy spread. This effect is called “phase-space refreshment”. After several interactions, the synchrotron motion mixes all the particles within the bunch and the final result is an increase of the total energy spread. As we will see in detail in Ch. 5, the phase space refreshment is crucial for the harmonic generation process.

In the following sections we concentrate on the process of coherent harmonic generation for a SRFEL in oscillator configuration. In this configuration, the role of the dispersion section is to introduce a phase shift between the radiation (at fundamental wavelength) emitted by the first and the second undulator and, as a consequence, to produce the interference between the two emissions.

3.2.1 Giant pulses

As shown in Eqs. 3.1, harmonic components of the bunching are the source of harmonic radiation. However, since the bunching in an oscillator FEL is not very strong (there is not enough energy modulation) in a single passage, when the FEL is operated in "free-running mode", the harmonic emission is very low and cannot be detected.

As the harmonic power is limited by the energy spread, an experimental technique has been implemented that allows to recover the initial (i.e., "cold") beam condition.

We can imagine to start with a small difference between the light round-trip time in the optical cavity and the inter-bunch period (see Section 2.3. Such a detuning can be experimentally controlled by changing the orbit of electrons.

As shown in Fig. 3.5, in the "free-running mode", the intensity fluctuates in a random way. In the giant pulses regime (see Fig. 3.6), the intensity of each macropulse appears instead more stable and reproducible. Besides, the distance between macropulses is constant since it is externally regulated.

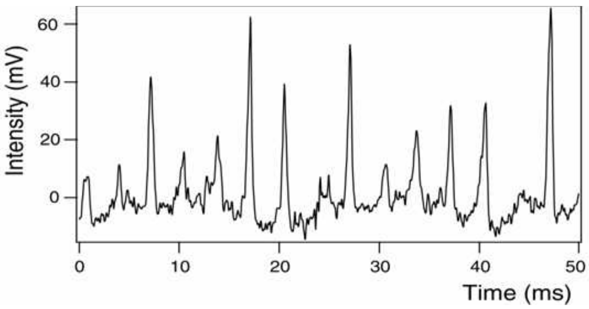

Figure 3.5: *Intensity evolution vs. time of a SRFEL in "free-run".*

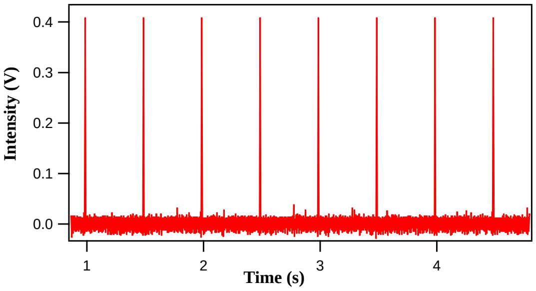

Figure 3.6: *Train of macropulses obtained in the giant pulse regime.*

Several methods have been studied and applied in oscillator FELs [9, 10, 11, 12] to create "giant pulses". There are basically three techniques that have been implemented:

- the gain modulation [13];
- the modulation of RF frequency [11, 12];
- the mechanical gating (chopper) [14].

The first method is presently employed at Duke, where a dedicated magnet steers the electron beam orbit in the transverse direction. When the electron beam orbit is off-axis with respect to the optical cavity, the lasing is stopped and the electron beam can cool down. Once the electron beam orbit returns on-axis, a new giant pulse starts. The modification on the electron orbit can induce small transverse oscillations, but, as the laser waist is much more bigger than the electron beam transverse dimensions, these oscillations have a negligible effect on the actual overlap and therefore on the gain.

The RF frequency modulation has been used in Super-ACO and is currently implemented at Elettra and UVSOR. The revolution period of electrons is periodically modified in order to lose the synchronism with the light in optical cavity. When the light and the electrons are de-synchronized, the electron beam recovers its initial condition and then, when the synchronism is re-established, a macropulse can be generated. It is possible to find an optimum repetition rate of the process that maximizes the average output power: if the period between consecutive pulses is shorter than the synchrotron damping time, the process looses its efficiency. In principle, by quickly restoring the tuning condition, it is possible to prevent the beam heating, but this short transition will induce strong longitudinal oscillations on the electron beam [12] and, as a consequence, affect its temporal overlap with the optical pulse stored in the cavity. If the overlap is perturbed, the net gain at the laser start is reduced and as a consequence the maximum power of the giant pulse. Nevertheless, one can found a compromise for the velocity of the restoring process (slope of the RF jump) that optimizes the intensity and keeps down the oscillations.

The third technique make use of a rotating metallic disc placed into the optical cavity. This disc, called “chopper”, has a small hole where the light can pass through and rotates at constant speed. At regular intervals, the chopper intercepts the light stored in the optical cavity preventing the interaction with the electron beam. Only when light periodically passes through the hole there is interaction and the macropulse can rise up, otherwise the electrons can cool down.

While the first two techniques can be considered equivalent for generating giant pulses (as demonstrated for Duke in [15]), the mechanical gating is still under investigation.

The twofold purpose of the Q-switch technique is to concentrate the average power of a storage-ring FEL in a series of giant-pulses with higher power and to have a regular temporal dynamics of the light. These two features allow to use the FEL light as an investigating tool. It is also possible to synchronize another laser at the FEL emission and to make pump-probe experiments changing the relative delay between the signals. The pump-probe technique can be more easily implemented using the chopper. Indeed the RF frequency can be used for feedback loops in order to control the stability of the FEL intensity.

As in the case of harmonic generation in (seeded) single-pass devices (see section 3.1), the interaction between the electron beam and the stored radiation induces a coherent energy modulation of the beam distribution. The energy modulation, which is proportional to the seed peak power, sums up with the incoherent energy modulation. The dispersive section converts the energy modulation in phase modulation creating the bunching. The electron phase at the exit of the dispersive section depends also to the strength of the magnetic field applied in the dispersive section.

Due to the recirculation of the electron beam, the synchrotron motion transforms after one turn the energy modulation into initial energy spread. This amount increases turn after turn and at a certain point it becomes comparable to the energy modulation induced by the seed. Then the bunching coefficient b_1 reduces to zero, or, equivalently, the net gain (difference between the gain and the losses of the optical cavity) becomes negative. At this stage the seed power collapses and the generation of higher harmonics is stopped.

Bibliography

[1] R. Bonifacio, L. De Salvo and P. Pierini, *Nucl. Instr. and Meth. A* **293** 627 (1990)

[2] R. Bonifacio, L. De Salvo Souza and P. Pierini, *Nucl. Instr. and Meth. A* **296** 787 (1990)

[3] L. H. Yu, *Phys. Rev. A* **44**, 5178 (1991)

[4] I. Boscolo and V. Stagno, *Nucl. Instrum. Methods Phys. Res.* **198**, 483 (1982)

[5] R. Coisson and F. De Martini, Physics of Quantum Electronics **9**, 939 Addison-Wesley, Reading, MA, 1982;

[6] I. Schnitzer and A. Gover, *Nucl. Instr. and Meth. A* **237**, 124 (1984)

[7] http://pbpl.physics.ucla.edu/ reiche/

[8] L. H. Yu and I. Ben-Zvi, *Nucl. Instrum. Methods Phys. Res. A* **393**, 96 (1997)

[9] G. N. Kulipanov, *et al.*, *Nucl. Instr. and Meth. A* **296** 1 (1990)

[10] V. N. Litvinenko, *et al.*, *Nucl. Instr. and Meth. A* **429** 151 (1999)

[11] T. Hara, *et al.*, *Nucl. Instr. and Meth. A* **431** 21 (1994)

[12] G. De Ninno, *et al.*, *Nucl. Instr. and Meth. A* **528** 278 (2004)

[13] I. V. Pinayev, *et al.*, *Nucl. Instr. and Meth. A* **475** 222 (2001)

[14] F. Curbis, *et al.*, *Proceeding of FEL 2006, Berlin, Germany* http://cern.ch/AccelConf/f06/PAPERS/TUPPH021.PDF

[15] G. De Ninno, *et al.*, Elettra Internal Note

Other related papers:

[16] R. Prazeres, *et al.*, *Nucl. Instrum. Methods Phys. Res. A* **304**, 72 (1991)

[17] A. Doyuran, *et al.*, *Phys. Rev. Lett.* **86**, 5902 (2001)

[18] V. N. Litvinenko, *Nucl. Instr. and Meth. A* **507** 265 (2003)

[19] Bessy CDR

Chapter 4

Experimental setup for CHG

In this chapter we present the experimental setup for CHG. Both oscillator and single-pass configurations rely on the same the same experimental setup, i.e. the optical klystron installed on the Elettra storage ring. We will describe firstly the common parts of these two configurations and then we will focus on the peculiarities of each configuration.

4.1 Linear accelerator and transfer-line

A linear accelerator (LINAC) generates the electrons that are then injected in the ring. The overall length of the linac is 66 m and it is composed of the gun, a low energy section and seven high-energy sections each 6 m long. The gun houses a thermionic cathode that is heated to very high temperature and emits electrons. These electrons are extracted by an electric field of up to 100 kV and then accelerated through various radio-frequency structures, up to a final energy which can be as high as 1.2 GeV. The beam is focused between accelerating sections by quadrupole magnets. The electrons must propagate in vacuum through all the components, from the source to the storage ring, and in the ring itself the vaccum must be very high to have a good lifetime. After the linac, the electrons pass through the transfer-line (a series of deflection and focusing magnets) to reach the storage ring. Both the linac and transfer line are below ground so as not to interfere with beamlines in the experimental hall. The storage ring is filled by a multi-turn injection process whereby pulses of electrons are gradually fed into the ring ten times a second until the desired current is achieved. Filling the ring to high currents takes several minutes. A schematic layout of the accelerators chain in shown in Fig. 4.1.

4.2 Elettra storage ring

The Elettra storage ring is a machine dedicated to the production of synchrotron radiation and it is therefore usually operated in multibunch mode at an electron beam energy of 2–2.4 GeV to optimize the beam lifetime (against the Touschek effect), photon flux and spectrum. As most of today's synchrotron sources, the storage-ring lattice (i.e. the arrangement and strengths of dipoles, quadrupoles and sextupoles magnets) is based on the Chasman and Green design, also called double-bend achromat, that ensures low emittance and hence high brightness.

Three families of quadrupoles are used to strongly focus the electron beam in the trans-

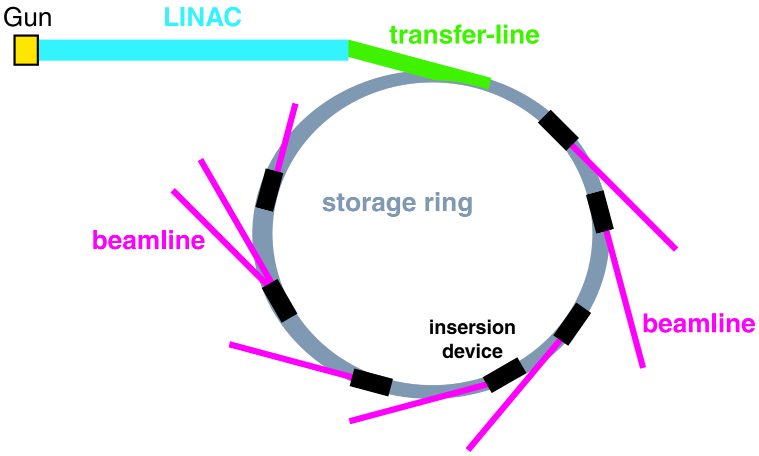

Figure 4.1: *Linac, transfer-line and storage ring.*

verse plane. This allows to obtain a small transverse size and divergence of the electron beam and hence a small emittance that is request for high brightness of the photon beam. Sextupoles are used both to suppress chromatic effects (arising because particles with different energies follow different trajectories) and to compensate nonlinearities introduced by other magnets.

Four (single cell) RF cavities supply to electrons the energy lost by synchrotron radiation. The cavities operate at 500 MHz. The summed voltage of the cavities determines the longitudinal energy acceptance of the machine.

In one of the 12 straight sections is accommodated an optical klystron that can act either as a standard synchrotron light source for the Nanospectroscopy beamline or as the interaction region for the FEL. The optical klystron was designed both to be compatible with the normal operations of the beamline at high electron energy and to provide light in the visible–VUV range for FEL operations at low electron energy.

There are several reasons that prevent the SRFEL operations during the normal users shifts. The optical cavity has a round trip of 216 ns that corresponds to the interbunch period if 4 bunches are stored (equally spaced). In the standard operation all (most) of 432 buckets are used to accumulate electrons and 300-400 mA are usually stored for several hours. Hence the multibunch filling corresponds to less than 1 mA per bunch. At present, the maximum current that can be stored in 4 bunches is about 24 mA but sometimes from 10 mA strong coupled bunch modes (CBMs) instabilities take place. Over this threshold the CBMs can be reduced changing the temperature settings of the four RF cavities. During the FEL operations the energy is below 1.5 GeV (typical energies are 0.75 GeV, 0.9 GeV, 1.1 GeV) and the filling is single bunch or 4 bunches, spaced by 216 ns. Using the resonance condition and considering the maximum magnetic strength produced by the undulator, one can see that using 2 GeV for the beam energy, the actual undulator resonates around 160 nm. Moreover there are technical reasons for which electron energy greater than 1.5 GeV could be dangerous for the safety of the beamline and also radiation problems connected to the maximum current achievable. Table 4.2 resumes the main Elettra parameters in FEL operation mode.

Electron beam energy	0.75–1.5 GeV
Ring circumference	259.2 m
Orbit period	864 ns
Orbit frequency	1.157 MHz
RF frequency	499.654 MHz
Harmonic number	432
Momentum compaction factor	0.00161
β_x at ID center	8.2
β_y at ID center	2.6
Normalized x-emittance (1 GeV)	3.2 mm mrad
Normalized y-emittance (1 GeV)	0.2 mm mrad
Number of bunches	1–4
Max current per bunch	6 mA
Energy spread at 6 mA (0.9 GeV)	0.20% - 0.12%
Bunch length at 6 mA (0.9 GeV)	25–30 ps
Peak current at 6 mA (0.9 GeV)	~ 80 A
ϵ_x (0.9 GeV)	$\sim 1.4\,\mathrm{mm}\mu$ rad
ϵ_y (0.9 GeV)	$\sim 0.14\,\mathrm{mm}\mu$ rad
σ_x (0.9 GeV)	$1.1 \cdot 10^{-4}$ m
σ_y (0.9 GeV)	2.6×10^{-5} m

Table 4.1: *Elettra parameters for SRFEL operations.*

4.2.1 The optical klystron

The experimental setup for CHG at Elettra is based on the optical klystron installed on the storage ring. This device has been built and used for a long time only for the SRFEL in oscillator configuration (see Fig. 4.2).

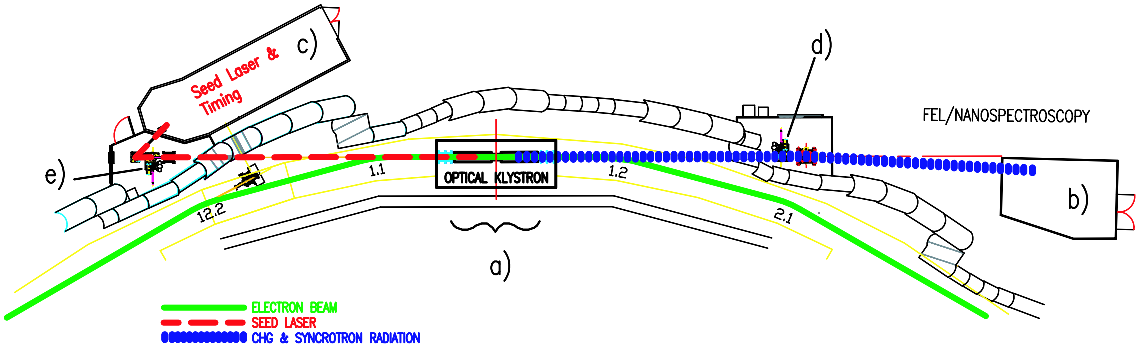

Figure 4.2: *Layout of the Elettra section 1 where is installed the optical klystron for the FEL beamline.*

The general layout of the Elettra FEL beamline is shown in Fig. 4.2. Two APPLE-II type permanent magnet undulators together with a three-pole electro-magnet constitute the modulator (ID1), the radiator (ID2) and the dispersive section (DS) of the optical klystron (OK). Both the gap and the phase of the APPLE-II undulators can be tuned independently. Each undulator can be tuned at different wavelengths and the polarization can be varied continuously from linear to elliptical. The dispersive section is a three-pole electro-magnet which allows to vary continuously the R_{56} parameter from 0 μm to 70 μm. Table 4.2.1 summarizes the main parameters of the optical klystron.

Undulators: ID1 and ID2	
Type	APPLE II permanent magnet
Period	100 mm
Number of periods	20
Minimum gap	19 mm
λ 1^{st}harm. (gap=19 mm,phase=0)	756 nm at 0.9 GeV 272 nm at 1.5 GeV 153 nm at 2.0 GeV
Dispersive section: DS	
Type	electromagnetic 3-pole
Length	50 cm
Maximum field	0.8 T

Table 4.2: *Optical klystron parameters.*

4.3 Setup for FEL operation

4.3.1 Oscillator configuration

In order to operate the FEL in oscillator mode, a couple of high reflectivity mirrors have to surround the photon source. By choosing correctly the mirror curvature radii the light emitted by the undulators is stored in the optical cavity and by placing them at the right distance the optical pulses are synchronous to the electron bunches circulating into the ring.

The SRFEL beamline is equipped with two UHV mirror chambers (see Fig. 4.2) used for the precise alignment of the optical cavity, which is 32.4 m long. Up to three mirrors can be mounted by means of a load lock UHV transfer chamber. Position and angle of the mirrors can be adjusted by means of in-vacuum stepper motors with a resolution of 0.5 μm for the three spatial coordinates and of 11 μrad for pitch and yaw angles. Piezoelectric (pitch and yaw) actuators with a resolution of 11 n rad for pitch and yaw angles allow a finer tuning of the optical cavity. A more detailed description of the SRFEL beamline is given in [1, 2, 3].

Optical Cavity

The optical resonator is the responsible of transverse intensity profile of the FEL beam that normally can be expressed by the fundamental Gaussian TEM00 mode:

$$I(x, y, z) = I_0 \frac{w_0^2}{w^2(z)} \exp\left[-\frac{2(x^2+y^2)}{w^2(z)}\right] \tag{4.1}$$

where $w^2(z) = w_0^2\left(1+\frac{z^2}{\zeta_0^2}\right)$, $\zeta_0 = \frac{\pi w_0^2}{\lambda}$ is the Rayleigh range and w_0 is the "waist" of the Gaussian beam defined by:

$$w_0 = \sqrt{\frac{\lambda\sqrt{(2R_c-\mathcal{L})\mathcal{L}}}{2\pi}} \tag{4.2}$$

where R_c is the bend radius of the mirrors and $\mathcal{L}$ is the length of the optical cavity.

The radii of curvature have to be chosen in abidance of the stability criteria [4] and in order to maximize the coupling between electrons and the photons stored in the cavity. The stability is guaranteed if the following condition is respected:

$$0 < g_c^2 < 1 \tag{4.3}$$

where g_c is defined as $1 - \mathcal{L}/R_c$.

The Filling factor parameter aims to describe the photon-electron coupling in the interaction region:

$$F_f = \frac{1}{\sqrt{\left[1+\left(\frac{w_0}{2\sigma_x}\right)^2\right]\left[1+\left(\frac{w_0}{2\sigma_z}\right)^2\right]}} \tag{4.4}$$

where σ_x and σ_z are the transverse dimensions of the electron beam.

4.3.2 Single pass configuration

Let's now concentrate on the experimental setup for externally seeded CHG. The three main blocks are the optical klystron, the seed laser and the front-end station used both for the detection/diagnostics of the CHG pulse and to focus the harmonic light into an experiment end-station. Although on a reduced scale, the scheme is fully equivalent to that for seeded single-pass FELs [5]. In the following Sections, we provide details about both the temporal and transverse alignment of the laser pulse and of the electron beam.

Optical klystron

As already mentioned, gap and phase of the undulators are independently tunable: for a given electron beam energy this allows to select the first harmonic's wavelength of the spontaneous emission of ID1 and ID2, that correspond, respectively, to the seed laser wavelength and to the harmonic that we want to amplify. Since the polarization of the seed laser is linear and horizontal, in order to maximize the coupling between the electromagnetic field and the electron bunch inside the modulator, we usually set the phase of ID1 at zero, corresponding to linear s polarization state. The phase of ID2 can be chosen either for linear or circular polarization depending on the experimental requirements about the polarization of the coherent emission. Finally, the DS strength is varied in order to optimize the micro-bunching of the electron beam. It is worth underlining that the radiator is not long enough to reach saturation in the CHG process. Nevertheless, as it will be shown in Ch. 6, the obtained out power makes this device an attracting light source for some experiments. To maximize the electron current per bunch, the machine is operated in single bunch mode: this prevents the excitation of longitudinal mode instabilities. In this configuration one can store up to 6 mA in a stable single bunch, which corresponds to a peak current of about 80 A for an electron bunch about 30 ps long. Moreover, since the modulator has to be tuned at the wavelength of the seed laser ($\lambda \geq$260 nm, see next paragraph), due to the limitation on the minimum undulator gap, typical values for a suitable beam energy are in the range 0.75–1.5 GeV. One of the great advantages of the single pass scheme is that it does not rely on the use of optical elements that limit the accessible spectral range. Nevertheless, we make use of the front mirror chamber (D in Fig. 4.2) to mount a broad band holed mirror that we use for aligning of the seed laser with the electron beam. At the same time, the reflection positions of both the synchrotron radiation and the seed laser allows to monitor the transverse alignment (see paragraph 4.3.2). Since the mirror is placed 12.5 m downstream the radiator, an aperture of 1 mm has an angular acceptance of 80 μrad.

Seed laser system

The seed laser is a multi-stage system including an IR oscillator developed from the laser group in Elettra and a Legend amplifier assembled by Coherent [6]. The oscillator is a passive mode locked Ti:Sapphire cavity pumped by a 4.5 mW diode laser. The mode locking, based on the optical Kerr effect [7], allows entering in a pulsed regime that is adapted to the total cavity length. Such a length has been chosen in order that the repetition rate of the laser is commensurate with the repetition rate of the synchrotron. As it will be shown in Section 4.3.2, this allows the synchronization. Note that the selected frequency is in the hundred MHz range, where the system is less sensitive to acoustic perturbation. When optimized, the oscillator delivers 120 fs (FWHM) pulses with 3 nJ energy per pulse at the fundamental wavelength in the range 780–800 nm. The oscillator emission seeds the Legend amplifier, which increase the energy of a single pulse up to 2.5 mJ at the fundamental wavelength. The pulse duration can be changed by means of two compressors, a flipper allows to switch. In particular, two different schemes can be chosen in order to obtain either 100 fs or 1 ps "transform limited" pulses. The operational repetition rate range is between 1 Hz to 1 kHz. In Fig. 4.3 is reported the autocorrelation trace obtained for the fundamental wavelength at a repetition rate of 50 Hz. Considering the calibration factor of the autocorrelator equal to 500 fs/ms, under the hypothesis of Gaussian profile the resulting pulse duration is:

$$\Delta t = \frac{0.282 \times 500}{1.41} = 100\, fs \quad \text{[FWHM]}. \tag{4.5}$$

The amplifier is equipped with second and third harmonic generation stages, leading to the production of ultra-short pulses at 390–400 nm for the second harmonic and 260–267 nm for the third one, with conversion efficiencies high enough to obtain a suitable peak power for the seeding of the electron bunch. The main advantage of seeding with shorter wavelength is the possibility of generating coherent radiation into the VUV range, where a number of electronic transitions can be accessed and their dynamical character can be investigated exploiting the peculiar temporal properties of the CHG radiation. At the same time, in relation with the limit imposed by the minimum gap value of the modulator, as the seeding wavelength is shortened, it is possible to increase the electron beam energy, taking so advantage of a more stable and durable (longer lifetime) electron beam.

In Fig. 4.4 it is shown the laser system that is located in a temperature controlled hutch to prevent as much as possible any thermal drift of the optical alignment. This hutch

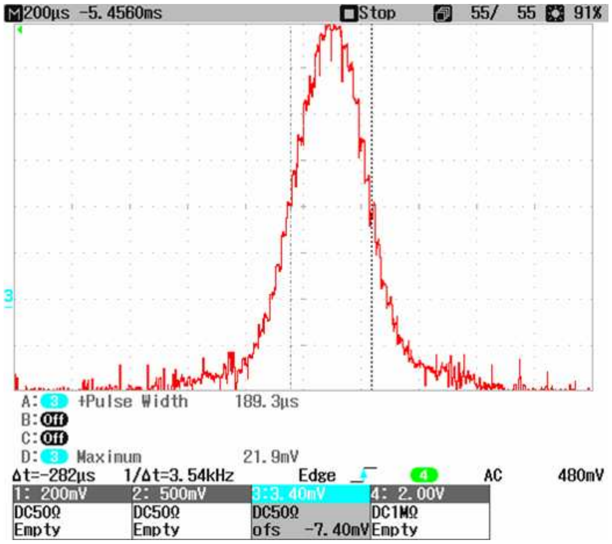

```
M200µs -5.4560ms          Stop     55/  55  91%
A: 3  +Pulse Width      189.3µs
B: Off
C: Off
D: 3  Maximum            21.9mV
Δt=-282µs   1/Δt=3.54kHz        Edge   4    AC      480mV
1: 200mV     2: 500mV     3:3.40mV     4: 2.00V
DC50Ω        DC50Ω        DC50Ω        DC1MΩ
Empty        Empty        ofs   -7.40mV Empty
```

Figure 4.3: *Autocorrelation trace of the pulse produced from the amplifier at the* 1^{st} *harmonic. The calibration coefficient is 500 fs/ms.*

is used as FEL back-end station when the FEL is operated in oscillator configuration. The same optical path is used to focus the seed laser onto the electron bunches passing through the modulator.

In order to optimize the energy transfer from the laser to the electron bunch, the laser must be precisely aligned and synchronized to the electron beamand special diagnostics must be developed.

Alignment

Transversal alignment is complicated by the fact that the electron beam is recirculated in the storage ring. Indeed, this does not allow the use of (destructive) fluorescent screens to steer the position of the laser and optimize the transverse alignment with the electron beam. For this purpose, we used instead the back reflection from a holed mirror placed downstream the optical klystron. In order to align the hole on the axis of the modulator, we measured the spectra of the spontaneous emission as a function of the mirror transverse position by means of a spectrometer located in the front-end hutch. It is well known in fact (see Eq. 1.38) that the spectra shifts in the direction of higher wavelengths as the off-axis angle increases.

The mirror is aluminum coated and reflects back with good efficiency the radiation that is not transmitted through the hole, at least in the spectral range useful for the modulator operations (i.e. from 800 to 260 nm). We adjust then the angles of the holed mirror in order to project the reflection onto a monitor located at the back-end exit. This projection together with the hole of the mirror defines a reference line that we can use to align the seed laser with the electron beam. The laser, entering the straight section trough the back-end viewport (see Fig. 4.4), is aligned on the hole maximizing the power transmitted at the front-end exit. The procedure is repeated adjusting the entering point as far as the reflection of the laser is superposed to the reflection of the spontaneous emission (see Fig. 4.5).

In order to ensure of the stability of the transverse alignment, we checked the pointing

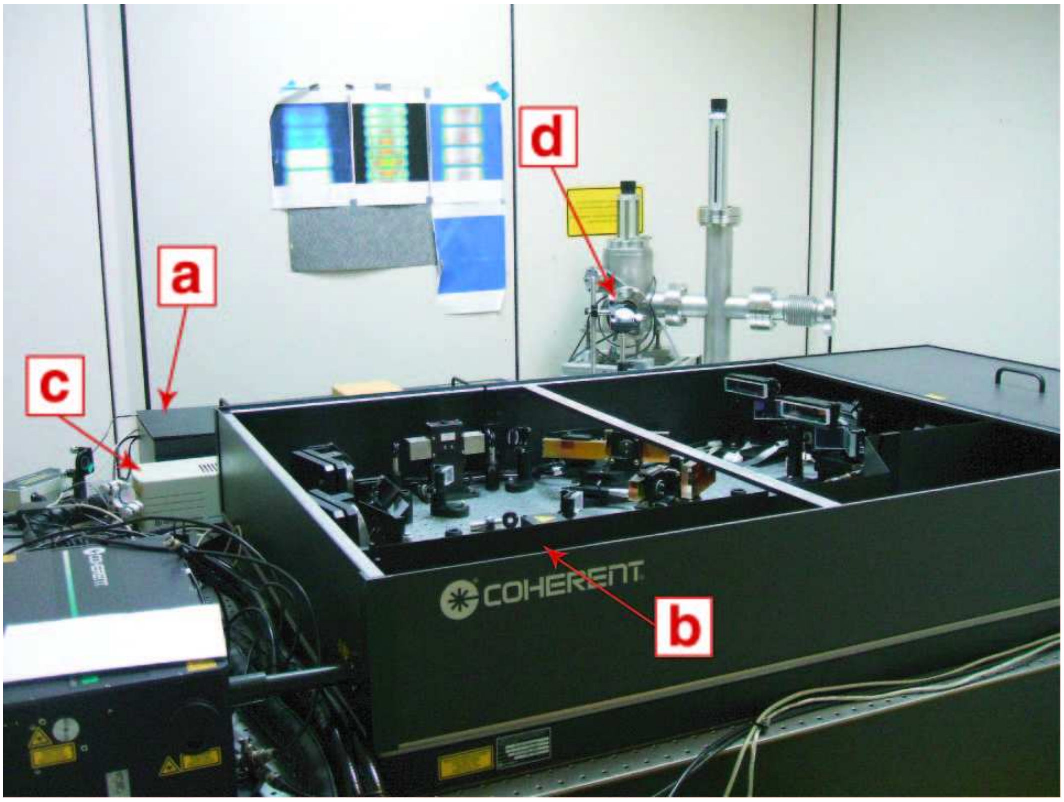

Figure 4.4: *The seed laser system. a) Ti:Sapphire oscillator b) Ti:Sapphire amplifier c) diode laser d) SRFEL back-end viewport.*

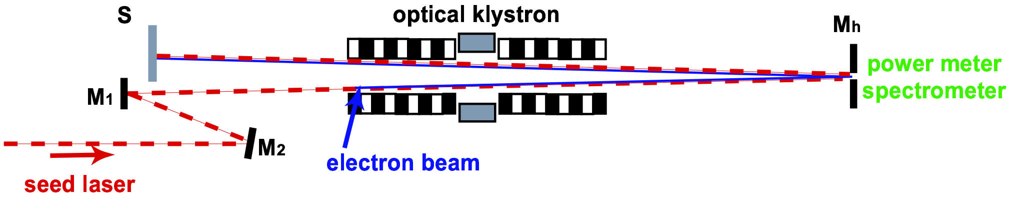

Figure 4.5: *Schematic layout of the alignment procedure. M_h: holed mirror M_1,M_2: laser mirrors S: monitor*

stability of the laser beam. The results are well compatible with the geometry of the experiment. The waist of the laser is placed at the center of the modulator located about 20 m upstream the last seed mirror. The pointing stability is better than $1.4\times\ 4.4\mu\text{rad}^2$ (horiz x vert), which corresponds to a spatial fluctuation at the interaction region lower than $0.03\times\ 0.09\,\text{mm}^2$. Since the dimension of the laser beam at this distance is nearly $1\,\text{mm}^2$, the laser can ensure an excellent stability of the transverse alignment.

Timing

After transverse alignment the laser must be synchronized to the storage ring radio-frequency (RF = 499.654 MHz) and opportunely delayed so that the seed can overlap and interact with the electron beam inside the modulator. To do so, we lock the laser oscillator to a sub multiple of the RF trough a phase locked loop (PLL). In fact, the length of the cavity has been chosen to determine a mode locking frequency of 83.3 MHz $\simeq$ RF/6 and is continuously adjusted by the PLL, in order to maintain the synchronization with the RF reference signal. Moreover, this is also valid for a single bunch (SB) after a whole revolution inside the storage ring: in fact the harmonic number of Elettra (i.e. the number of RF cycles in an orbit period) is 432 that can be divided by 6.
The train of pulses coming from the oscillator enters the regenerative amplifier. The output of this latter is naturally synchronized with the oscillator but the maximum repetition rate is 1 kHz. Therefore we need to provide a trigger to the Pockels cells of the amplifier with this frequency where the exact period is a multiple of the SB orbit period. A scheme of the synchronization setup is shown in Fig. 4.6).

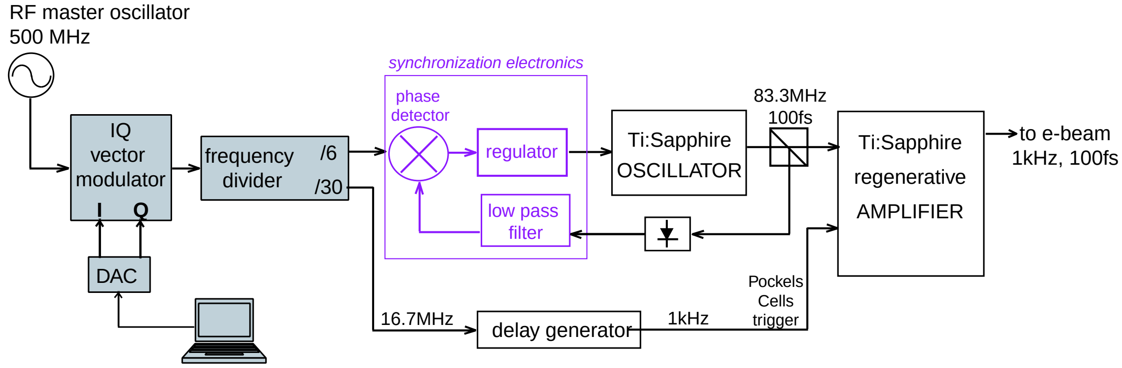

Figure 4.6: *Scheme of the synchronization setup.*

The RF frequency is distributed in the Elettra experimental hall on coaxial cable and is part of the SR user timing system (SR-UTS), available for time resolved experiments. The RF signal is divided by 6 by means of a low noise, 8 channels, clock distribution board AD9510to form the reference signal of the PLL. The PLL is realized by means of a Time-Bandwidth CLX-1100 unit [8], which compares the reference signal (f_1 = RF/6 $\simeq$ 83.3 MHz) to the oscillator time structure, obtained filtering the output of an in-cavity photodiode signal. The CLX-1100 measures their relative phase and responds with an action on the cavity length moving a mirror mounted on piezoelectric stage. Doing so, the phase difference is kept constant and the average phase noise can be in principles of few hundreds fs, depending on the quality of the electrical signals, on the

environmental condition (e.g., acoustic noise) and on the laser stability.
To produce the trigger for the amplifier we gate at f_{amp}=0.997 Hz a second output of the AD9510, f_2=RF/30$\simeq$16.7 MHz, by means of an Highland Tech. P400 delay generator. More precisely, the relationships between the frequencies of the different signals are as follows:
the SB revolution frequency is f_{SB} = RF/432 = 1.157 MHz
f_1 = RF/6 = 72×f_{SB}
f_{amp} = f_2/16704 = RF/(30×16704) = RF/(501120) = RF/(432×1160) = f_{SB}/1160.
Finally, the amplifier output is delivered every 1160 SB turns. This implies some issues that have to be considered in order to separate the CHG from the synchrotron radiation background that, when integrated over the laser period, can be as intense as the CHG contribution (or even more) and must be filtered out. For single shot acquisition, the CHG contribution is typically orders of magnitude more intense if compared to the spontaneous emission, which can be neglected. To trigger the single shot acquisition we use the low jitter (∼20 ps) pre-trigger supplied by the amplifier. On the contrary, for integrated measurements we must either subtract the background or develop a gating system for the detection.

To evaluate and adjust the synchronization between seed and electrons we proceed as follows: once aligned in space, the two optical beams are collinear and share the same optical path. It is therefore possible to collect both on a fast photodiode and measure the delay with a broadband sampling oscilloscope. This approach is straightforward and permits to define a temporal overlap with an uncertainty better than 20-30 ps which is very close to the electron bunch duration. The main limitation to this procedure is set by the great difference in amplitude of the two pulses (about 10 orders of magnitude); such as difference cannot be overcome using optical filters. As a result, during this procedure the seed power must be strongly reduced, to protect the photodiode and to have a signal comparable with the spontaneous emission. In this condition the seed is not enough efficient to trigger the CHG mechanism. After synchronization the photodiode is removed and the seed power is increased at a suitable value. A fine optimization of the transversal and longitudinal alignment is made maximizing the CHG signal. This means that during harmonic generation we cannot monitor directly the stability of the synchronization. Nevertheless, this procedure is useful to calibrate an indirect indicator for the longitudinal alignment: the SR user timing system includes the distribution in the experimental hall of the signal of the "pick-up" electrode. The latter is obtained by amplification of the signal from an inductive electrode placed in the SR vacuum chamber. For SB filling this produces a sharp spike (∼200 ps of rise-time) that indicates the relative position of the bunch inside the ring circumference. The delay that we measure between the seed pre-trigger and this signal when the CHG is optimized depends only on the laser optical path and on the coaxial line length that can slightly change in time due to thermal drift. The delay is reproducible and can be continuously monitored also during CHG.
In order to adjust the phase shift between the seed laser and the electron beam and obtain a suitable longitudinal alignment, we make use of a digital IQ vector modulator based board. This low noise device introduces an arbitrary phase shift on the RF reference signal controlled via PC using a DAC board. If the phase shift is small enough, the corresponding delay is propagated throughout the electronics (AD9510 divider and PLL) to the oscillator pulses without losing the locking condition. Empirically, we observed that it is possible to shift the pulses train with respect to the electrons at a speed of the order

of 100 ns/s maintaining the locking condition. The amplitude and phase noise of the RF signal from the SR-UTS has been measured with an Agilent Source Signal Analyzer. The integrated absolute jitter is about 1.5 ps that, considering a typical electron bunch length of 30 ps, it is appropriate for our purpose. The final jitter on the pulses train of the oscillator is about 2.5 ps in the 10 Hz—10 MHz offset frequency range. It results to be mostly due to RF jitter and oscillator instability. In fact, we have estimated the contribution to the total jitter of the IQ modulator and the AD9510 divider to be about 50 fs and 250 fs respectively. If used with state of the art low jitter reference signal (few tens of fs) and femtosecond fiber oscillators, this setup can be applied when timing stability requirements are more sever, as is the case for the seeding of 4^{th} generation CHG sources.

4.3.3 Diagnostics

Monochromator

The light emerging from the front-end exit is transmitted inside the front-end hutch passing through a CaF2 view-port that separates the SR UHV area from the atmosphere. Here the light is detected and characterized by means of a 750 mm, Czerny-Turner design spectrometer. This instrument mounts two UV-blazed gratings, one for medium dispersion (i.e., 600 l/mm) and the other for high dispersion (3600 l/mm). After dispersion, the light can be focused either onto a liquid nitrogen cooled charge-coupled device (CCD) detector or, by means of a side mirror, on the exit slits after which is mounted a photomultiplier tube (PMT).

- The CCD can record in a single acquisition a whole spectrum whose width depends on the grating in use. It is suitable for very weak intensity but the minimum integration time is about 25 ms, i.e. much longer that the laser period. For this reason, in order to extract the contribution of the harmonic emission only, we need to acquire and subtract the spontaneous emission background.

- The PMT is a single channel detector but has good detection efficiency and fast response (rise time ∼1 ns). It is used for single shot measurements in a given bandwidth that depends on the grating dispersion and on the width of the exits slits.

The light can also be transported outside the hutch to be focused into an experimental end-station. We can insert in the optical path different sets of interferential mirrors that allow separating and recombining harmonics and seed. This permits to optically delay one signal with respect to the other to perform pump and probe experiments.

The optical path, from the CaF2 window to the end-station and trough the spectrometer can be purged with N2 flow in order to reduce the atmosphere's absorption in the UV range.

The SRFEL beamline shares with the Nanospectroscopy beamline the optical klystron in the Elettra straight section 1. The transport of the harmonic pulses produced in the FEL branch is accomplished by means of a switching mirror. The Nanospectroscopy beamline is equipped with SPELEEM microscope and it has been used to conduct a proof–of–principle experiment. The experimental results will be shown in Ch. 7.

Streak camera

A streak camera is a powerful instrument to measure very short optical pulses in a wide spectral range. A pico-second resolution double sweep streak camera (DSSC) [9] is used in our laboratory to measure and characterize the electron beam and FEL properties. By measuring the visible part of the optical pulse generated by electrons passing though a bending magnet (synchrotron radiation) it is possible to infer to the bunch length and also the electron beam stability with respect to the ring RF frequency.

The DSSC working principle is shown in Fig. 4.7 and it relies to a time-to-space conversion of fast optical pulses. The focused incoming photons are converted into electrons by a photo cathode. The emitted electrons are accelerated and deflected by a high voltage applied to the deflection electrodes (see Fig. 4.7). A charge-coupled device (CCD) camera acquires the final image generated by those electron streaked out on a phosphor screen, placed at the instrument end.

By combining the synchrotron radiation and the FEL pulses, the DSSC acquisition is able to provide information on the coupled electron-laser dynamics (see for example Fig. 5.4).

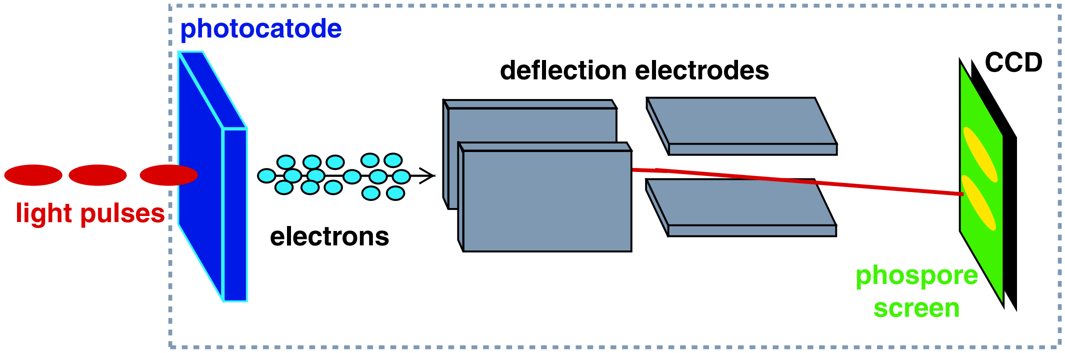

Figure 4.7: *Working principle of a double sweep streak camera. The light pulses are converted by the photocatode into electrons that pass through two orthogonal pairs of deflection electrodes. The sweepped electrons are then collected by a phospore screen and a linear detector, such as a CCD array is used to measure the pattern on the screen and thus the temporal profile of the light pulse.*

Bibliography

[1] R. P. Walker,*et al.*, *Nucl. Instr. and Meth. A* **429** (1999) 179

[2] R.P. Walker, *et al.*, *Nucl. Instr. and Meth. A* **475** (2001) 20

[3] M.W. Poole, *et al.*, *Nucl. Instr. and Meth. A* **445** (2000) 448

[4] O. Svelto, "Principi dei Laser", Tamburini, Milano 1972.

[5] Technical Note of Sincrotrone Trieste for Fermi project no. ST/F-TN-07/12

[6] www.coherent.com

[7] K. Sala and M. C. Richardson, *Phys. Rev. A* **12**, 1036–1047 (1975)

[8] www.tbwp.com, sub-ps laser timing stabilization

[9] M. Ferianis, "The Elettra Streak Camera: system set-up and first results", *Proc. of the DIPAC 1999 Conf., Chester, UK*

Chapter 5

Generation of Coherent Harmonics in Oscillator configuration

This chapter concentrates on the possibility of producing light pulses at harmonic wavelengths of the coherent field amplified in an oscillator FEL. The process relies on the bunching produced by the laser-electron interaction within the undulator and on the emission at specific harmonics of the resonant wavelength. Actually, the tunability range of this kind of devices in standard operation mode is limited by lack of mirrors with the required characteristics below 170 nm. The coherent harmonic generation is challenging in oscillator FELs implemented on storage rings, that usually have the fundamental emission in the VUV range. Peculiar of oscillator SRFELs is the re-circulation of electrons. The repeated interaction with the stored FEL radiation affects the beam properties. Indeed, Q-switch regimes have been implemented in SRFELs in order to increase the peak power of the radiation and hence the bunching which is necessary for the harmonic generation.

This chapter is organized as follow: We first present the experimental setup and the methods for the generation of coherent harmonic radiation in oscillator configuration. Then, we review the obtained experimental results for giant-pulse regime and harmonic generation. We also mention some open points regarding the fine temporal shape of fundamental and harmonic pulses that require numerical simulation in order to be deeply investigated. A section is then dedicated to present numerical simulations: the investigation is based on a modification of an existing FEL code. Obtained results are in agreement with experiments. Simulations also allow to study the inner structure of the FEL pulses.

5.1 Layout

The experiments have been performed on the Elettra storage ring, already presented in Ch. 4. The SRFEL has been operated in oscillator configuration. This implies the use of two cavity mirrors. Both undulators are tuned at the same resonant wavelength. The out-coupling laser mirror has high reflectivity at the fundamental wavelength and, at the same time, high transmission at the desired harmonic wavelength. Extraction can be achieved either by using a dichroic mirror, characterized by different optical properties at different wavelengths, and by using a holed mirror. Both solutions have been studied during the experiments. A first set of measurements has been done using mirrors with high reflectivity (HR) at 660 nm and high transmission (HT) at 220 nm. An alternative configuration made use of mirrors with HR at 450 nm and a small hole in the center of the front one (where the harmonic is extracted). The size of the hole is such that it allows the extraction of enough harmonic power without causing too large loss on the fundamental field; assuming a fundamental Gaussian modes for both the fundamental and the harmonic radiations, the required size of the hole is 0.7 mm of diameter.

Figure 5.1 shows the schematic layout of the Elettra SRFEL in oscillator configuration.

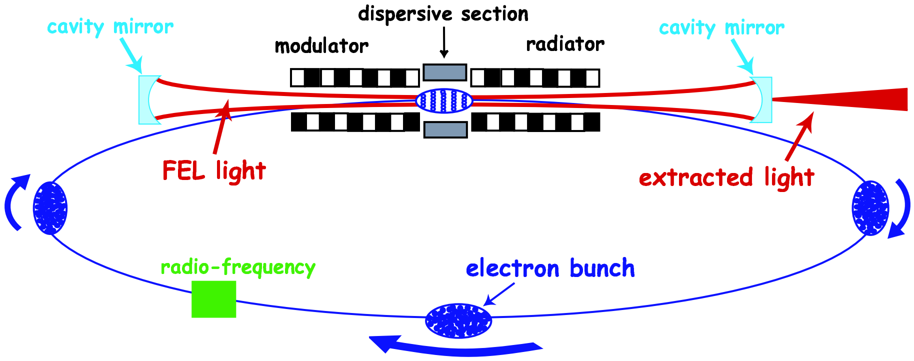

Figure 5.1: *Sketch of the Elettra SRFEL in oscillator configuration. Harmonic radiation of the resonant FEL field can be extracted by means of special out-coupling mirrors (for a more detailed description of the setup see Ch. 4)*

As already mentioned, when the FEL oscillator is operated in free-running mode the micro-pulse power is usually not sufficient to act as a seed for CHG. A much larger amount of peak power can be produced when the FEL works in the so-called giant-pulse regime. In fact, it has been demonstrated [1] that the giant-pulse regime is the only way to produce enough intra-cavity power to initiate the coherent harmonic generation in SRFELs.

5.2 Giant pulses in SRFEL

As explained in Ch. 2, the laser dynamics on a millisecond temporal scale depends on the temporal overlap between the electron bunch and the laser pulse in the optical klystron. Depending on detuning, three different regimes can be identified. If the perfect tuning condition is maintained for a time long enough (tens of milliseconds), the system displays a transient regime characterized by macro pulses (hundreds of microseconds long) spaced by zero intensity periods (see Fig. 5.2). Eventually, the system reaches a steady state with a constant value of intensity. The first macro pulse will be called “giant pulse” in the following sections and it is the envelope of a train of micro pulses (tens of picoseconds long) with modulated amplitude, as displayed in the inset of Fig. 5.2. Moreover, according to the results presented in this chapter, the micro pulses are characterized by an inner temporal structure showing the presence of few spikes (hundreds of femtoseconds long) which contain most of the emitted energy.

During the FEL process the electron beam energy spread increases (beam heating) and, as a consequence, the FEL gain decreases at the same time (see Eq.2.72). When the gain G is equal to the level of the optical cavity losses L, the system reaches the saturation. During the transient, the FEL growth is faster than the energy spread increase. For this reason the peak power level reached at saturation for macro pulses is higher than in the final steady state, when also the energy spread is thermalized to its stationary value.

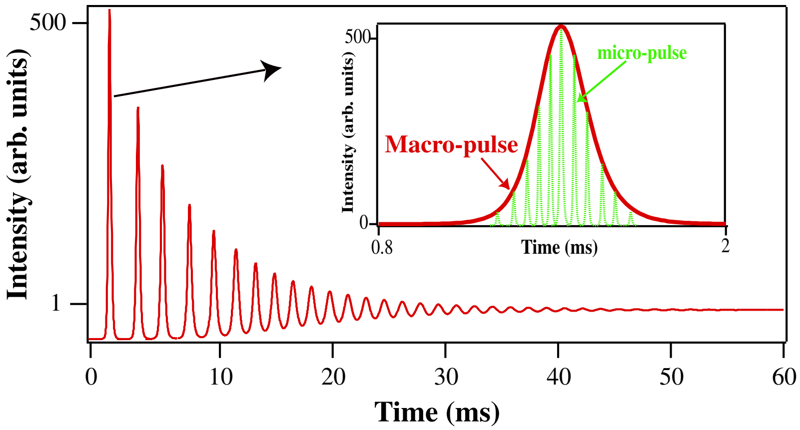

Figure 5.2: *Macro and micro-temporal dynamics of the laser intensity in a SR FEL. The giant pulse is the envelope, represented by a continuous line, of several individual micro pulses, represented by dashed lines.*

In principle, the power level generated during the giant-pulse regime can be predicted using the Renieri limit(see Eq. 2.78), i.e., considering only the energy spread growth. In fact there are two effects that have to be taken into account [2]: the “phase space refreshment” and the temporal spiky structure of micro pulses. The former is a consequence of the synchrotron motion. The electron-beam distribution can be approximated longitudinally with a Gaussian curve and this shape is reflected on the temporal profile of the FEL pulse. The electrons’ energy spread displays a local increase in correspondence of the beam center where the FEL field is stronger. The heated part of the beam is then removed by the synchrotron motion that brings fresh electrons into the interaction region (phase space refreshment). The characteristic time scale for the phase space refreshment corresponds to about half of a synchrotron oscillation (see Section 1.1.2)that in our case is of the order of several tens of microseconds. Indeed, after a complete synchrotron oscillation, the FEL pulse interacts again with the previously heated electrons, no fresh electrons are available anymore and, as a consequence, the gain starts decreasing.

The second effect is due to the origin of the FEL micro pulses. In fact they start from spontaneous emission, with a process similar to the SASE radiation, and, for this reason, they preserve a temporal structure composed of spikes. Each spike exceeds the average level of peak power by about one order of magnitude. Due to this finer structure the phase space refreshment is enhanced, with a further increase of the peak power.

The peak power level reached in giant-pulse mode is orders of magnitude stronger than in free running mode. This feature enhance the possibility to produce coherent harmonic radiation in oscillator SRFELs via nonlinear harmonic generation (NHG).

5.3 Experimental techniques for giant-pulse generation

Experimentally, the giant-pulse production occurs via a suitable manipulation of the FEL gain (gain switch [3]) or losses (Q-switch [4, 5]). Both these methods can be implemented on SRFELs by acting on the light-electron overlap inside the optical klystron. The giant-pulse operation mode has been implemented for the first time at SuperACO [4]. The used Q-switch method is based on a periodic variation of the tuning condition, i.e., when the inter-bunch period is equal to the round-trip of the optical cavity. More recently a gain switch method based on steering the electrons orbit has been developed at Duke SRFEL [6].

The giant-pulse regime at Elettra is obtained using two different experimental techniques, both based on the Q-switch. The first method, called “RF modulation”, is similar to the one implemented at Super-ACO and uses the RF radio frequency signal which controls the revolution period of electrons along the storage ring. The second method relies on a real cavity losses modulation by means of an optical chopper inserted into the laser cavity. The method we implemented uses a spinning disc with a small hole placed into the optical cavity that acts as a mechanical gating, intercepting the FEL light stored in the optical cavity and inducing a periodic depletion of the latter. The periodicity of the radio-frequency changes and the rotating velocity of the chopper determine in the two cases the giant-pulse repetition rate.

5.3.1 RF frequency modulation technique

The Q-switch through RF frequency modulation has been implemented by modulating the frequency of the master oscillator which provides the reference RF signal to the RF cavities of the storage ring. As already mentioned in Ch. 2, the detuning between the revolution periods of electron bunches in the storage ring (related to the RF frequency) and photons in the cavity (related to the cavity length) can affect the FEL interaction and, if sufficiently large, it can turn off the FEL. In practice, the method makes use of detuning in order to control the evolution of the FEL.

The process takes place in four steps (see Fig. 5.3). At the beginning (phase 1), the laser is switched off because the system is completely detuned, due to a significant change of the radio-frequency. The system is maintained in this condition for tens of milliseconds (corresponding to several synchrotron damping times, see Section 1.1.2). During this period the energy spread cools down and the FEL gain recovers its initial value (see Eq. 2.72). Then (phase 2) we restore the light-electron overlap for the time necessary to the creation of a single giant pulse (phase 3, few hundreds of microseconds). Finally, the tuning condition is modified again (phase 4) and the loop can start again in the same way.

By properly choosing the parameters of the modulation (i.e., amplitude of the frequency detuning, slope and duration of the transition), this technique allows to generate a stable train of giant pulses with a peak power two-three orders of magnitude greater than the standard steady-state operation mode. With this method, efficient giant-pulse generation can be realized with a repetition rate of the order of 10–20 Hz.

The process leading the system back to the perfect synchronism has to be quick enough to prevent any significant heating of the electron beam before the perfect tuning is re-established but not so quick to induce strong beam instabilities. Many of the parameters of the process (repetition rate, frequency, detuning, ...) can be freely varied at the Elettra SR [5]. The only limitation is imposed by the minimum time needed to the system for recovering the perfect synchronism. This time is fixed by the response of the RF system to the modulation and it is of the order of hundreds of ns.

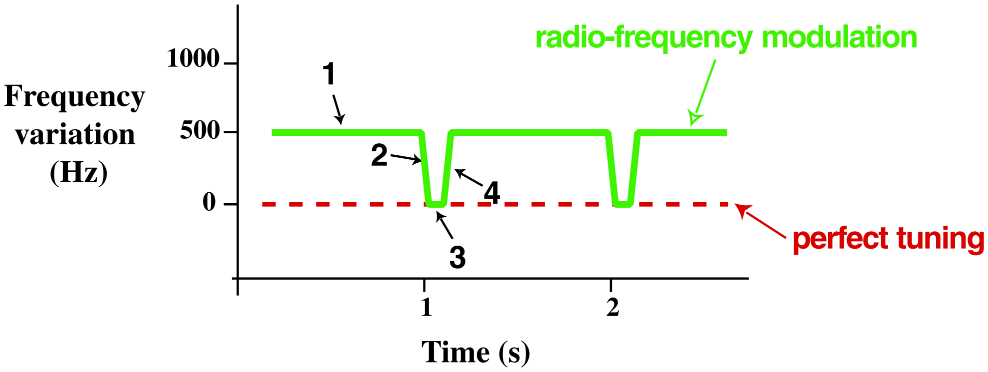

Figure 5.3: *Shape of the signal used for the frequency modulation of the RF provided by the master oscillator to the storage ring. Starting from a detuned condition (1) that inhibits FEL emission, the tuning is quickly established (2,3) allowing the growth of a FEL giant pulse. After the emission of the giant pulse, the system is detuned again (4). The electron beam energy spread recovers its initial value and, eventually, a new cycle can start.*

Figure 5.4a shows a streak camera image in which are displayed, at the same time, the synchrotron radiation and the FEL signal. Along the vertical axis of the picture, one can follow the temporal evolution of the distribution profile. This example demonstrates that if the RF jump is too quick, it can cause beam perturbations. In particular, one can see that the synchrotron oscillations start before the laser onset. This effect is more clear in the analysis of the streak camera image. When the tuning condition is (re-)established, there is a quick jump of the centroid position of the electron beam (see Fig. 5.4b). The recovered tuning condition allows the FEL interaction and as a consequence the electron beam starts to manifests the heating in the energy spread increase and bunch lengthening. The maximum length is reached just after the peak of the giant pulse (Fig. 5.4b).

This method does not allow the possibility to use the RF signal as a reference for synchronization or timing diagnostic purposes. Thus, in the case one is interested in synchronizing external systems, it is important to find an alternative solution to generate giant pulses.

5.3.2 Chopper technique

An alternative method to RF modulation for performing Q-switch operation on SRFELs is related to the possibility of implementing into the optical cavity a mechanical gating (see Fig. 5.5). This possibility has been explored at Elettra by inserting into a dedicated vacuum chamber in the FEL beam line an optical chopper (Fig. 5.6a).

The chopper chamber is placed between the back-end and the back cavity mirror (Fig. 5.6b). The distance of the chopper from the back mirror is about 80 cm. In that position, the dimension of the TEM00 Gaussian beam, defined by the used cavity mirrors, is of the order of 3–4 mm depending on the operation wavelength. Characteristics of the chopper disc should be defined in order to guarantee the required ratio between the extinction time (FEL off > 100 ms) and active time (FEL on ~hundreds of μs). We then

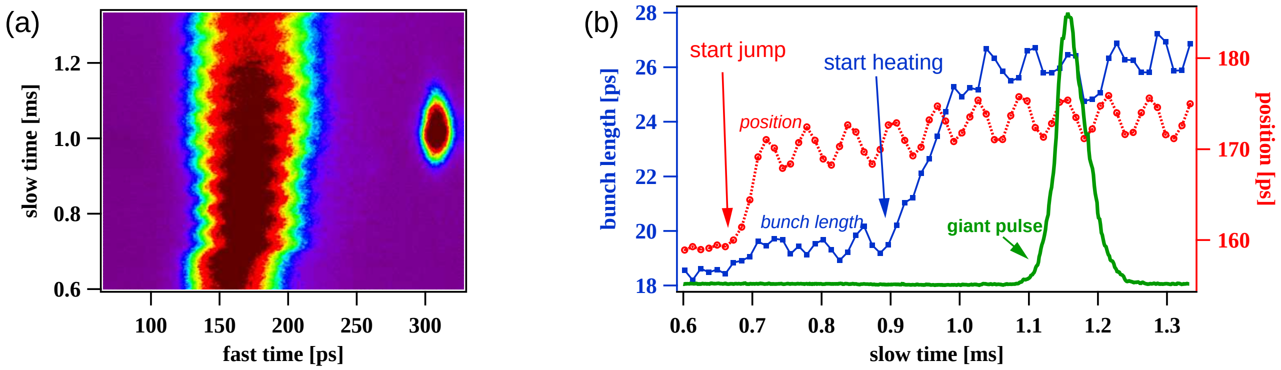

Figure 5.4: *(a) Streak-camera image of the electron beam (left trace) and of the FEL pulse (right trace) in Q-switch operation mode and corresponding analysis (b). Through a frequency modulation of the RF signal the resonant condition is established at t=0.2 ms. As a consequence the electron bunch shows a quick jump in temporal position (red trace fig(b)) and some instabilities are excited providing evident synchrotron oscillations. The major effect of the recovered tuning condition is the growth of the FEL pulse associated to the bunch length growth (green and blue trace respectively). Experimental conditions: electron beam current≃8 mA, energy=0.9 GeV, amplitude and slope of the RF jump: 600 Hz, 40 Hz/μs, resonant wavelength=250 nm.*

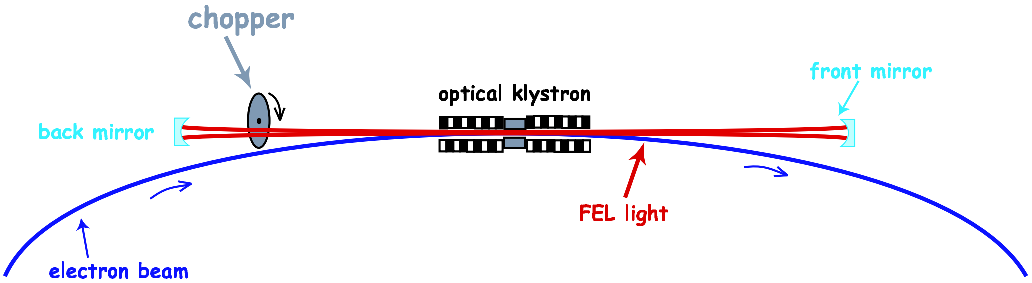

Figure 5.5: *An optical chopper has been placed in the optical cavity of the Elettra SRFEL in order to allow Q-switch operations.*

use a molybdenum disc with a 115 mm radius with a little aperture positioned close to the border (see Fig. 5.6a).

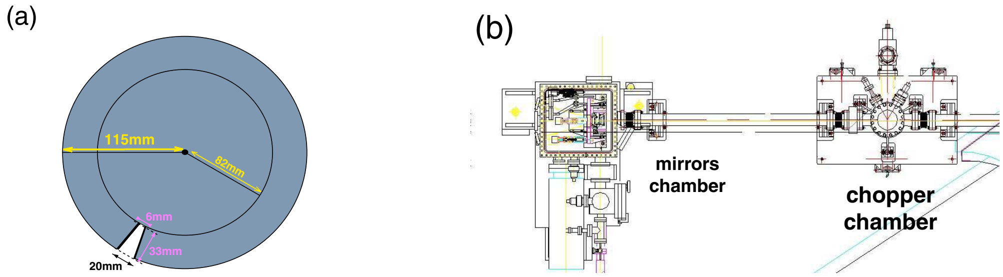

Figure 5.6: *Chopper: (a) schematic design of the metallic disc, (b) chopper position with respect to mirrors chamber.*

The used dimension for the hole (Fig. 5.6a) is sufficiently larger than the FEL beam dimension at the chopper position and allows its operation when the revolution frequency is in the range from 0 to 50 Hz. A PHYTRON UHV stepper motor provides the necessary fast rotation of the chopper at constant frequency. At present, due to some limitation of the used motor, the chopper can achieve only repetition rates lower than 5 Hz. Nevertheless, we expect in the near future to be able to upgrade it and operate the chopper up to frequencies of 10 Hz or even larger. When correctly placed, the chopper assures that the FEL emission can be generated only if the small hole is on the axis of the optical cavity, while for the rest of the time the disc intercepts the radiation and does not allow the FEL growth. As a consequence, short FEL pulses are generated, separated by long quiescent periods, as requested for the giant-pulse production. This optical method for Q-switch operation does not introduce perturbations on the electron beam and, therefore, higher power and better stability may be expected in in the giant-pulse regime. Furthermore, since the chopper Q-switch does not involve the RF frequency, the latter can be used as a clock for diagnostic and synchronization purposes. This is an important point when one is interested to perform cross-correlation measurement that are useful for a temporal characterization of micro pulses within the giant-pulse regime.
In summary, the chopper advantages with respect to the RF technique is that it does not induce beam perturbation, but, since the transition time is set by the repetition rate and cannot be regulated otherwise, the chopper Q-switch takes generally a longer transition time and thus it is supposed to provide giant pulses with lower gain at low repetition rates with respect to RF modulation.

Some pictures of the chopper during the commissioning are shown in Fig. 5.7.

5.4 Characterization of FEL macro pulses

In order to characterize the giant-pulse regime, the experimental setup has been optimized to simultaneously detect the fundamental FEL radiation as well as its coherent harmonics (see Fig. 5.8). The fundamental and the harmonic radiation travel along the same path until a beam splitter deflects a small portion of the light towards a fast photodiode. Since the ratio between harmonic and fundamental signals is very small, the photodiode

Figure 5.7: *Pictures of the chopper. a) Preliminary studies in air. b) and c) during the installation.*

basically detects only the fundamental radiation. Most of the radiation is sent to the monochromator that selects the band around the harmonic and the monochromatized light is detected by a photomultiplier (PMT). The signal from the photodiode and the PMT are acquired at the same time by a digital oscilloscope. This setup is used for both the RF modulation and the chopper technique. It is important to note that both detectors are fast enough to detect the micro-pulsed structure of the giant pulse but do not provide any useful information about real temporal characteristic of micro pulses which is in the picoseconds scale, far beyond the bandwidth limit of the used detectors and oscilloscope.

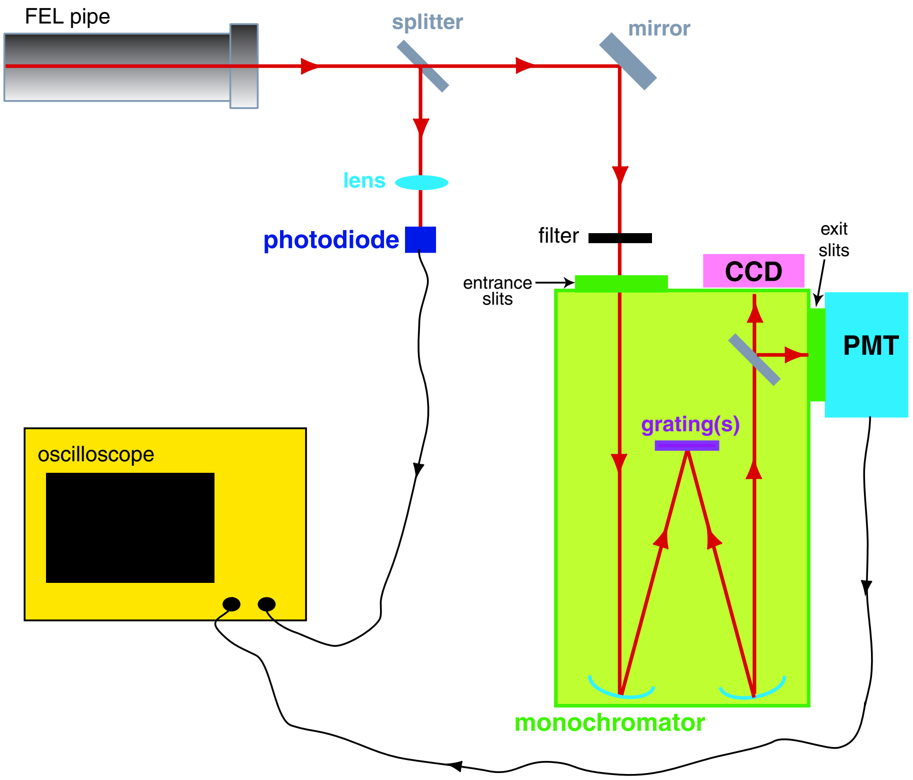

Figure 5.8: *Experimental setup for FEL acquisition in Q-switch regime. The signals from the photodiode and the photomultiplier are acquired at the same time by the oscilloscope, that is triggered by the signal that induces the RF frequency modulation.*

Temporal characterization of micro pulses has been done using the streak camera (2-3 ps resolution) and also with cross-correlation techniques. Moreover, also spectral measurements of the signal can be done either using the CCD installed on the monochromator or in scanning mode using the PMT and moving the transmission wavelength of the monochromator. This second option has been used in the case of the characterization of the harmonic radiation since it allows to suppress the contribution from the spontaneous synchrotron emission which has a much higher repetition rate

5.4.1 Temporal characterization of macro pulses

Figure 5.9 (left) shows a typical simultaneous measurement of fundamental (462 nm) and third harmonic (154 nm) radiation obtained with RF modulation technique. The zoom of the macropulses (at right) shows that they are the envelope of micro pulses separated by the inter-bunch period. Although in the zoom window (corresponding to few μs) the micro-pulse intensity should be almost constant, some fluctuations are visible. This can be ascribed to electron beam fluctuations at this time scale. The giant-pulse risetime, highlighted in Fig. 5.9 (left top) with a black line, is used to calculate the gain, as will be explained in the next section.

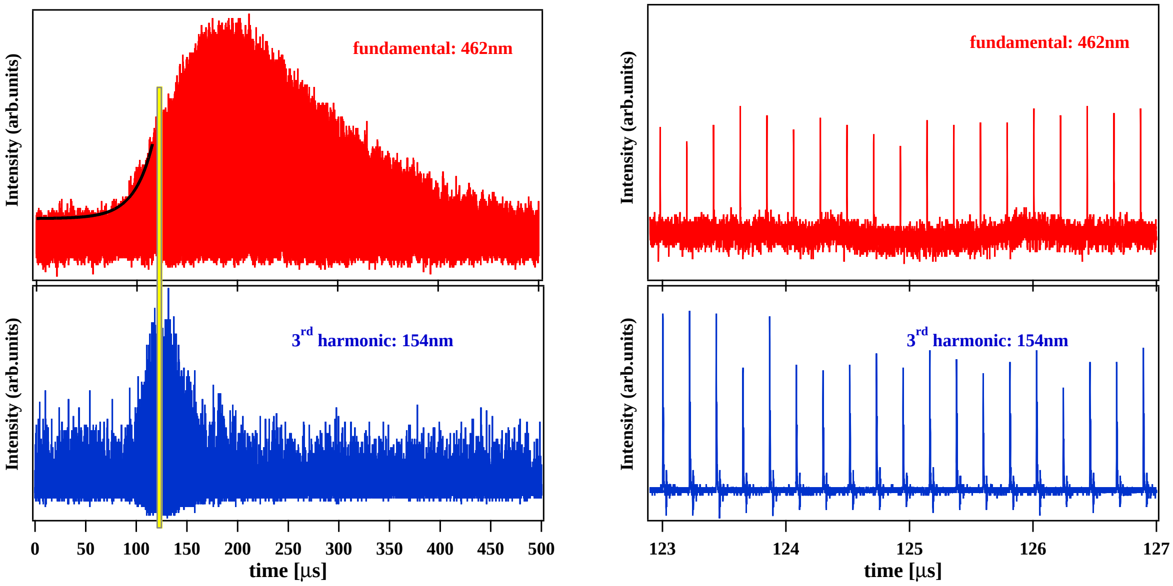

Figure 5.9: *Fundamental and harmonic macro pulses obtained using RF modulation. The upper trace has been detected by the photodiode, the bottom one by the PMT. The images at right are a zoom of the boxes in the left pictures. Current (four bunches): 8.7 mA. Electron beam energy: 750 MeV.*

Using a different couple of mirrors, we obtained fundamental radiation at 660 nm and harmonic radiation at 220 nm by means of the chopper technique (see Fig. 5.10). The fundamental macro-pulse shape looks different form Fig. 5.9 probably due to saturation of the detector. Also in this case, the pictures at right show a zoom of both macro pulses. Besides, the intensity of micro pulses display some fluctuations, as in Fig. 5.9(right part) .

Quantitatively, the giant-pulse duration and the risetime are the sensitive parameters, since the former is connected to the emitted power and the latter to the gain of the process. A large number of measurements both using RF modulation and chopper

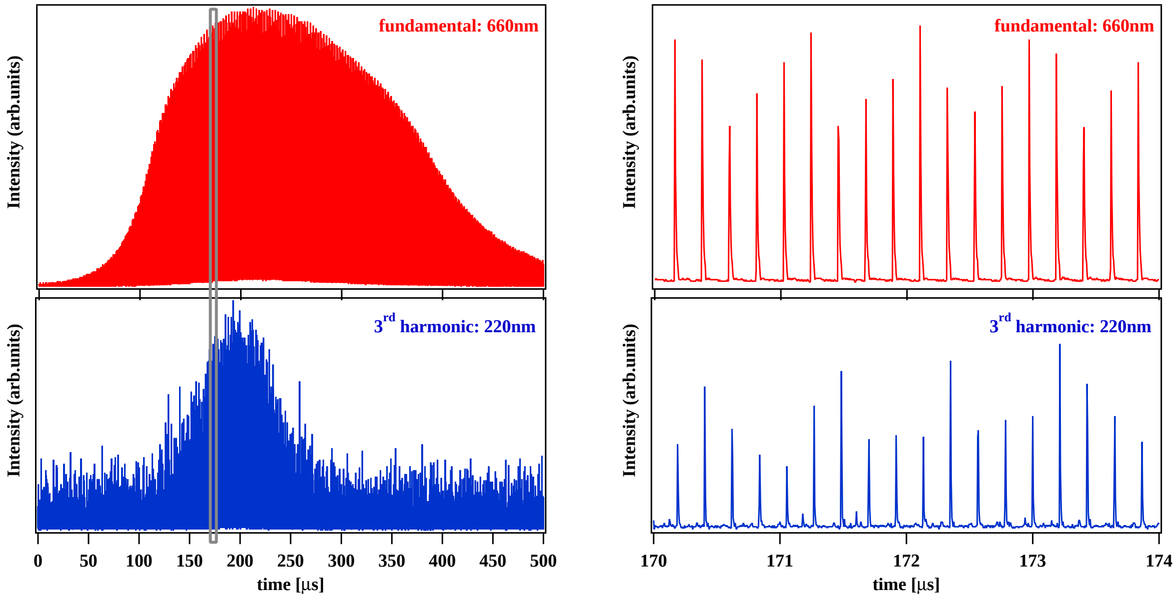

Figure 5.10: *Fundamental and harmonic macro pulses obtained using chopper technique. The images at right are a zoom of the gray box in the pictures at left. Current (four bunches): 6.2 mA. Repetition rate=3 Hz.*

techniques, performed in different experimental conditions (different ring current, fundamental wavelength, repetition rate, ...), has shown that the fundamental macro pulse has a longer risetime respect to the harmonic. In several cases we estimated that the harmonic risetime is about 3 times shorter than the fundamental. This difference is in good agreement with the theory that predicts for the field at the fundamental and the harmonic the following relation: $A_h \propto A_1^h$ [7].

Stability: Sequences of giant pulses

In order to study the stability of the fundamental giant-pulse intensity and the risetime, we acquired sequences of 100 giant pulses. Being the detuning curve about 100 Hz (full width at half maximum (FWHM)) large, we set a detuning of the RF equal to -80 Hz with respect to the nominal value. Then a signal provided by a waveform generator, with a pulse amplitude 1 V, length 1 ms and risetime 50μs, is applied to the RF frequency. The modulation depth is 100 Hz per 1 V. Figure 5.11 shows a sequence of 100 giant pulses obtained with the RF modulation. The train is stable in amplitude and in time.

During giant-pulse production, the FEL interaction causes the electron-beam heating. The bunch lengthening, related also to the energy spread growth, can be detected using the streak camera, as shown in Fig. 5.12. In this case, the amplitude and the slope of the RF jump have been chosen in order to minimize beam perturbations.

Figures 5.13 and 5.14 report similar results obtained using the chopper technique. Data reported in Fig. 5.13 show a sequence of 100 giant pulses acquired with the photodiode. Also using this technique,the stability in time and intensity is good.

Figure 5.14 shows a streak camera image of the electron beam showing the effect of the giant-pulse production on the electron bunch. From the analysis of the streak camera image, it is possible to notice the bunch lengthening. Also in this case the bunch length

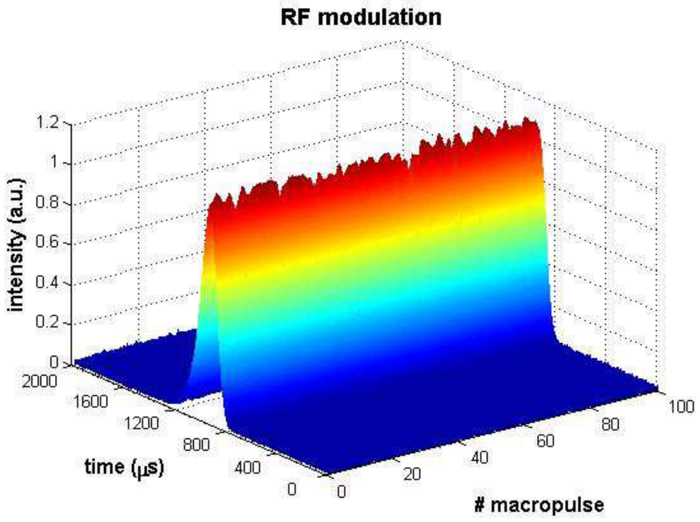

Figure 5.11: *Sequence of 100 giant pulses obtained with the RF modulation. Current: 4.8 mA, Rep. rate: 3 Hz. The driving signal has amplitude 1 V, duration 1 ms and risetime 50μs. The modulation depth was 100 Hz per 1 V, starting from -80 Hz.*

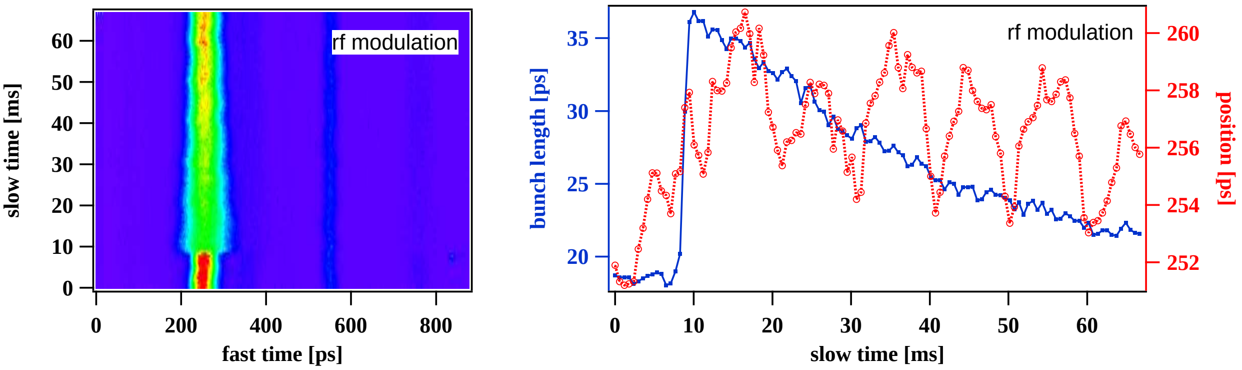

Figure 5.12: *At left: streak camera image acquired during RF modulation. At right: analysis of the image at left showing the shift of the centroid position before the bunch lengthening.*

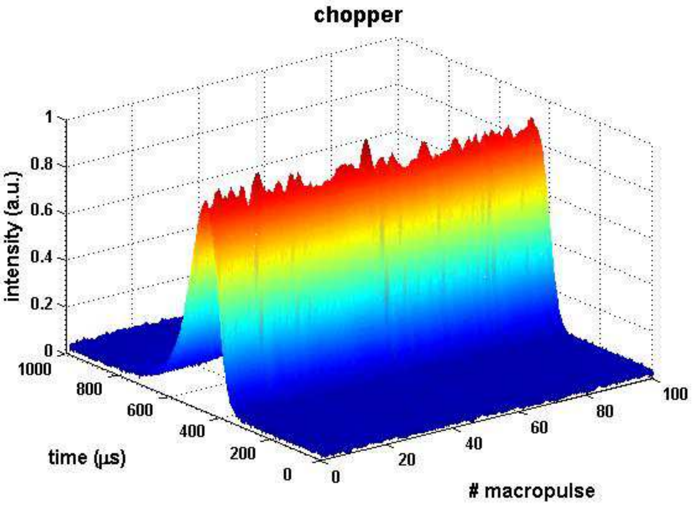

Figure 5.13: *Sequence of 100 giant pulses obtained with the chopper technique. Electron energy: 0.9 GeV. Current: 4.5 mA, Rep. rate: 3 Hz.*

doubles, as already seen in the RF modulation method (see Fig. 5.12b).
As already anticipated, the Q-switch with the chopper does not perturb directly the electron beam. Indeed, Fig.5.14b does not show any significant displacement in time for the centroid of the electron-beam distribution as in the case of RF modulation. Moreover, the chopper technique does not excite synchrotron oscillations, that can degrade the gain of the giant pulse.

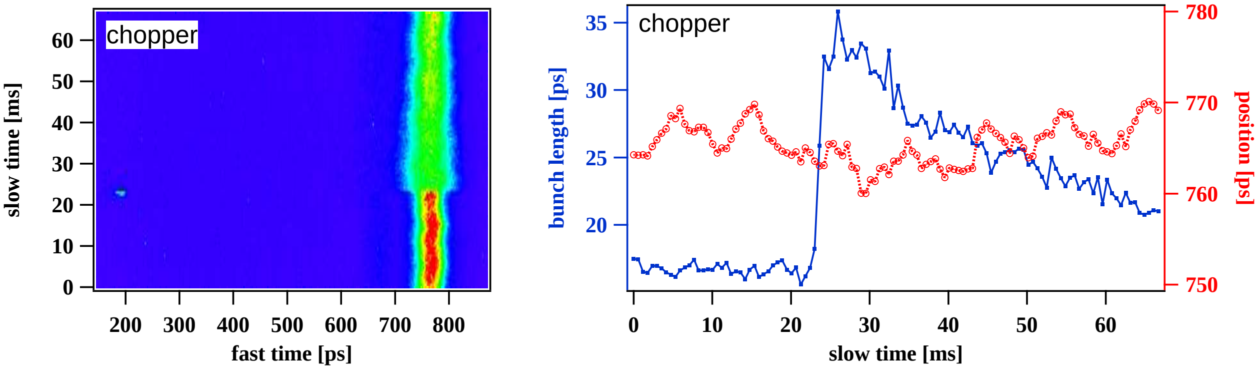

Figure 5.14: *At left: streak camera image acquired during chopper giant pulse production. At right: analysis of the image at left showing the evolution of the centroid position and the bunch lengthening due to the creation of the giant pulse.*

Comparison RF modulation vs. chopper

We performed systematic acquisitions of macro pulses obtained using both techniques at different repetition rates. Figure 5.15 shows two sequences acquired in succession and obtained with the two methods at 3 Hz. A direct comparison displays that the chopper sequence is much more stable in terms of time, while the data obtained with RF modulation show a temporal jitter in the macro-pulse centroid.

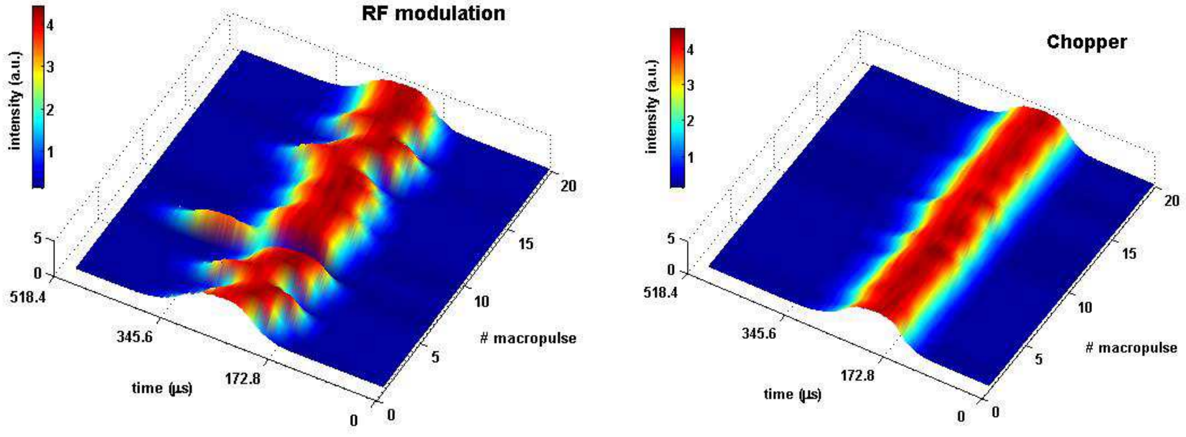

Figure 5.15: *Sequences of 20 macro pulses obtained with RF modulation (at left) and with chopper technique (at right). The two sequences have been acquired in succession. The repetition rate is in both cases 3 Hz. Current=15 mA.*

In Figs. 5.16-5.17 we report the analysis of data acquired in similar experimental conditions. The effective (or net) gain[1] g has been calculated from the risetime τ of the giant pulse following the relation: $g = T_0/\tau$, where T_0 is the inter-bunch period.
In Fig. 5.16 it is reported the net gain as a function of the electron beam current for the two techniques at 3 Hz and 1.5 Hz. At higher repetition rate (3 Hz), the two techniques seem comparable at high current (15 mA), while at lower repetition rate (1.5 Hz) the RF modulation, having a faster transition time, displays a higher gain with respect to the chopper modulation.

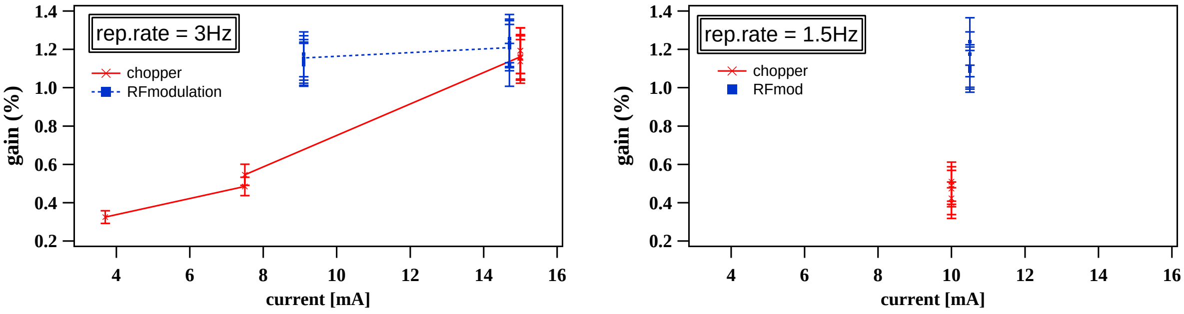

Figure 5.16: *Net gain as function of the beam current for chopper and RF modulation techniques at different repetition rates: at left 3 Hz and at right 1.5 Hz.*

Figure 5.17 shows the net gain as function of the beam current for different repetition rates and for both RF modulation (left) and the chopper (right) Q-switch techniques. The data shown confirmed the previous results and the expectations: the chopper technique is not suitable for low repetition rates (lower than 2 Hz) since the gain is lower than the RF modulation one. Besides, we found that the RF modulation method is less sensitive to the beam current than the chopper technique. This unexpected feature is still an open point and should be investigated in dedicated shifts.

---

[1] It is customary to calculate the (total) gain G adding at the net gain g the losses of the optical cavity.

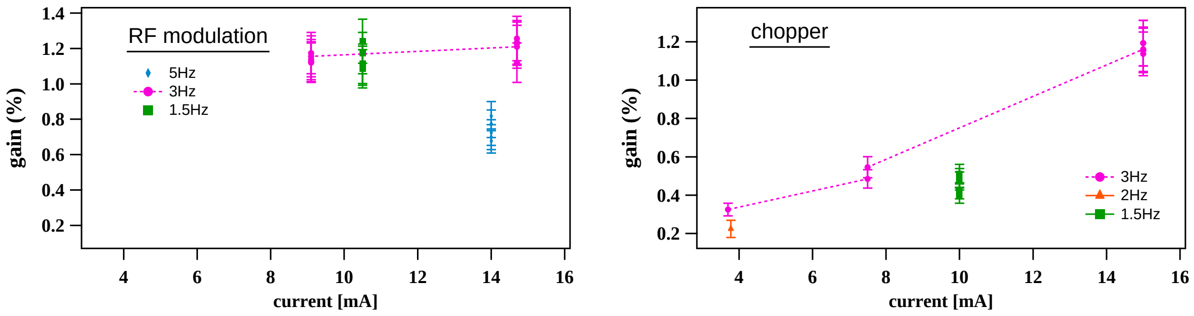

Figure 5.17: *Net gain as function of the beam current at different repetition rates for RF modulation (left) and for chopper (right) techniques.*

The duration of a fundamental macro pulse can be also measured by a streak camera and it is usually 100-150μs (FWHM). The harmonic macro pulse is significantly shorter because the harmonic generation happens only when the fundamental field is strong enough.

5.5 Characterization of FEL micro pulses

5.5.1 Temporal characterization of micro pulses

The temporal characterization of fundamental and harmonic micro pulses can be done by using the dual-sweep streak camera. The measurements reported in Fig. 5.18 show that the fundamental micro-pulse duration is about 5 ps (root mean square (RMS)) while the harmonic micro-pulse duration is about 2 ps (RMS). However the harmonic signal is at the limit of the instrument resolution [8] and another technique has to be use in order to measure it.

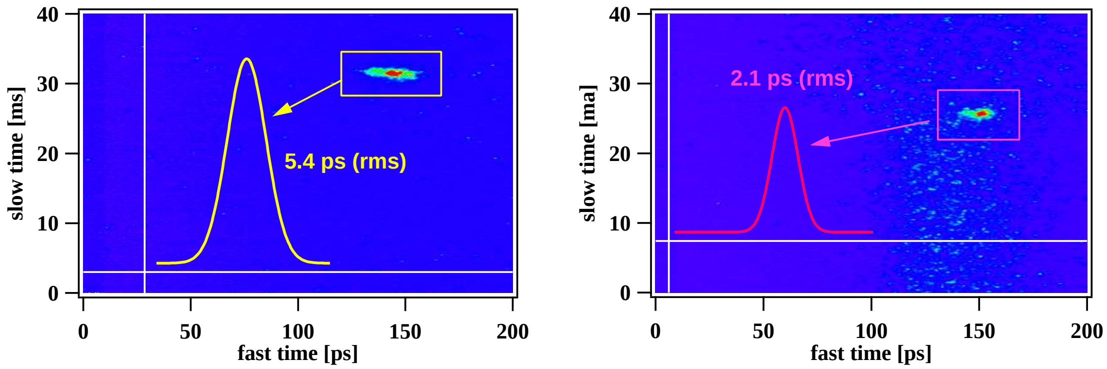

Figure 5.18: *Streak camera images of the fundamental (left) and harmonic (right) macro pulses. Micro-pulse profiles and their durations are also shown.*

Micro-pulse duration measurement with background-free cross correlation technique

As mentioned before, the harmonic micro pulses have a duration that is under the streak camera resolution (about 2 ps). In principle, the measurement of their duration can be performed by means of a cross correlation technique. For this purpose, one can combine the harmonic pulse with an external laser (e.g., a Cr:LISAF, see Fig. 5.19). As first step, we validated the technique with the fundamental radiation at 660 nm. The experimental setup (including the electronic part) is shown in Fig. 5.19.

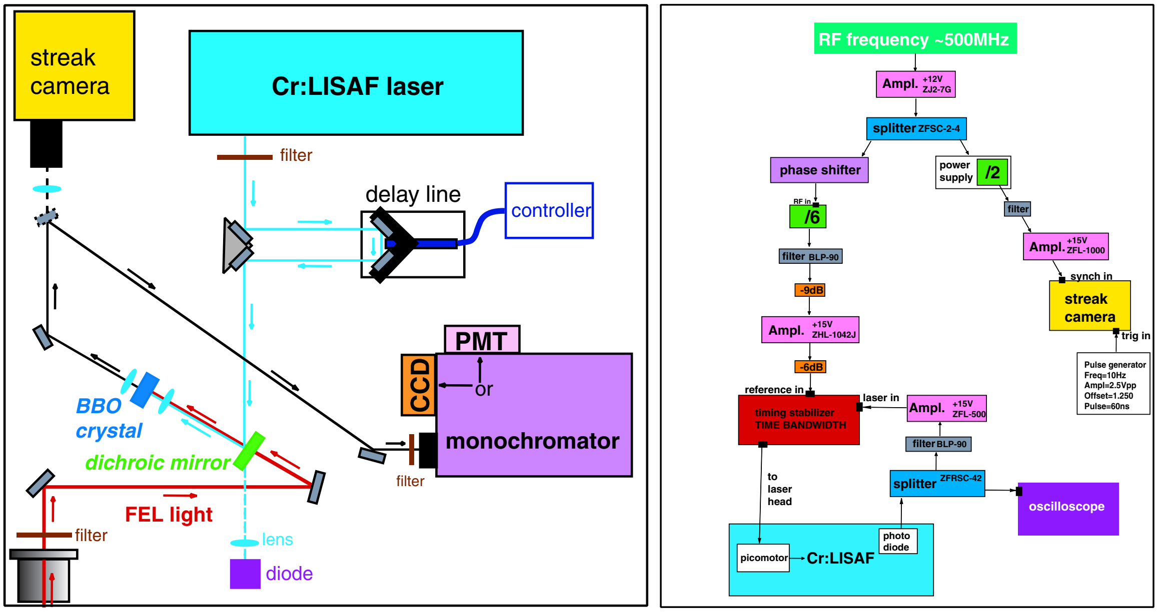

Figure 5.19: *Left picture: layout of the experimental setup for the cross correlation measurement of the fundamental micro-pulse length. Right picture: electronic setup for the measurement.*

The FEL radiation (660 nm) and the Cr:LISAF light (850 nm) entering in a non-linear β-barium-borate (BBO) crystal create radiation at 370 nm (sum of frequencies). This radiation is sent by a mirror to the monochromator. The dichroic mirror (which reflects the laser and is crossed by the FEL) allows the spatial overlap between the FEL and the laser. The delay line, together with the phase shifter (see Fig. 5.19), controls the temporal overlap. The delay can be changed by hand or using a dedicated LabVIEW software. Due to problems involving the stability of the laser and the FEL-laser alignment, we performed only two sets of measurements. The first scan was performed by hand, moving the delay line using the controller, recording the encoder value and the number of counts displayed in the monochromator. The result is shown in Fig. 5.20. A Gaussian fit of the data gives a pulse duration of 4.0±0.7 ps (RMS) that is close to the streak camera measurements (5–6 ps (RMS)).

The second scan has been performed using dedicated LabVIEW software. The result is shown in Fig. 5.21. Although this measurement (that shows a double peak) is probably affected by the instability of the Cr:LISAF, the single peak width (10 ps (FWHM)) is in agreement with previous results.

The further step is the measurement of the third harmonic micro-pulse duration at 220 nm. For this purpose the setup has been changed and it is shown in Fig. 5.22. The harmonic FEL emission is combined in a BB0 crystal with the Cr:LISAF radiation. Their temporal overlap is suitably controlled by means of a delay line that modifies the Cr:LISAF path length. If superimposed, they can produce radiation at about 297 nm (difference of frequencies). The monochromator, put after the BBO crystal, is set to filter

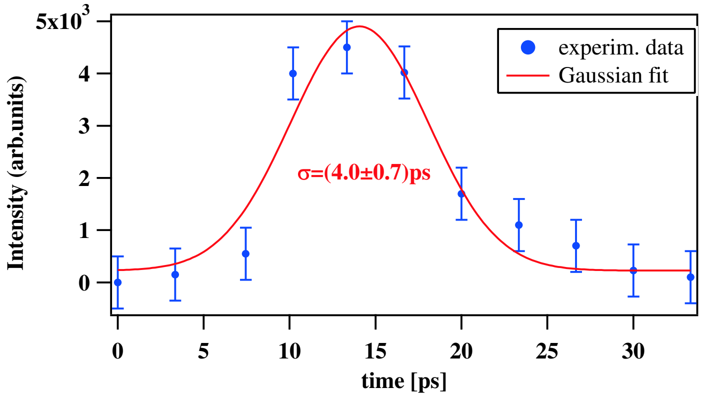

Figure 5.20: *Fundamental pulse length measurement (manual scan).*

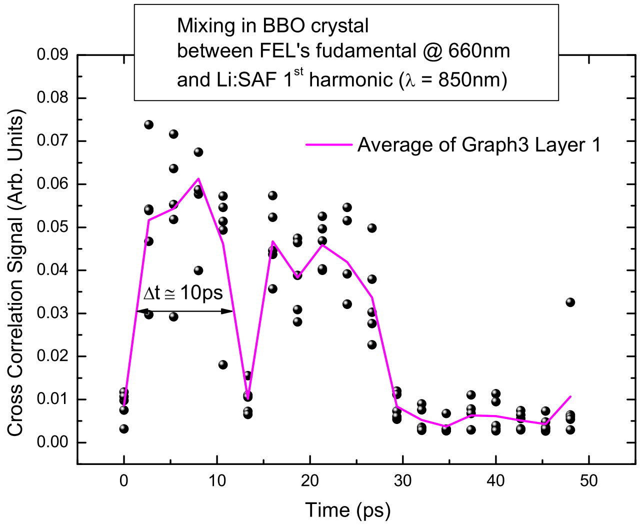

Figure 5.21: *Fundamental pulse length measurement (software scan).*

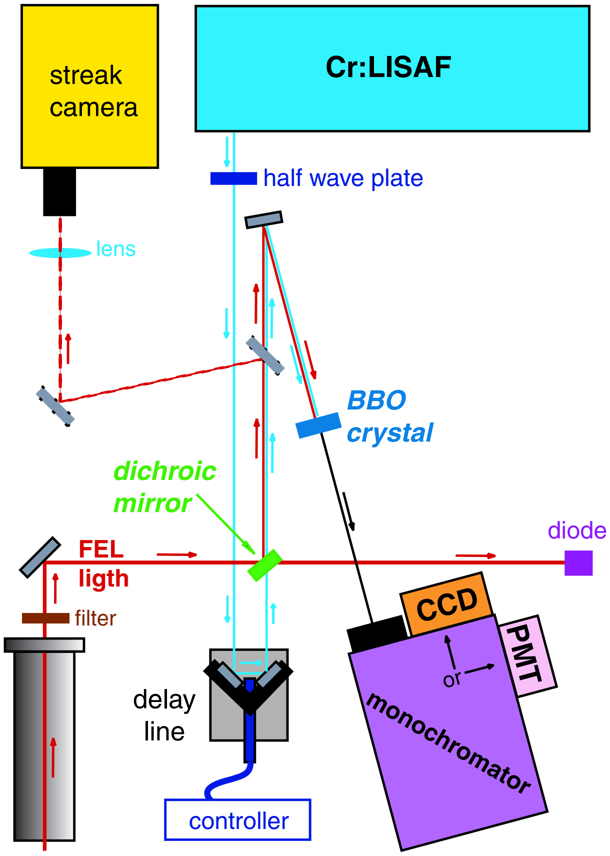

Figure 5.22: *Experimental setup for the harmonic micro-pulse length measurement.*

this wavelength that is then detected by a CCD or by a photomultiplier, which signal is acquired by an oscilloscope. By means of a dichroic mirror, the fundamental FEL radiation is monitored by a photodiode acquired by an oscilloscope. An aluminum coated mirror, suitably placed to intercept both the FEL harmonic signal and the Cr:LISAF, allows to send these emissions to the streak camera in order to control their temporal overlap.

We dedicated only few shifts at this measurement and, in spite of the experience gained in the fundamental micro-pulse duration measurement, our attempt does not succeed. The failure can be put down to the large number of degrees of freedom of the setup. In particular, the stability of synchronization of Cr:LISAF was very poor (jitter between the laser and the reference signal quite high) and the power level of the harmonic signal was quite low.

The measurement of the harmonic micro-pulse length, in similar experimental conditions, can be done more easily with a more powerful and stable laser (like a fiber laser).

5.5.2 Spectral measurements

The spectral profiles of the fundamental and third harmonic signals have been measured using the monochromator in scanning mode. The results are shown in Fig. 5.23. The width of the fundamental is 0.6 nm (FWHM) and that of the third harmonic is 0.26 nm.

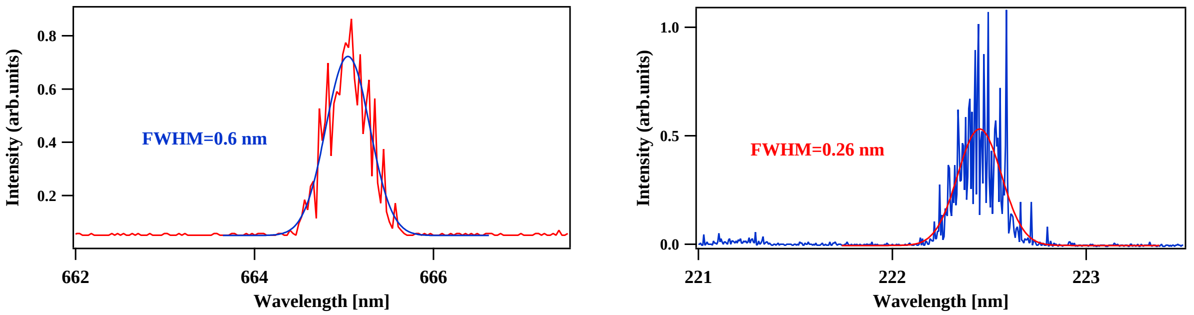

Figure 5.23: *Left picture: spectral profile of the fundamental signal at 665 nm. The width is 0.6 nm (FWHM). Experimental conditions: 2 Hz, 4 nm/mm. Right picture: spectral profile of the third harmonic signal at 222.5 nm. The width is 0.26 nm (FWHM). Experimental conditions: 3 Hz, 1 nm/mm.*

Assuming that both the fundamental and the harmonic radiations are transform limited, the temporal duration can be easily calculated by the following relation:

$$\frac{c\,\Delta t\,[FWHM, s]\,\Delta\lambda[FWHM, m]}{\lambda^2[m]} = 0.441 \qquad \text{(for a Gaussian beam).} \tag{5.1}$$

In the reported case, we obtain a pulse duration of about 1 ps for the fundamental wavelength while for the third harmonic signal the duration is about 280 fs. These values are below the resolution of our faster detector (streak camera) and a direct experimental confirmation is not possible. Nevertheless, these results give an indication of the fact that the micro pulses have a sub-structure and that the majority of the power is contained in few spikes. Sub-structures inside both the fundamental and harmonic micro pulses have been measured at Duke. The same measurement is impossible at Elettra because, even if our streak camera has a similar resolution (2-3 ps), the Elettra bunch is three times shorter than the one at Duke and, as a consequence, also the micro pulses and the structures inside them are shorter. More details on the spikes will be given in Section 5.6.2.

5.6 Giant-pulse simulation

As it has been shown, the possibilities to completely characterize the temporal properties of the radiation emitted by FEL in giant-pulse regime are limited by the lack of available instrumentation with the required resolution. It has been largely demonstrated that the FEL interaction occurring in the optical klystron can be well reproduced by 3D numerical codes available within the FEL community (Ginger [9], GENESIS [10], `Medusa` [11]). Moreover it is possible to simulate the propagation of electrons along the storage ring considering a one-turn map for the longitudinal and transverse evolutions (see Eqs. 1.21 and Eqs. 1.4, respectively) while the radiation is propagated along the optical cavity according to the mirror specifications. Then a complete description of the FEL process in a SRFEL during giant pulse can be numerical reproduced by properly integrating the three process in a simulation. In addition, some FEL codes allow taking into account nonlinear harmonic generation (NHG). With this option, it is possible to study the generation of harmonic spikes during giant pulses in SRFEL. However, some modifications to existing codes have to be done in order to simultaneously accomplish the requirements of multi-pass FEL simulations imposed by the oscillator configuration and the recursive interaction with the same electron bunches circulating into the storage ring. In collaboration with the Author of the code, W.M.Fawley, it has been decided to modify the FEL numerical code Ginger in order to fulfill these requirements. In particular, the code now allows to use as an input for the electron beam the macroparticles that another numerical code propagates along the storage ring. Moreover, the modified version of Ginger provides as an output the macroparticles information at the exit of the optical klystron. This is used for the electron bunch propagation along the ring and to initiate the following iteration. For the light propagation inside the optical cavity we have considered monochromatic radiation (single-frequency approximation) and we propagate only the intensity of the optical field (the phase is neglected), according to Eq. 2.62. Transversally, we approximate the optical propagation by considering all the emission contained within the resonant TEM00 Gaussian mode of the optical cavity.

In order to perform simulations that can reproduce the main features of the FEL evolution, it is important to take into account the different time scales involved in the process. Key temporal durations are the giant-pulse length (hundreds of microseconds), the revolution period (hundreds of nanoseconds), the bunch length (tens of picoseconds), the slippage length (hundreds of femtoseconds). Among them, the most important are the bunch and the slippage lengths that are used to define the number of slices and particles needed. Since the synchrotron motion (that mixes electrons within the bunch) is responsible for the phase space refreshment, it is necessary to simulate the entire bunch, although the radiation is produced by a small portion of that. Besides, to investigate the possible finer structure it is necessary to space properly the simulated slices. Since the spikes duration should be close to the slippage length, the distance between slices have to be sufficiently smaller than the slippage. For this reason, the minimal number of required slices is very large. Moreover, the number of macroparticles can not be small, because should be able to describe the real distribution of electrons, at least in the central part of the bunch which is more involved in the FEL process. Therefore, the final number of macroparticles that is necessary to simulate easily exceeds the million. This strongly affects the necessary time for accurate SRFEL simulation. New sorting procedures and parallelization of sub programs have been implemented in order to reduce the CPU time.

5.6.1 Numerical results

The suite of codes has been then used for simulating the Elettra SRFEL configuration. In the selected case, the fundamental emission is at 660 nm and its third harmonic radiation is at 220 nm. The parameters used in the simulation are reported in table 5.1. As a first result, we are able to reproduce the macro-pulse envelope both for the fundamental and the harmonic radiation. The reported data presented in Fig. 5.24 compare the results of simulations with experimental measurements obtained in equivalent conditions. The good agreement between experiments and simulations suggests the validity of our approximations and procedure. In particular, the results for harmonic signals (Fig. 5.24b) can provide a validation of the new feature of the used XGINGERH code that has been recently upgraded for the simulation of even harmonic emission in planar undulators [12]. The analysis of the data reported in Fig. 5.24 shows that the temporal evolution of a single macro pulse lasts in all few hundreds of microseconds for the fundamental wavelength and about half for the harmonic. The risetime of the harmonic signal is significantly shorter, about a factor 3, as already observed in experimental data. The net gain of the fundamental simulated macro pulse, calculated from the risetime, is 2%. The total gain G is thus about 4%. The experimental data show a bit longer risetime, then the gain is slightly low.

electron beam energy	900 MeV
peak current	32 A
normalized transverse emittance (y)	$2.5{\cdot}10^{-7}$ rad m
normalized transverse emittance (x)	$2.5{\cdot}10^{-6}$ rad m
relative laser-off energy spread (RMS)	$0.86{\cdot}10^{-3}$
laser-off bunch duration(RMS)	16 ps
fundamental wavelength	660 nm
cavity losses	2%
FEL waist	740μm
number of undulator period	20
undulator length	2 m
dispersive section length	0.5 m
optical klystron total length	4.5 m
dispersive section strength (R_{56})	70μm

Table 5.1: *Electron beam and optical klystron parameters used in Ginger+one-turn map simulation relative to Fig. 5.24.*

As demonstrated by data reported in Fig. 5.25, numerical simulations can also reproduce the dependence of results on some parameters. Figure 5.25 shows both fundamental and harmonic power as a function of the dispersive section strength R_{56}. The

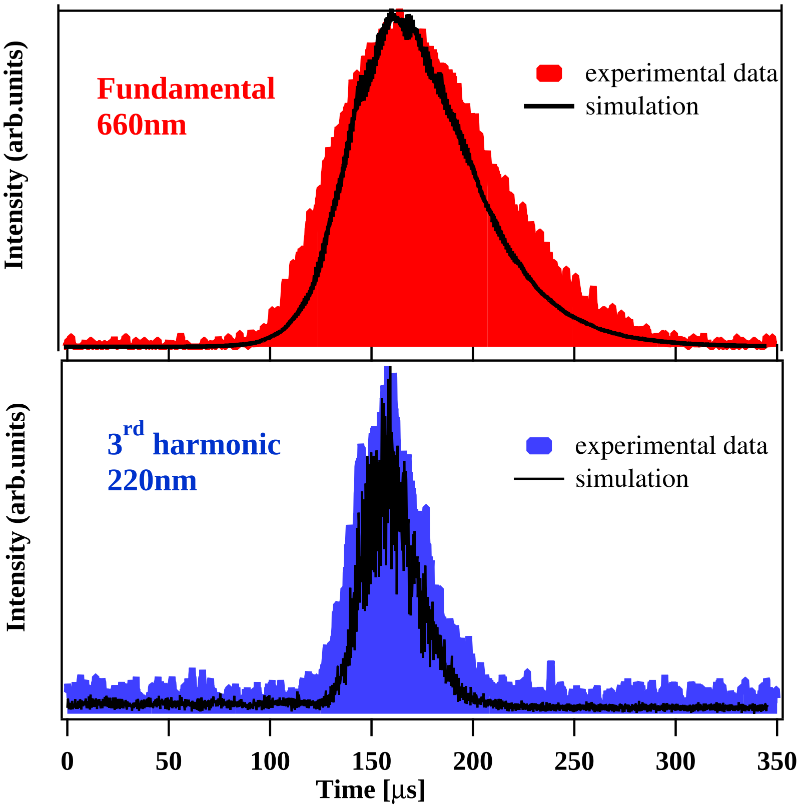

Figure 5.24: *Comparison between simulation and measurement: Simultaneous evolution of fundamental (upper traces) and harmonic (lower traces) macro pulses. The macro pulses are composed of a train of micro pulses separated by the inter-bunch period. Beam energy=0.9 GeV, peak current=32 A, laser off bunch duration=16 ps, cavity losses=2%,* R_{56}*=70µ m.*

trend obtained with Ginger simulations is similar to the experimental result both for the fundamental and the harmonic emission: the maximum for the fundamental emission corresponds to a lower R_{56} with respect to the harmonic one. Quantitatively, the discrepancy between simulation and data is of 10μm in the case of the fundamental wavelength, while for the harmonic is only 5μm. The relative distance between fundamental and harmonic peaks is 10μm according to simulation and 25μm according to measurements. Obviously, the experiment is affected by uncontrollable sources of errors that should change during successive acquisitions. Nevertheless, despite this small disagreement, the simulations reproduce overall the experimental results.

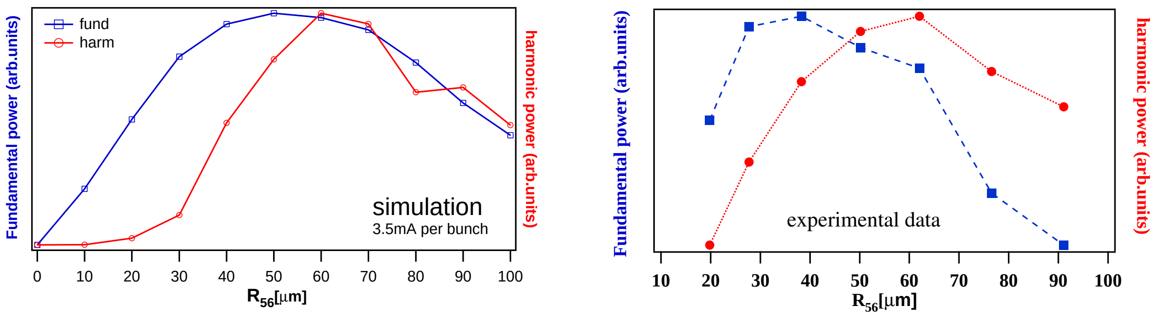

Figure 5.25: *Fundamental and harmonic power as a function of dispersive section strength* R_{56}*. The direct comparison between simulation (at left) and experimental data (at right) shows a similar trend with the fundamental maximum at lower* R_{56} *than the harmonic one.*

The evolution of electron-beam phase space during the giant pulse evolution is shown in Fig. 5.26. Starting from an initial Gaussian profile both for the energy and the time, the distribution appears strongly distorted by the laser onset. The induced energy spread, initially concentrated when there is the maximum gain (i.e., corresponding to the beam centroid), is then smeared on the whole bunch by synchrotron motion over several turns. Similar results are reported in [13] and [2].

Moreover, the simulations performed with Ginger [9] demonstrate that not only at Duke but also in the Elettra case the micro pulse is made of few/several spikes. Figure 5.27 shows a pseudo streak camera image of the fundamental pulse and of the corresponding electron beam. With respect to the real streak camera pictures, the fast time and the slow time axes are swapped. Performing a vertical cut on the image, the micro-pulse temporal profile displays its spiky structure.

5.6.2 Spikes

It has been stressed that the FEL radiation originates from the spontaneous emission and hence inherits its noisy structure. The distribution of particles inside the bunch is not homogeneous because of the granularity and this affects the first spontaneous emitted micro pulse. The radiation is composed of spikes having different peak powers. The duration of spikes is very close to the “slippage” distance along the optical klystron. The optical cavity stores the fundamental micro pulses and their spiky profile is amplified during successive interactions with the electron beam. Indeed, the spikes with initially larger peak power grow much faster than others because the amplification process is strongly

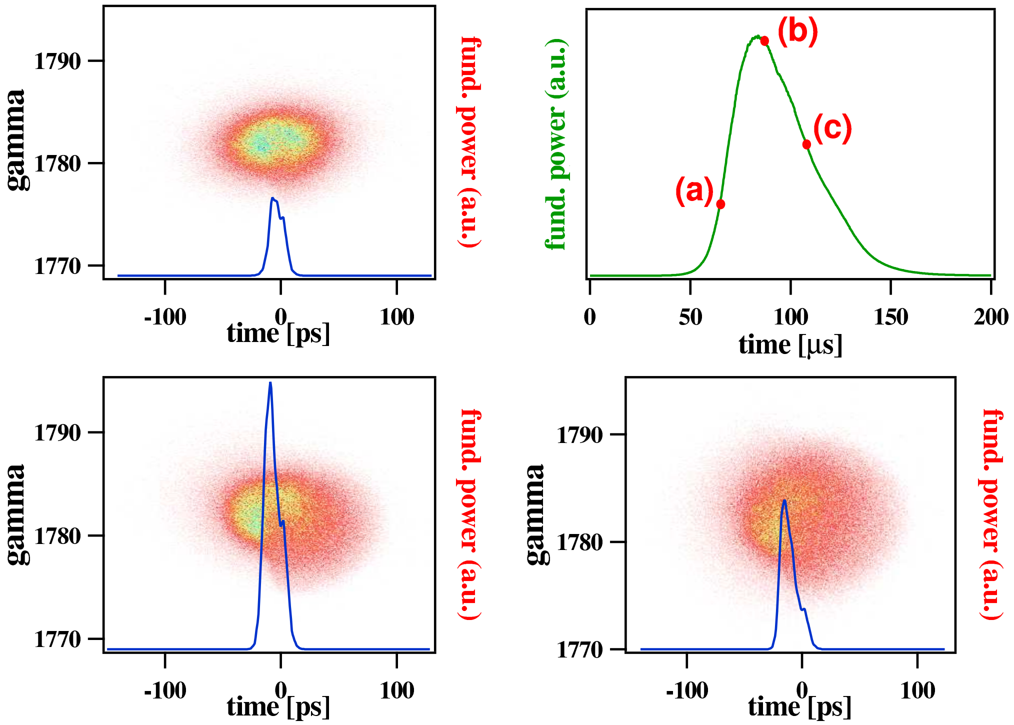

Figure 5.26: *Simulation of Elettra SRFEL: phase space during the giant pulse evolution.*

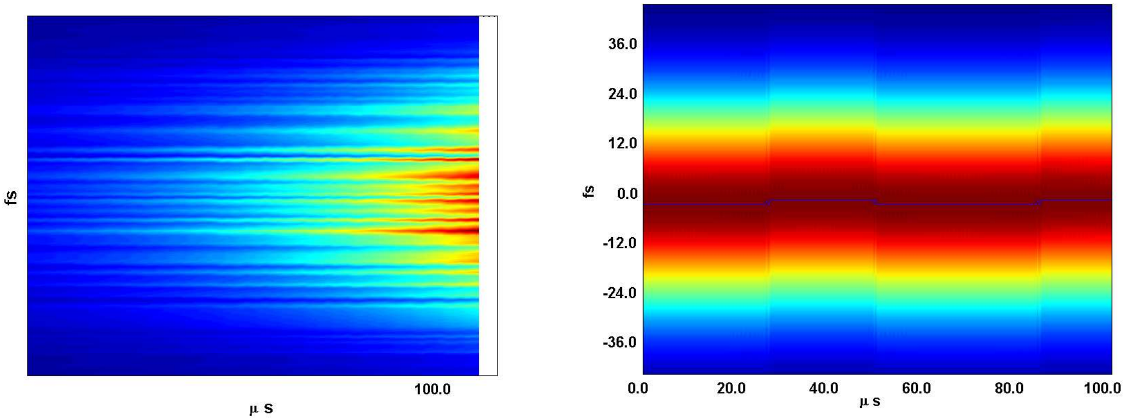

Figure 5.27: *Simulation of Elettra giant-pulse regime. At left: pseudo streak camera image of the fundamental pulse at the beginning of the giant pulse. At right: pseudo streak camera image of the electron beam. With respect to the experimental streak camera images the axes are swapped.*

nonlinear. As a result, at saturation few isolated spikes will contain the whole emitted power and also the harmonic micro pulses display the same temporal structure. This prediction has been demonstrated by simulation and confirmed by experiments carried at Duke SRFEL. In Fig. 5.28(a) we show a fundamental micro pulse near the saturation: it is clearly visible that few spikes contain most of its energy. Figure 5.28(b) is a pseudo-streak camera image of the third harmonic radiation, corresponding to the central part of the giant pulse. The slope in the pulse evolution is due to a slight temporal detuning between the FEL pulse and the electron beam at each pass through the optical klystron. In both cases, the simulations predict a much finer structure (hundreds of femtoseconds) than the resolution of available streak cameras.

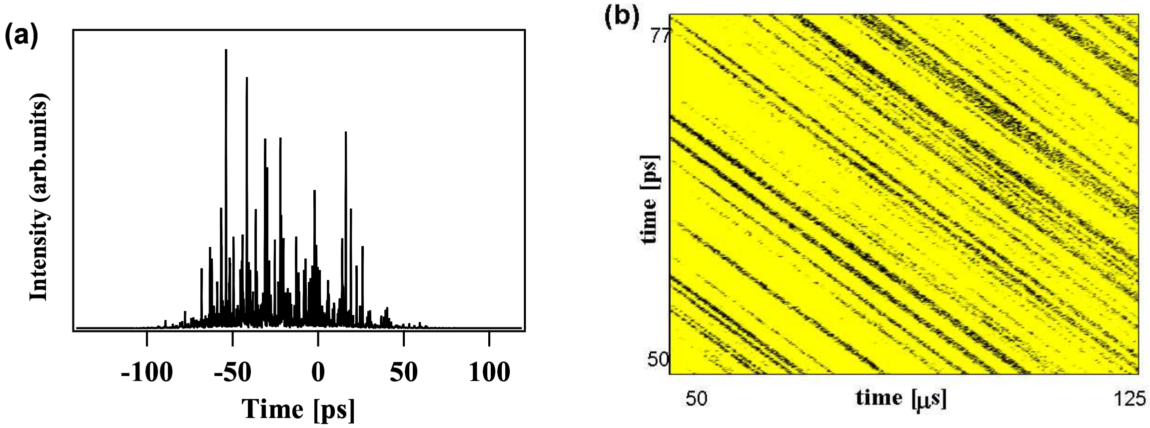

Figure 5.28: *Simulation of Duke giant pulse: micro-pulse temporal profile and pseudo-streak camera image of giant pulse.*

The code that we have developed allows to follow the evolution of the electron beam in terms of longitudinal and transverse dynamics. The evolution of the bunch length is shown in Fig. 5.29 by means of a pseudo streak camera image. After few tens of μs, starting to the giant pulse onset, the image displays the bunch lengthening. At the same time, also the energy spread starts to grow.

The experimental results and the numerical simulations for both the Elettra and the Duke SRFELs have been collected in a joint paper accepted by Phys.Rev.Lett. for publication (January 08).

5.7 Elettra SRFEL performance

In Table 5.2 are reported the oscillator configuration performance in free running and in Q-switch regime. The covered spectral range is from visible to about 170 nm.

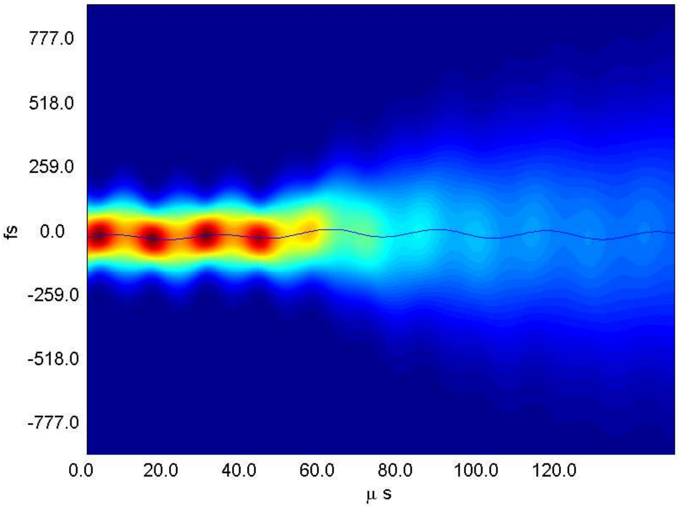

Figure 5.29: *Simulation of Duke giant pulse: pseudo-streak camera image of the electron beam where is visible the bunch lengthening.*

	NATURAL MODE	Q-SWITCH MODE
Relative spectral width ($\Delta\lambda/\lambda$)	$\sim 2 \cdot 10^{-4}$	$\sim 10^{-3}$
Repetition rate	4.63 MHz	10–20 Hz
Macro-temporal structure (ms-timescale)	aperiodic – quasi “CW”	–
Micro-pulse duration	~10 ps (FWHM)	~10 ps (FWHM)
Macro-pulse duration	–	~10μs
Average power (aperiodic structure)	few mW - 500 mW	–
Peak power	2 kW	30 kW
Photons/pulse	$5 \cdot 10^7$ @ 180 nm $2.5 \cdot 10^7$ @ 360 nm	$7.5 \cdot 10^8$ @ 180 nm $3.8 \cdot 10^8$ @ 360 nm

Table 5.2: *Oscillator configuration performance.*

5.7.1 Power estimations

Emission at fundamental wavelength

A direct measure of the micro-pulse peak power is impossible because the lack of instruments with the temporal resolution required for this case. Nevertheless, this value can be evaluated from the macro-pulse energy by applying some simple considerations. The measured macro-pulse energy outside the cavity at the fundamental wavelength is 5.2 mJ at 660 nm. Considering a mean macro-pulse duration of 130μs and the inter-bunch period (216 ns), the number of micro pulses in a macro pulse is about 600. The micro-pulse duration has been experimentally determined by streak camera measurements and it is typically 10 ps (FWHM). The peak power of the micro pulse can be simply calculated:

$$\frac{5.2\,mJ}{600 \cdot 10\,ps} = 870\,kW. \tag{5.2}$$

Here we have assumed that all micro pulses contained in a single macro pulse have the same intensity. This is equivalent to consider a rectangular macro pulse with a length equal to the FWHM of the experimental profile.

However, from the simulation results, we are allowed to re-calculate the peak power considering the spikes inside each micro pulse. Assuming that the power of each micro pulse is carried by 5 spikes with duration of about 750 fs, the peak power of the fundamental wavelength is about 2 MW.

Third harmonic radiation

For the harmonic the estimation of the peak power is based on the comparison with the spontaneous emission of the optical klystron at the same wavelength. In this case, at 220 nm, the measured power is 250 nW and then the energy carried by a spontaneous micro pulse is 250 nW×216 ns=$5.4 \cdot 10^{-14}$J. Considering a factor 25 (that is found from measurements) between the harmonic and the spontaneous signal, the energy carried by the coherent micro pulse at 220 nm is

$$\frac{25}{0.15 \cdot 0.07} \cdot 5.4 \cdot 10^{-14} \simeq 1.3 \cdot 10^{-10} J \tag{5.3}$$

where 0.15 is an estimation of the loss factor due to the interferential filter (see setup) and 0.07 is a factor that takes into account the contributions of the monochromator (essentially, two mirrors plus the grating), the CaF2 view-port and the cavity mirror. Assuming that the duration is 3 ps, the calculation of the peak power gives:

$$\frac{1.3 \cdot 10^{-10} J}{\sqrt{2\pi} \cdot 3\,ps} \simeq 17\,W. \tag{5.4}$$

However, considering the spikes, the peak power becomes one order of magnitude bigger:

$$\frac{1.3 \cdot 10^{-10} J}{\sqrt{2\pi} \cdot 250\,fs} \simeq 200\,W. \tag{5.5}$$

The latter value could be interesting for applications of the harmonic radiation in user experiments.

Bibliography

[1] V. N. Litvinenko, *Nucl. Instrum. Methods Phys. Res. A* **507**, 265 (2003)

[2] V. N. Litvinenko *et al.*, *Nucl. Instrum. Methods Phys. Res. A* **375**, 46 (1996)

[3] I. V. Pinayev, *et al.*, *Nucl. Instr. and Meth. A* **475** 222 (2001)

[4] T. Hara, *et al.*, *Nucl. Instr. and Meth. A* **431** 21 (1994)

[5] G. De Ninno,*et al.*, *Nucl. Instr. and Meth. A* **528** 278-282 (2004)

[6] I. Pinayev *et al.*, *Nucl. Instrum. Methods Phys. Res. A* **528**, 283 (2004)

[7] R. Bonifacio, L. De Salvo and P. Pierini, *Nucl. Instr. and Meth. A* **293** 627 (1990)

[8] M. Ferianis, "The Elettra Streak Camera: system set-up and first results", *Proc. of the DIPAC 1999 Conf., Chester, UK*

[9] W. Fawley, Report No. LBNL-49625, LBL, 2002

[10] http://pbpl.physics.ucla.edu/ reiche/

[11] H. P. Freund *et al.*, *IEEE J. Quantum Electron.* **36**, 275 (2000); H. P. Freund, *Phys. Rev. ST Accel. Beams* **8**, 110701 (2005)

[12] W. Fawley, Report LBNL-LCLS, To be published

[13] V. N. Litvinenko, *Nucl. Instrum. Methods Phys. Res. A* **358**, 369 (1995)

Chapter 6

Generation of Coherent Harmonics in “single-pass” configuration

In this chapter we present the results about harmonic generation obtained in single pass configuration. We give a complete characterization of the coherent harmonic radiation generated making use of the seeding technique. Detailed simulations have been carried out using the tri-dimensional code GENESIS. The expected performance is compared with the obtained experimental results.

6.1 Layout and GENESIS simulations

The implementation of the seeded “single-pass” configuration on the Elettra SRFEL is motived by the possibility to realize the Coherent Harmonic Generation (CHG) on an existing device (the Elettra optical klystron) and to test in advance the some of diagnostics and synchronization features of future linac based facility, i.e. FERMI@Elettra project.
Part of the project has been supported by the EUROFEL Design Study, an European contract involving various laboratories to prepare the construction of the next generation FEL light sources for short-wavelength radiation.
In particular, the TASK4 of EUROFEL has as the aim of to find answers and to test techniques essential for the design of the seeded harmonic generation of the new VUV-X-ray FELs in Europe. The issues are important for increasing the stability, the coherence and the wavelength range of these devices.
In this framework, we have exploit the possibility to implement single-pass FELs in a storage ring and to evaluate differencies and possible advantages. Our work has contributions both in theoretical investigations and experimental tests with an available infrastructure.

The setup of the Elettra SRFEL has been modified in order to seed the electron beam with an external laser (Ti:Sapphire). The two cavity mirrors have been removed and the seed laser is injected into the first undulator from the back–end of the SRFEL beamline. A schematic picture of the layout is shown in Fig. 6.1. For other details, see also Ch. 4. The experiment has been divided in to stages. During the first part, we have used the full power at the fundamental wavelength of the laser in order to optimize the setup and demonstrate the feasibility of the harmonic generation in the Elettra SR. Then we have used the second harmonic of the seed laser to produce coherent harmonic radiation down to 100 nm. As a consequence of the positive results obtained by these experiments, a new project (EUFOS) has started at Elettra with the aim of seed the electron beam with the third harmonic of the Ti:Sapphire laser. The resulting harmonic radiation, at 80 nm and even shorter wavelengths, will be also employed for user experiments.

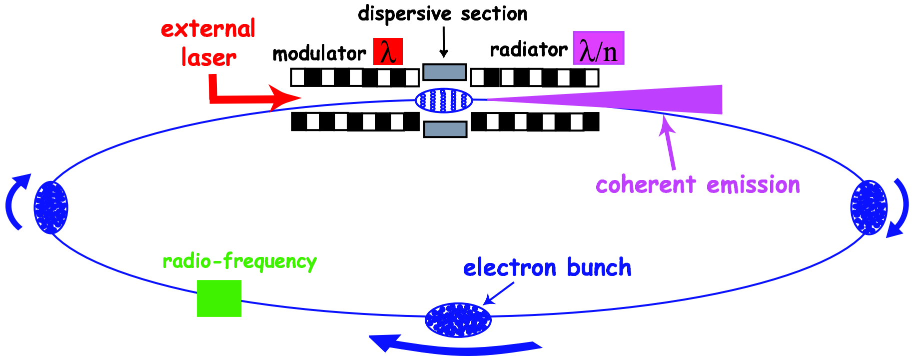

Figure 6.1: *Seeded "single-pass" configuration layout.*

An external Ti:Sapphire laser delivers an optical pulse having a short duration (100 fs–1 ps) and a high peak power (order of several GW). The laser pulse is synchronized with the electron bunch. The first undulator is tuned at the seed wavelength and the dispersion section strength is optimized to maximize the electron-bunch harmonic content (micro-bunching) at the entrance of the radiator. The radiator is tuned at one of the harmonics of the seeding signal.

In the first experiment the power of the seed laser at the fundamental wavelength (780 nm) could be set up to 25 GW with a pulse length close to 100 fs (FWHM). The implementation of synchronization schemes allows to guarantee an electron-photon overlap within the undulators. It has been also possible to optimize the transverse overlap between the two beams by means of two remotely controlled steering mirrors.

In the second stage, the second harmonic of the Ti:Sapphire laser has been obtained by means of a β-barium-borate (BBO) crystal. The efficiency of the frequency doubling is of the order of 28%. The peak power at 390 nm is about 5.4 GW with pulse length of about 130 fs (FWHM). Although the peak power is much less with respect to 780 nm, at shorter wavelength the the actual dimension of the laser spot in the undulator is about a factor two smaller. The beam size has been measured in the laboratory at the same distance from the lens. The estimation of the beam waist inside the undulator is 2.0 mm at 780 nm and 1.2 mm at 390 nm.

Before experimental implementation, such a configuration has been simulated using the tri-dimensional code GENESIS [1]. The parameters used during the simulations are shown in Table 6.1. GENESIS is a numerical tool able to simulate the Free Electron Laser process inside an undulator or a chain of those. The electron beam is represented by macroparticles that are propagate in a 6D phase space (x, y, z, p_x, p_y, p_z) and contain all the characteristics of the beam (energy, emittance, energy-spread, bunch-length, and so on). There is also the possibility to run simulation both in time-dependent and time-independent mode.

Energy	0.75 – 1.5 GeV
Current range	0.5–6 mA
Emittance RMS at 0.9 GeV	1.53 nm rad
Natural RMS energy-spread	0.036% at 0.9 GeV 0.03% at 0.75 GeV 0.06% at 1.5 GeV
Natural RMS bunch length	5.4 ps at 0.9 GeV 4.1 ps at 0.75 GeV 11.6 ps at 1.5 GeV
RMS energy-spread at 6 mA	0.12% at 0.9 GeV 0.23% at 0.75 GeV 0.08% at 1.5 GeV
RMS bunch length at 6 mA	27 ps at 0.9 GeV 28 ps at 0.75 GeV 27 ps at 1.5 GeV

Table 6.1: *Elettra parameters used in* GENESIS *calculations.*

6.1.1 Preliminary calculations

The Elettra SRFEL can operate between 0.75 and 1.5 GeV. The lower limit is due to machine limitations (magnets' power supplies at lower operational limit) while the upper limit has been set considering the effect of the undulator radiation on the last CaF2 window (see Ch. 4) and the possibility to tune the first undulator at the seed fundamental wavelength. A preliminary set of simulations has been dedicated to determine the optimum energy. We have simulated three different energies (i.e., 0.75, 0.9 and 1.5 GeV). For this first set of simulations, the seed wavelength is 240 nm, because we suppose to use the third harmonic of the Ti:Sapphire laser. In Fig. 6.2 the peak power emitted at the end of the radiator at the third harmonic (80 nm) is plotted versus the seed power for the envisaged energies.

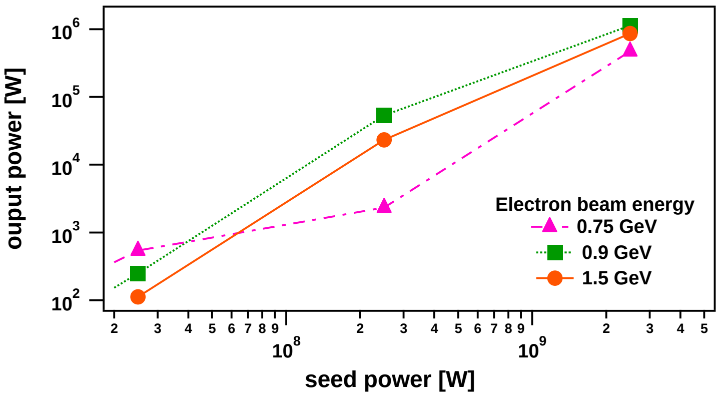

Figure 6.2: *Output power at 80 nm as a function of the seed peak power for three different energies.*

When the seed power is low (10^7 W), the induced energy spread is low and the effect of the initial energy spread is important (see Ch. 3). As a consequence, the maximum power is obtained at 0.75 GeV which has the smaller initial energy spread. On the other hand, for higher seed powers (about 1 GW), the energy modulation induced by the seed laser is dominant in the bunching process, so that there is a small difference from one energy to the other.

In the following we have preferred to use 0.9 GeV because, besides the slight higher output power, at this energy the modulator gaps can be closed in order to be resonant with the wavelength of the seed laser. Lower energies would request closer gaps, smaller than the vacuum pipe.

We also studied the dependence of the output power on the dispersive section strength. According to simulation, in the ideal conditions (perfect temporal and spatial overlap) the maximum available seed power is enough to produce the maximum micro-bunching and the magnetic field of the dispersive section can be set to zero. It will be shown later that the experimental conditions require a dispersive section quite strong. In Fig. 6.3 we report some results regarding the dependence of the output power and the bunching with respect to R_{56}. The first plot shows that the seed power is enough to induce the required energy spread and a stronger dispersive section degrades the performance. The second plot provides an estimation of the bunching and the third plot confirm that the maximum power can be obtained with the minimum R_{56}.

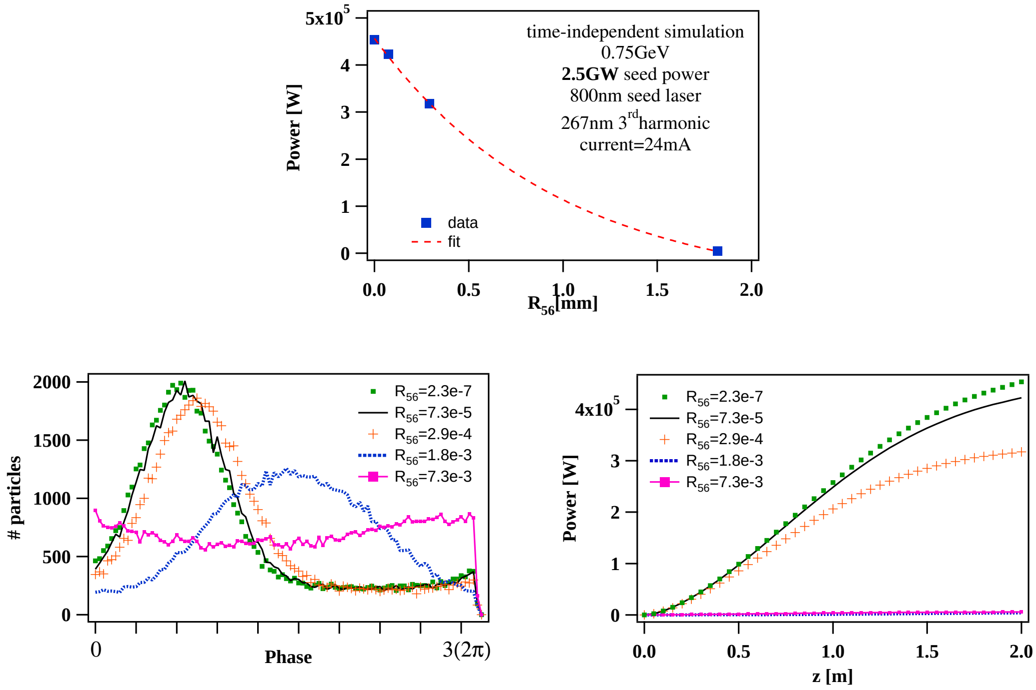

Figure 6.3: *Top: third harmonic power as function of the dispersive section strength. Bottom left: particle distribution in phase for different values of* R_{56}*. Bottom right: third harmonic output power along the radiator for* R_{56} *values of previous plot.*

Expected performance

We want to simulate the best case that we expect to be able to implement experimentally. The simulation has been performed using GENESIS in time-dependent mode. The seed laser is set to 240 nm and the modulator is tuned at the same wavelength. The radiator is tuned at 80 nm (the third harmonic). We assume for the seed laser a Gaussian profile, with peak power of 2.5 GW and full width at half maximum (FWHM) duration of 100 fs. Besides, the waist of the optical field is placed at the entrance of the first undulator. The electron beam energy is 0.9 GeV, the peak current is 77 A, the bunch length is 25 ps (root mean square (RMS)) and the relative energy-spread is about 10^{-3}. The evolution of the harmonic radiation along the second undulator is shown in Fig. 6.4a. The output power is about 1 MW. Figure 6.4b shows the electron beam phase space (γ, θ) at the modulator exit. The distribution displays an already enhanced energy modulation, that requires only a short drift to be converted in spatial separation (bunching). Applying even a little magnetic field, the electrons distribution goes in overbunching and the output power gets worse. In Figs. 6.4c-d, the spectrum and the temporal profile of the third harmonic signal at the radiator exit are reported. The relative spectral width is about $1.7 \cdot 10^{-3}$ (FWHM) and the pulse duration is about 72 fs (FWHM). This means that the radiation is really close to Fourier limit (see Eq. 7.8 in Sec.7.3).

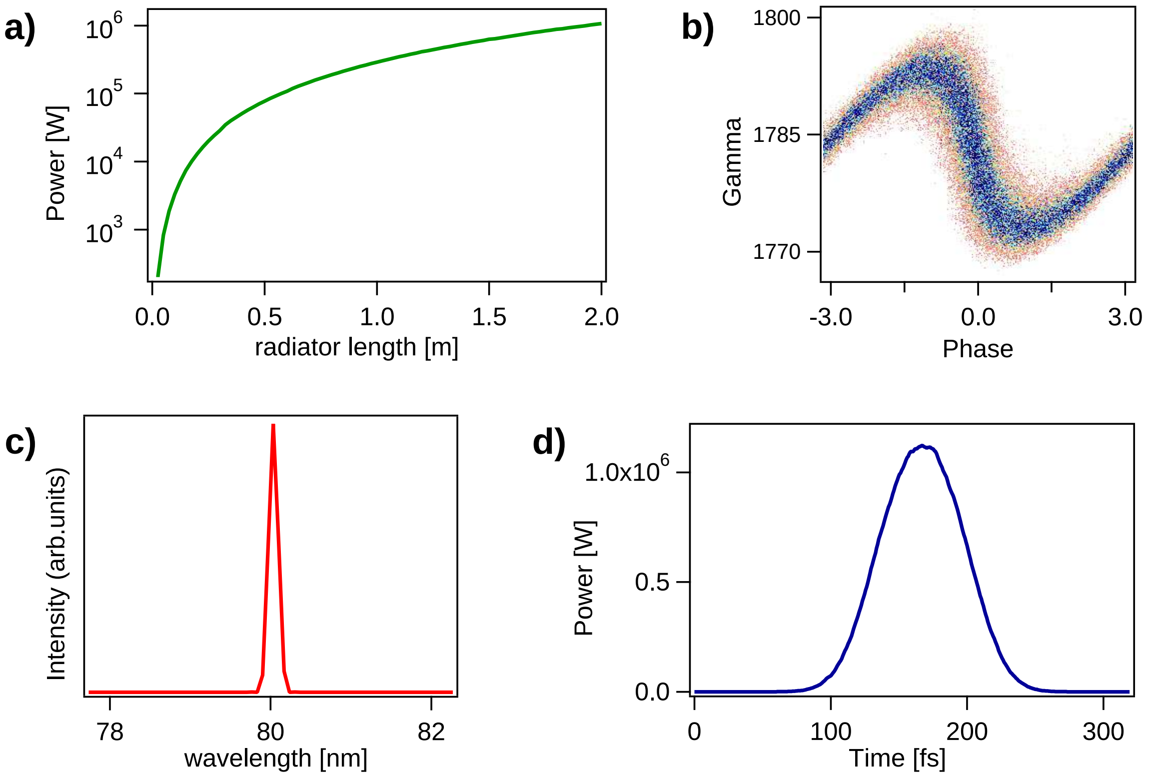

Figure 6.4: *Expected performance of the Elettra SRFEL from* GENESIS *calculation. a) output power along the radiator at 80 nm, b) phase space at the end of the modulator, c) spectrum of the harmonic signal, d) temporal profile of the harmonic signal.*

Comparison between 240 nm and 800 nm seed

The preliminary results of simulations are really promising for the future of this facility. However, using the third harmonic of the Ti:Sapphire laser as a seed, the resulting coherent harmonic radiation is below the threshold of air absorption. As a consequence, the transport of the harmonic radiation to diagnostics and/or experimental stations would require a high vacuum beamline coupled to dedicated diagnostics. Therefore, in order to demonstrate the feasibility of the experiment, as a first step we decided to use as a seed the fundamental of the Ti:Sapphire. Before the duplication, the laser power is obviously greater and this can help the detection of the signal. Using the infrared radiation as seed, one can realize the diagnostics in air both for the third (267 nm) and the fourth harmonics. We have also to take into account the CaF2 window at the end of the vacuum chamber (see layout in Ch. 4), that allows the transmission of radiation up to the sixth harmonic (133 nm). On the basis of these considerations, we started to simulate a configuration with seed wavelength=800 nm and electron beam energy=0.9 GeV. The total current that in principle can be stored in single bunch at Elettra is about 6 mA. Considering a bunch length of 24 ps (from previous measurements [2]), the peak current is accordingly 22 A. Since we have to take into account optics absorption, we set the seed laser peak power at 10 GW, namely 2.5 times lower the value obtained considering the nominal energy (2.5 mJ) and the nominal pulse length (100 fs) at the fundamental wavelength. Also, we considered a slightly longer pulse, i.e., 150 fs. We tune the radiator at the third harmonic (266.67 nm) and in 2 m the output power reaches 0.9 MW. Being demonstrated, in previous runs, that the peak power is basically the same in both time-independent and time-dependent simulations, the following results has been obtained in time-independent mode that is less time consuming. Considering the physical device (optical klystron plus vacuum chamber), we need to operate at 0.75 GeV, where the machine is less stable, since at 0.9 GeV the modulator can not be tune at 800 nm. There is actually a lower limit (19 mm) in the undulator gaps which is set by the beam pipe vertical dimension. Besides the instability, at 0.75 GeV the percent energy spread is about a factor two than the one at 0.9 GeV.

The other parameter that can be varied is the seed pulse length. As explained in Ch.4, there is the possibility to switch from 100 fs to 1 ps preserving the transform limit relation between the pulse duration and the spectral width. A comparison of the electron beam distribution at the modulator exit between the 100 fs and the 1 ps case is shown in Figs. 6.5a-b. The seed peak power is 5 GW in both cases. The resulting coherent radiation at the third harmonic for the 1 ps case, reported in Fig. 6.5c, has a lower peak power (one order of magnitude) with respect to the 100 fs case, but the pulse length is about 10 times longer and then the energy carried by the pulse is the same in both configurations. Similar results have been obtained at 0.9 GeV.

Further studies

In ideal conditions (perfect temporal and spatial overlap between the seed and the electron beam), the dispersive section can enhance the output harmonic radiation only if the energy modulation induced by the seed laser is below a given threshold. Otherwise, increasing the R_{56} parameter, one can observe a reduction of the power, as shown in Fig. 6.6.

The evolution of the bunching coefficients along the first undulator is shown in Fig. 6.7 for the fundamental, the third and the fifth harmonic. After 2 m (i.e., after 20 undulator periods) the fundamental bunching is close to saturation (0.6) and the bunching at the third harmonic is quite large (0.4). This is the reason why one can effectively produce coherent radiation at the third harmonic tuning the second undulator at this wavelength.

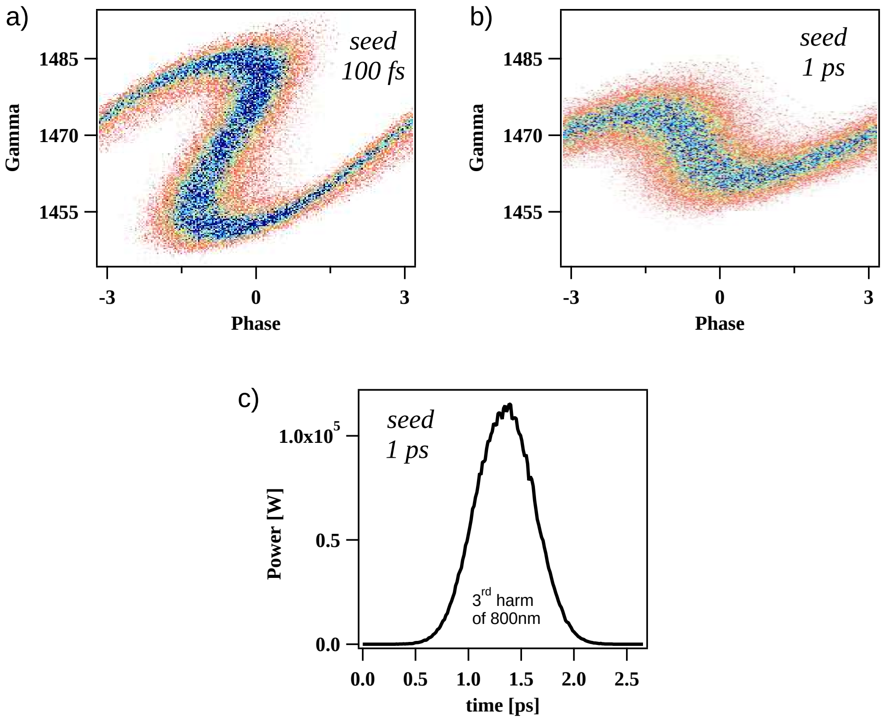

Figure 6.5: *Phase space at modulator exit for: a) 100 fs seed pulse length, b) 1 ps; c) temporal profile in the 1 ps case. Electron beam energy 0.75 GeV.*

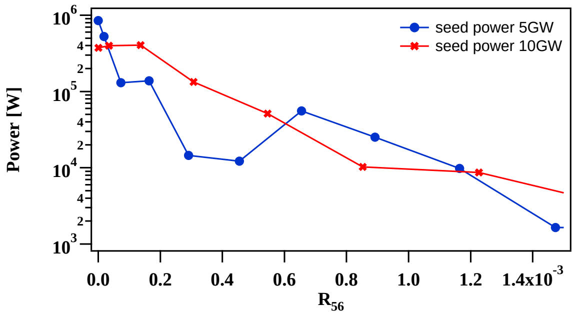

Figure 6.6: *Harmonic output power as function of the dispersive section strength R_{56} for two different peak powers of the seed laser.*

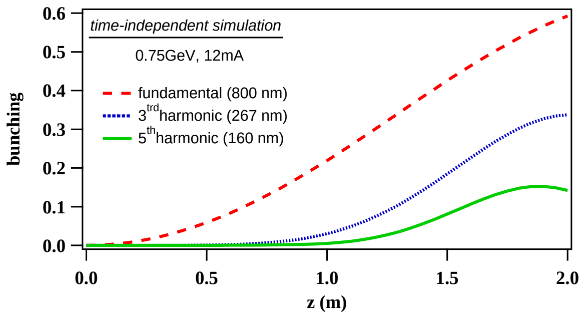

Figure 6.7: *Evolution of the bunching along the modulator for the fundamental, the third and the fifth harmonic wavelengths. Electron beam energy=0.75 GeV. Current=12 mA.*

The generation of harmonic radiation in seeded-FELs has a quadratic dependence on the bunch current whereas, for example, the synchrotron radiation displays a linear trend. In Figure 6.8 we report the results of three simulations performed at different currents.

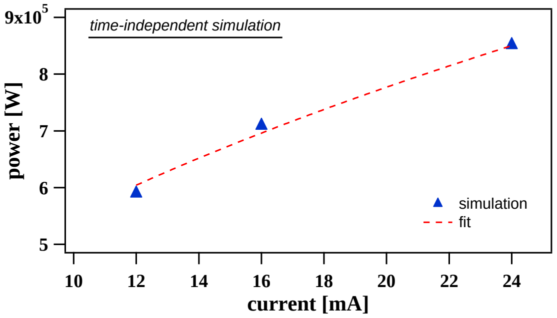

Figure 6.8: *Output power as function of the beam current.*

6.2 Experimental results

In this Section we present the experimental performance obtained in seeded configuration with the Elettra optical klystron. The layout of the diagnostics used to characterize the harmonic radiation in shown in Fig. 6.9. We make use of a monochromator coupled with a photomultiplier (PMT) and a charge-coupled device (CCD). The instrumentation details are described in Ch. 4.

6.2.1 Time resolved measurements

The coherent harmonic radiation is monochromatized and then acquired on a digital oscilloscope by means of a photomultiplier tube (PMT), which is fast enough to resolve the pulses dynamics of electron bunches photoemission (hundreds of nanoseconds) but does not allow to resolve the real photon pulse shape (tens of ps). In Fig. 6.10 (left), we report the first evidence of coherent harmonic radiation at the third harmonic of the seed laser. The enhanced peak is the coherent signal generated by the seeded electron

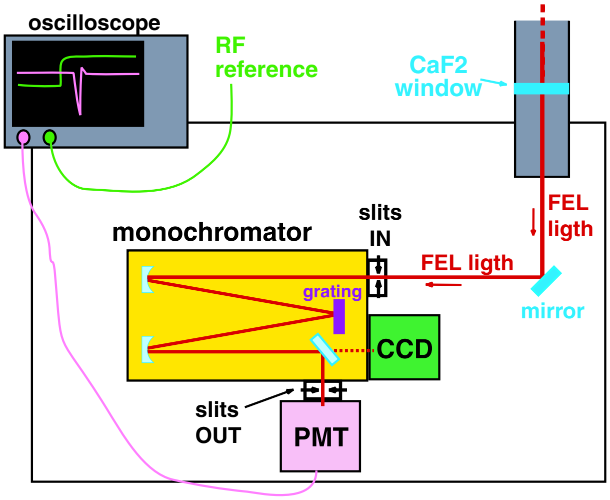

Figure 6.9: *Layout of the detection area.*

bunch, while the small side peaks represent the spontaneous (i.e., unseeded) radiation. The repetition rate of the seed laser and, as a consequence, of the coherent pulse is 1 kHz. For the reported experiment the seed power is of the order of 10 GW, the seed pulse length is about 100 fs and the electron beam energy is 0.75 GeV and the current (in single bunch) is about 2 mA. Optimizing the system, the harmonic signal grows with respect to the spontaneous emission, as shown in Fig. 6.10 (right). The seeded peak is about a factor 50 above the unseeded peaks (corresponding to synchrotron emission only). This factor becomes 10^4 if one takes into account the different pulse durations. In fact, the whole bunch, that is about 30 ps, contributes to the spontaneous emission, while in the case of the coherent harmonic signal, the seeded portion of the bunch is only about 100 fs.

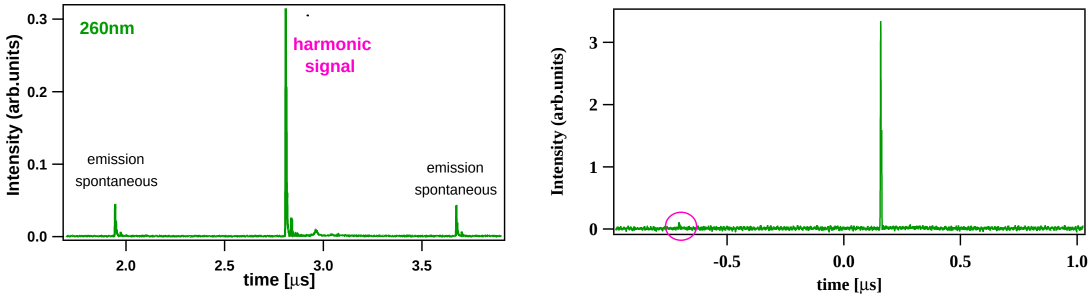

Figure 6.10: *Left: First evidence of coherent harmonic radiation at 260 nm (third harmonic of the seed wavelength). Integrated signal of the monochromatized radiation acquired with a photomultiplier tube plotted vs. the acquisition time. Right: coherent harmonic radiation at 260 nm after optimization.*

After the demonstration of generation of coherent signal at the third harmonic of the seed laser, a nonlinear BBO crystal has been used to obtain the second harmonic of the Ti:Sapphire. The peak power energy is reduced to 5.4 GW and the pulse length is increased to 130 fs. Using the seed laser at about 400 nm, the first undulator is tuned at the same wavelength. This allows to use higher beam energy (i.e., a more stable electron beam) since the corresponding undulator gaps are over the limit of the vacuum pipe. The harmonic radiation at 195 nm (the second harmonic of the seed) acquired by the PMT is shown in Fig. 6.11.

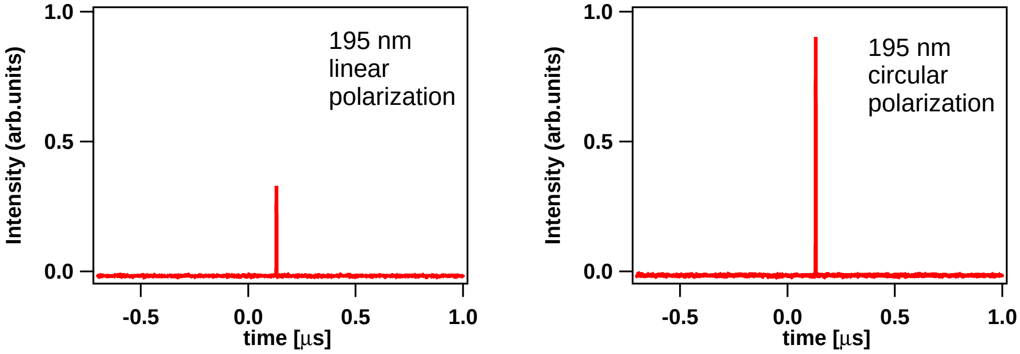

Figure 6.11: *Monochromatized harmonic radiation at 195 nm. At left linear polarization, at right circular polarization. The ratio between signals is about three.*

The quadratic dependence of the harmonic signal with respect to the beam current, which is the coherence signature, is shown in Fig. 6.12. We measured the intensity of the CHG acquired by the oscilloscope during a scan on the seed laser delay (in the reported case from -50 ps to +50 ps around the maximum). We assume that the seed pulse length is short enough to heat a portion of the bunch with uniform charge. Then we estimate the electrons participating at the process ("normalized charge density" on the picture) using streak camera images of the electron beam acquired simultaneously.

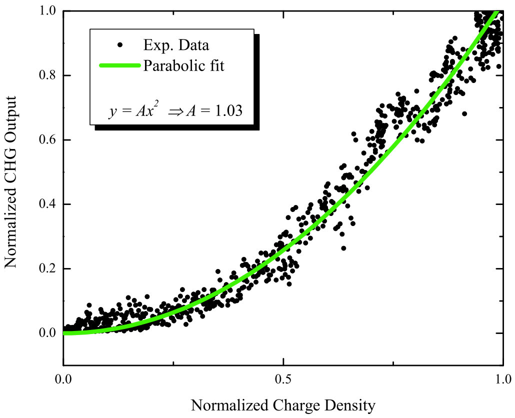

Figure 6.12: *CHG signal as a function of the electron beam charge. The quadratic behavior is the signature of coherence. Experimental conditions: energy=1.095 GeV, seed wavelength=398 nm, seed power=4-5 GW, seed duration=100 fs, repetition rate=1 kHz, linear polarization.*

The aim of this experiment is to produce a usable radiation with wavelength as short as possible. We will discuss later on the other requirements, such as stability and number of photons per pulse. To accomplish our goal, we implemented a nitrogen purged diagnostic to extend the wavelength range below 190 nm, where the power absorption due to oxygen becomes more and more important. The required optics has been put in a box filled with nitrogen flux. Some pictures are shown in Fig. 6.13.

Figure 6.13: *Pictures of the purging setup: a) end of the beam pipe, b) the box and the monochromator entrance, c) from top.*

The second undulator is tuned at the third harmonic of the seed laser. The obtained radiation at 130 nm, both in linear and circular polarization, is shown in Fig. 6.14.

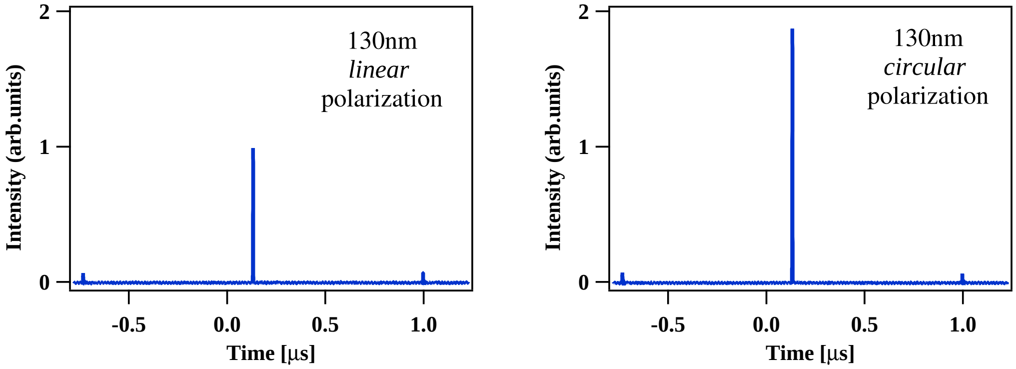

Figure 6.14: *Monochromatized harmonic radiation at 130 nm. At left linear polarization, at right circular polarization. The ratio between signals is about two.*

As mentioned in Ch. 4, the radiator can be tuned either in linear or in circular polarizations. When the undulator is set to produce circular polarization, the coupling between the field and the electron beam is strengthened and, as a consequence, the optical gain is enhanced. This explains why the signal in circular polarization is about a factor 3 (see Fig. 6.11) stronger than that generated using linear radiator.

Since the inter-bunch period is 864 ns, the electron bunch revolution frequency is about 1.16 MHz. As a consequence, the bunch is seeded (i.e., generates coherent harmonic emission) only once every about 1160 turns. Hence, the repetition rate of the spontaneous (incoherent) emission generated by the beam at every pass through the undulators is much higher than that of coherent emission. Spontaneous emission produces background noise, which may be a trouble when the light is to be exploited for user experiments. The problem can be solved by using a gated detector, as we will report in Ch. 7.

6.2.2 Spectral measurements

For spectral measurements, the main issue is the acquisition time, since, as already mentioned, 1 CHG pulse corresponds to about 1000 round trips of the electron beam. The acquisition time of the CCD coupled with the spectrometer is in the ms range. As a consequence, the reported spectra have been obtained removing the background of synchrotron radiation. The spectrum of the coherent signal at 260 nm, corresponding to Fig. 6.10, is shown in Fig. 6.15. The CHG signal is on the top on the spontaneous emission spectrum.

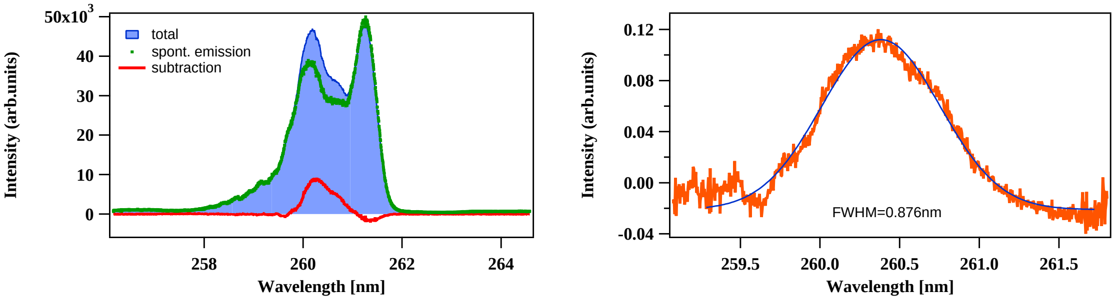

Figure 6.15: *Spectrum of coherent harmonic radiation at 260 nm (third harmonic of the seed wavelength). Left: total signal, spontaneous emission and the signal subtracted. Right: normalized signal after background subtraction.*

The spectra of the second (195 nm) and the third harmonics (130 nm) of the seed laser at 390 nm, after subtraction of the radiator spontaneous emission, are shown in Fig. 6.16. They exhibit a relative bandwidth of the order of 10^{-3}. Assuming a pulse length equal to the seed laser duration, the coherent harmonic signal is very close to Fourier limit.

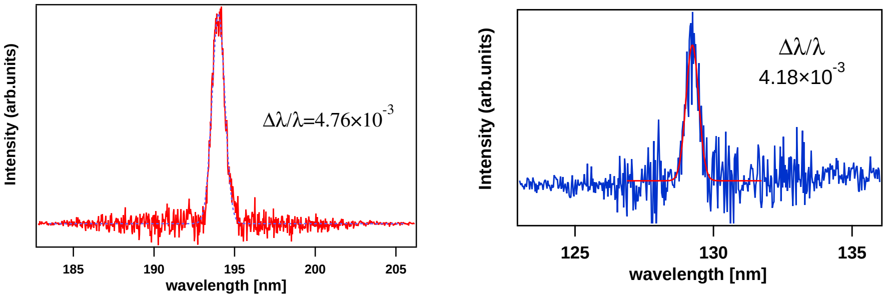

Figure 6.16: *Spectra of coherent harmonic radiation after background (spontaneous emission) subtraction: at left, 195 nm, at right, 130 nm.*

Figure 6.17 shows the spectral measurements of the coherent signal at 132 nm. The estimation of the spectral width gives a bandwidth, $\Delta\lambda$, of about 0.14 nm (RMS). Assuming Gaussian temporal and spectral profiles, at transform limit, one would get $\Delta t = 0.06 \cdot \lambda^2/(c \cdot \Delta\lambda) \simeq 33\,\mathrm{fs}$ (RMS) which is about a factor two larger than the value predicted by GENESIS calculation.

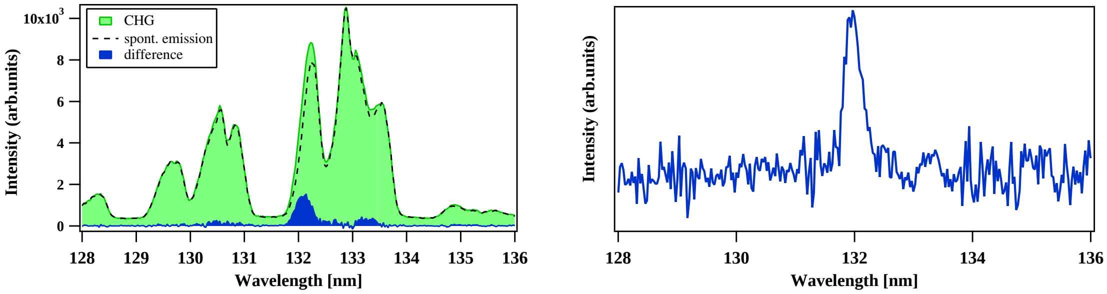

Figure 6.17: *CHG spectra at 130 nm. Left: total signal, spontaneous emission background and difference of spectra. Right: normalized signal after background subtraction.*

6.2.3 Electron beam characterization during CHG

During the generation of coherent harmonics, we investigated the influence of this process on the electron beam dynamics using the streak camera. We perform several sets of measurements in different conditions (changing, e.g., the beam energy, the stored current and the seed laser wavelength) The main difference has been observed between the lowest energy (0.75 GeV) and the highest energy (1.095 GeV) used during this experiment.

0.75 GeV case

The images in Fig. 6.18 (top) refer to unseeded condition. Performing an horizontal cut on the streak-camera image, it is possible to follow the evolution of the intensity. It is visible from the analysis that the electron beam displays a periodic instability with frequency of about 50 Hz. During CHG we acquired the picture in Fig. 6.18 (bottom left) and one can observe a lengthening of the bunch. The electron beam appears still instable (see Fig. 6.18 (bottom right)).

The comparison of seeded/unseeded bunch-length evolution is shown in Fig. 6.19. Before CHG, the bunch profile is almost Gaussian, while during CHG the distribution becomes flatter. The evolution of the RMS bunch duration show a lengthening during CHG of about 20%.

1.095 GeV case

The situation is different at 1.095 GeV. We expected an effect but we do not find any significant bunch lengthening. This is probably due to shorter damping time of synchrotron oscillations at higher energy (40 ms at 1.095 GeV vs. 130 ms at 0.75 GeV) and also to the larger energy spread. Figure 6.20 shows streak camera images and their analysis related to unseeded condition and during CHG.

Figure 6.21 shows the profiles of electron beam distribution related to seeded and unseeded conditions. Contrary to 0.75 GeV case, the distribution shape is Gaussian in both conditions. The evolution of the RMS bunch length has a similar (noisy) behavior during CHG and in the unseeded case.

We also analyzed the higher order moments of the electrons distribution. Preliminary results show that the Gaussian shape becomes more flat during the generation of coherent harmonic.

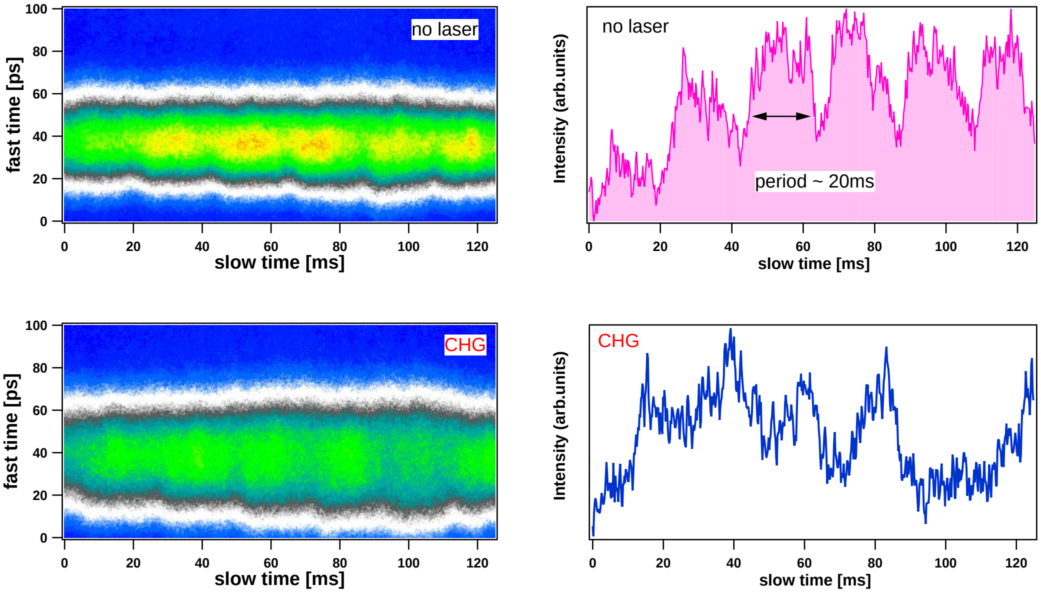

Figure 6.18: *Streak camera images at 0.75 GeV. Top left: streak camera image related to unseeded condition. Top right: evolution of the intensity obtained performing a horizontal cut on the image at left. The electron beam displays a periodic instability at 20 ms. Bottom left: streak camera image acquired during CHG process. Bottom right: evolution of the intensity obtained performing a horizontal cut on the image at left. The beam is still instable. Experimental conditions: seed laser wavelength 780 nm, peak power 10 GW, pulse length 100 fs, repetition rate 1 kHz. We acknowledge Hamamatsu company to allow the use of the streak camera for this measurements.*

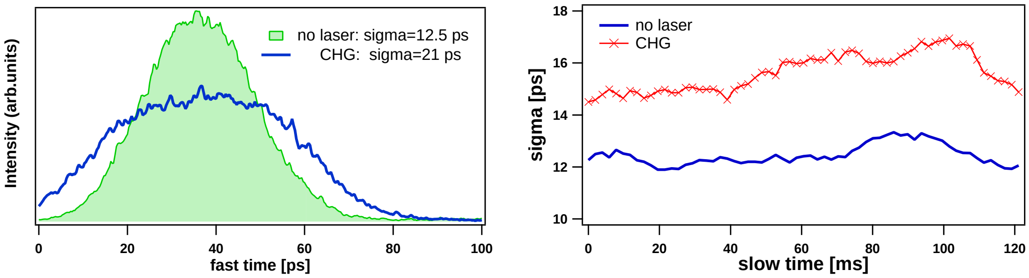

Figure 6.19: *Left: bunch-length measurements obtained performing a vertical cut on images in Fig. 6.18. Right: bunch-length evolution of images in Fig. 6.18. Experimental conditions: seed laser wavelength 780 nm, peak power 10 GW, pulse length 100 fs, repetition rate 1 kH.*

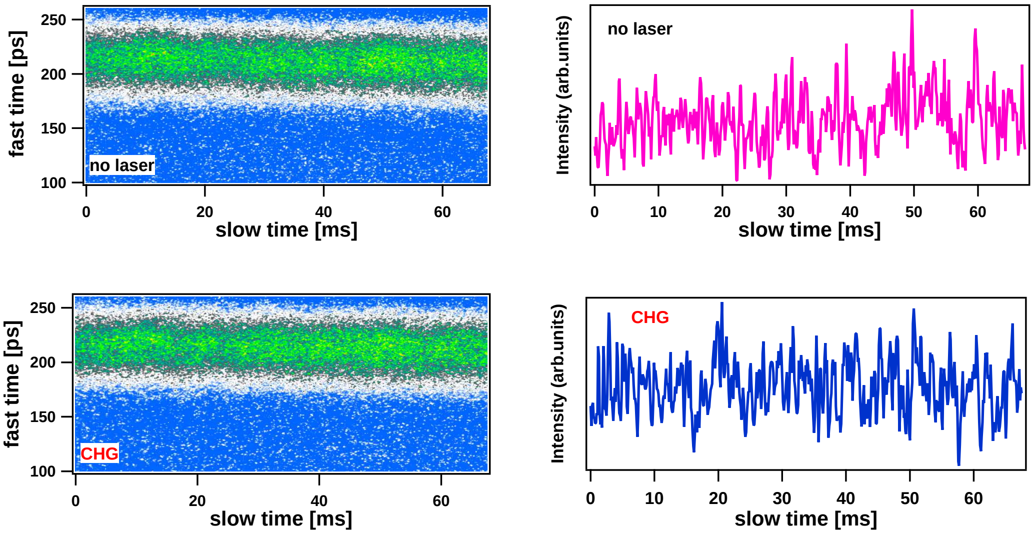

Figure 6.20: *Streak camera images at 1.095 GeV. Top left: streak camera image related to unseeded condition. Top right: evolution of the intensity related to unseeded condition. Bottom left: streak camera image acquired during CHG. Bottom right: evolution of the intensity during CHG. Experimental conditions: seed laser wavelength 390 nm, peak power 3 GW, pulse length 120 fs, repetition rate 1 kHz.*

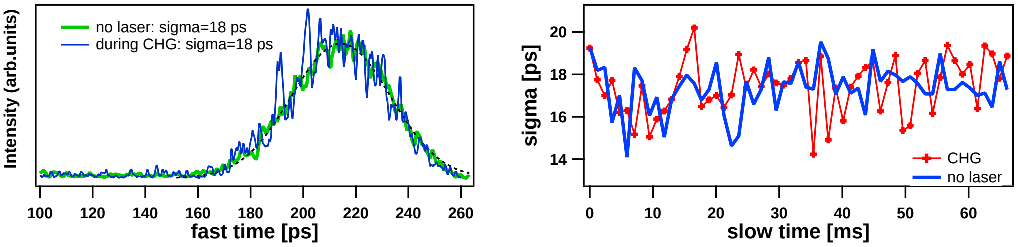

Figure 6.21: *Left: bunch-length measurements at 1.095 GeV. Right: bunch-length evolution related to streak camera images in Fig. 6.20. Experimental conditions: seed laser wavelength 390 nm, peak power 3 GW, pulse length 120 fs, repetition rate 1 kHz.*

Besides, 1 ps has not been tested yet and we will use a code that take into account the recirculation of the beam, because we expected the CHG works better at 100 Hz then 1 kHz.

This preliminary studies indicate that, at 1.095 GeV, the energy spread does not probably grow significantly during CHG. As a consequence, working with a seed pulse of 100 fs, there would be not a big gain at repetition rate lower than 1 kHz. Using a longer seed pulse (1 ps) instead, the CHG should profit from a lower repetition rate. This is also true if the initial energy spread is smaller. For this purpose, we have recently measured during CHG shifts the energy spread at 1.095 GeV, as shown in Fig. 6.22.

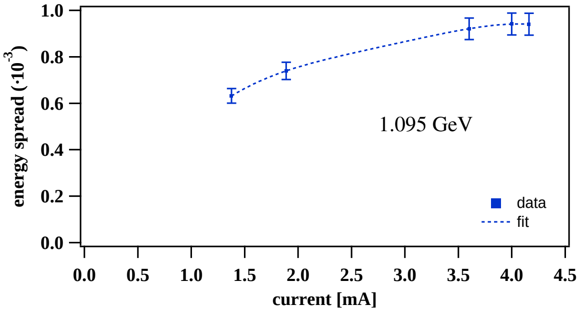

Figure 6.22: *Energy spread measurement at 1.095 GeV.*

6.2.4 Characterization of the source

Temporal stability

A fundamental feature of a light source to be exploited for user experiments is the shot-to-shot stability of the emitted power. Data displayed in Fig. 6.23 shows a sequence of 500 consecutive coherent pulses acquired by the PMT. The analysis of this sequence show that the fluctuation is about 14% and the spectrum displays strong components at 50 Hz and 100 Hz, indicating an instability of the electron beam. In this case, the reproducibility of our source is comparable to the synchrotron radiation.

Nevertheless, in other cases, a very good stability is found with fluctuations of the order of few percent, as shown in Fig. 6.24. This is mainly due to the very good electron-beam stability, which is a common characteristic of all modern storage rings. An important role is also played by the low seed-electron timing jitter, which is about 2 ps in our case. Such a value is enough to guarantee that, during consecutive shots, the laser “seeds” bunch portions containing very similar numbers of electrons. As for longer terms reproducibility, for relatively low current values ($\leq$1 mA), i.e. a relatively long beam lifetime, we observed a very stable behavior over several hours.

Power vs. seed laser

Figure 6.25 shows the dependence of the harmonic power on the seed power. It is clear from the plot that the relation is not linear and we tried to fit the data with a polynomial function. The output power scales with the bunching squared.

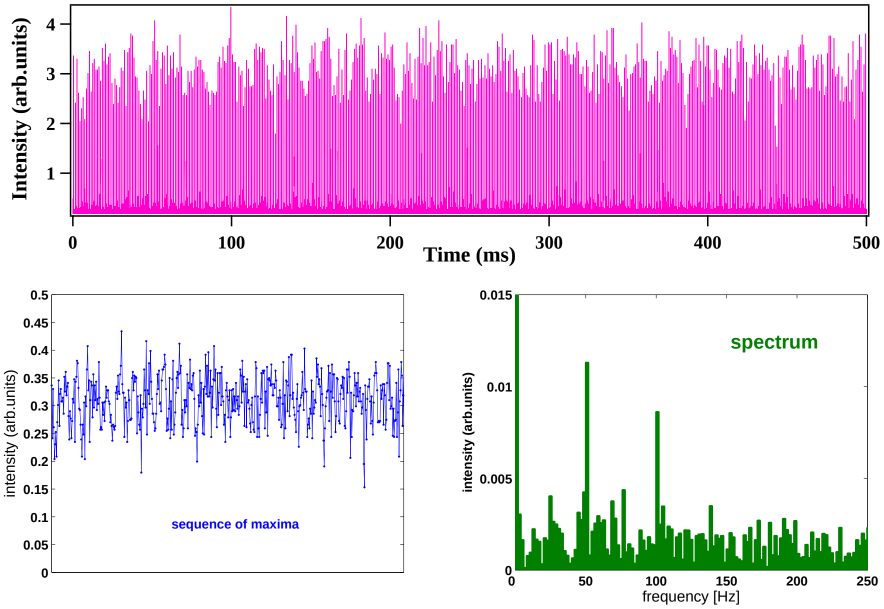

Figure 6.23: *Top: sequence of 500 pulses acquired by PMT. Bottom: analysis of the sequence: at left, the sequence of maxima (fluctuation 14%); at right, the spectrum of the sequence of maxima.*

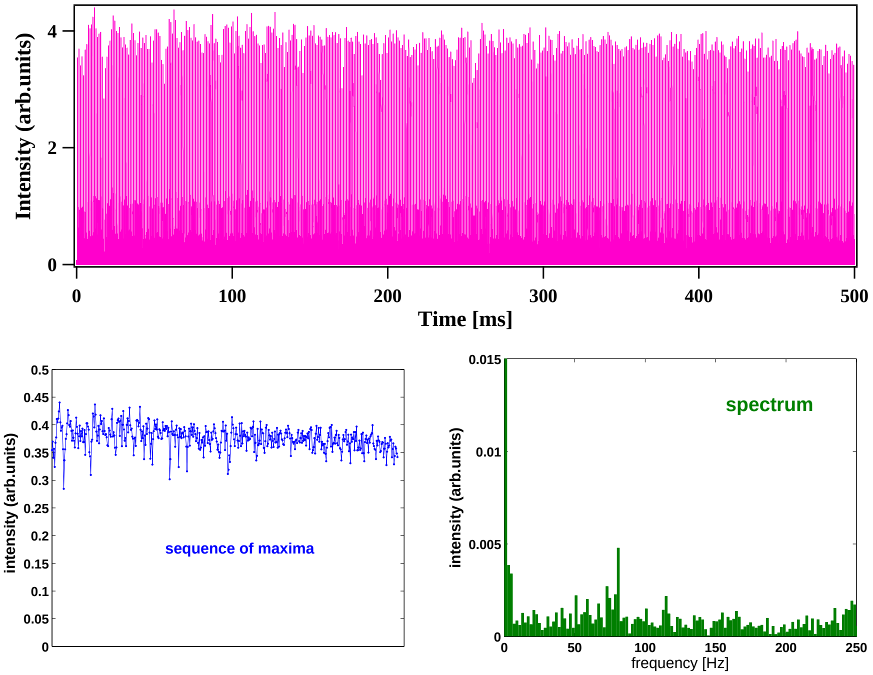

Figure 6.24: *Top: sequence of 500 pulses acquired by PMT. Bottom: analysis of the sequence: at left, the sequence of maxima (fluctuation 6%); at right, the spectrum of the sequence of maxima.*

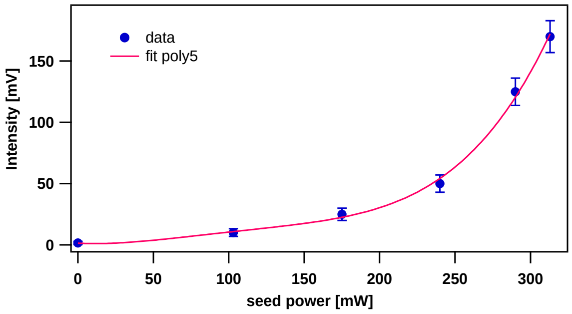

Figure 6.25: *Output power at 390 nm (second harmonic) vs. seed power.*

Dispersive section scans

In Fig. 6.26 we report the optimization of the dispersive section in order to enhance the harmonic signal. We found the optimum value around $R_{56} = 50\,\mu$m in both cases. Since the simulation gives $R_{56} \approx 0$, this discrepancy can be an indication of transverse misalignment or not perfect overlap. Over $R_{56} = 50$, the trend of the intensity shows that the stronger field causes beam overbunching.

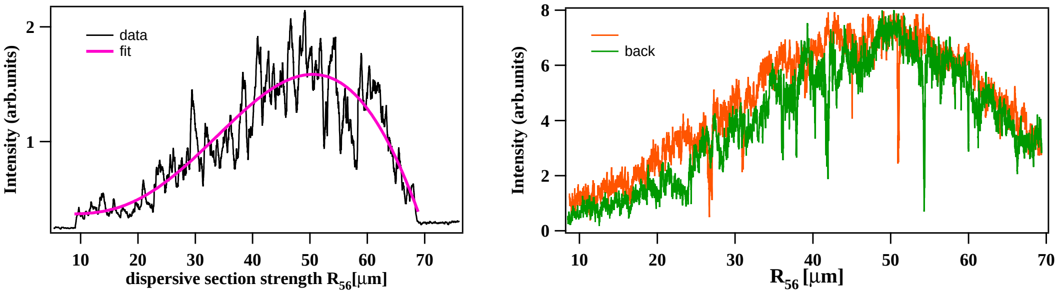

Figure 6.26: *Harmonic intensity (195 nm) vs. dispersive section strength.*

Scan with delay line

A "cross-correlation" measurement of the bunch length is shown in Fig. 6.27. This has been obtained moving the delay of the seed laser pulse with respect to the electron beam and hence seeding different portion of the bunch. The obtained result, a duration of 26 ps (FWHM), is in agreement with previous measurements performed with the streak camera at about the same current.

Spectral stability

Figure 6.28 a shows the very good spectral stability of the source. In the picture at left, the radiator is tuned at 198.5 nm, which is the second harmonic of the seed laser. In the picture at right, the radiator is tuned at 203 nm. The wavelength mismatch corresponds to 1% on the undulator parameter. As already explained, at the radiator entrance, the electrons are prepared to emit coherently at one of the seed harmonics. Coherent emission

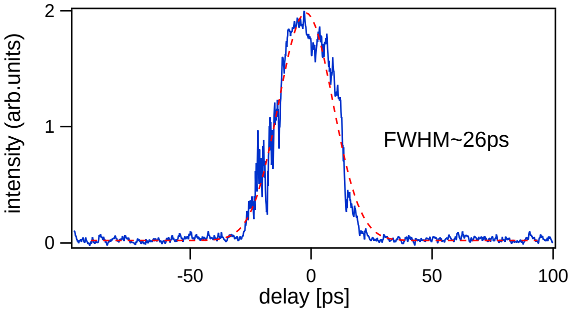

Figure 6.27: *Cross-correlation measurement of the bunch length.*

still occurs provided the relative mismatch does not exceed the FEL gain-width $\simeq 1/N$, N being the number of undulator period (see Eq. 1.41). The effect of the mismatch on the radiator emission is shown in Fig. 6.28 (right), where the measured spectrum is reported. As one can see, while the part of the spectrum generated by spontaneous emission is centered around the "detuned" wavelength (i.e. 203 nm), the position of the coherent signal is "locked" to the second harmonic of the seed laser. For the considered case, the mismatch is about 2.3%, which well within the FEL gain-width $1/N$=5%. After subtracting the background, the relative spectra are shown in Fig. 6.28 (bottom line).

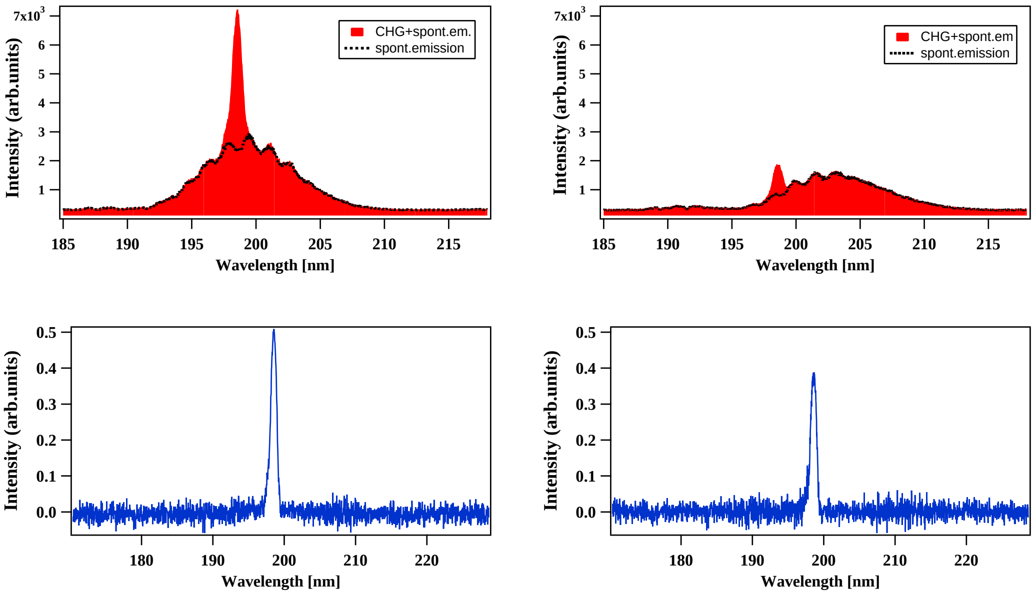

Figure 6.28: *Top: spectra at 198.5 nm. Bottom: corresponding background subtracted spectra (normalized). The difference between the pictures at left and at right is 1% on the undulator strenght.*

The experimental results have been submitted for pubblication togheter with the proof–of–principle experiment reported in Ch. 7.

6.2.5 Preliminary comparison: simulation vs. experiment

The estimation of number of photons per pulse has been done comparing the coherent signal with the spontaneous emission. The synchrotron radiation generated by one undulator has been estimated using `SPECTRA8.0`[3] for experimental conditions (beam energy, current, wavelength, polarization, ...).

This program gives the $Flux(ph./sec./0.1\%bw) = 10^{12}$. The relative bandwidth of one undulator is $\frac{\Delta\lambda}{\lambda} = \frac{1}{N} = \frac{1}{20} = 0.05 \rightarrow 5\%$. The number of photons per pulse is then $\frac{10^{12}\cdot 50}{10^6} = 5 \times 10^7$. The ratio between coherent harmonic signal and synchrotron radiation can be estimated either considering spectral measurement or PMT acquisition. We consider both cases and we compare the results.

Using spectral measurement:

$$\left(\frac{\#count_{peak|_\lambda}}{\#count_{bkg|_\lambda}} \cdot \frac{\nu_{synchr}}{rep.rate_{coher}}\right) \cdot \frac{Flux}{\nu_{synchr}} \cdot \frac{\Delta\lambda}{\lambda} \approx 0.9 \times 10^9 \qquad \text{for } 195\,\text{nm}. \tag{6.1}$$

Using PMT acquisition:

$$5 \times 10^7 \cdot \frac{50}{2} \approx 1 \times 10^9 \tag{6.2}$$

In Table 6.2 we summarize the the comparison between simulation and experiments. We report also the expected performance at 80 nm.

	$\Delta\lambda/\lambda$	pulse length	Photons/pulse
195 nm($\simeq 6.4\,eV$)			
simulation	3×10^{-3}	$\simeq 100\,fs$	3×10^9
experiment	4×10^{-3}	tb meas.	0.9×10^9
130 nm($\simeq 9.5\,eV$)			
simulation	2×10^{-3}	$\simeq 100\,fs$	2×10^9
experiment	4×10^{-3}	tb meas.	1×10^9
80 nm($\simeq 15.5\,eV$)			
simulation	$\simeq \times 10^{-3}$	$\simeq 100\,fs$	4×10^{10}

Table 6.2: *Comparison simulation vs. experiment. In the case of 195 nm and 130 nm, we considered beam current=0.7 mA and the seed laser at 390 nm. In the case of 80 nm, the current is 4 mA and the seed wavelength 260 nm.*

6.3 Even and odd harmonics studies

6.3.1 Motivation and experimental setup

Theoretical studies have been triggered by the need to estimate, and possibly control, the amount of power contained in the harmonics of the FEL fundamental wavelength. In the case of single-pass VUV/X-ray FELs, harmonic emission may have either a desirable or an undesirable effect. In some cases, it can be useful in order to extend the tunability range of FELs to shorter wavelengths, that otherwise would not be accessible [4]. In other cases, the harmonic radiation is considered as a noise source because it contaminates the radiation used for experiments, preventing a clear discrimination of investigated effects. As mentioned in previous chapters, in the case of high average power FEL oscillators, one is interested in suppressing harmonic radiation as much as possible. The reason for that is the damage that such a radiation may produce on the mirrors of the optical cavity.

In a FEL, the evolution of the electron beam density is driven by the field at the fundamental wavelength, which is orders of magnitude stronger than the harmonic fields. Harmonic bunching is the nonlinear source for harmonic generation, which is order of magnitudes stronger than the spontaneous incoherent emission [5, 6, 4]. In the case of SASE or oscillator FELs, harmonic emission is usually produced in the same undulator where the radiation at the fundamental wavelength is generated. We will refer to this process as nonlinear harmonic generation (NGH).

It has been demonstrated [5, 7] that, in the case of planar undulators, on–axis emission occurs exclusively at odd harmonics, while even harmonics are present only off–axis, and with some peculiar polarization properties [5, 8]. In this context, the possibility for helical undulators to generate significant coherent on–axis signal is still an open point.

In particular, a numerical prediction [9] indicates the existence of a strong coherent on–axis radiation at all the harmonics of the fundamental field. This is in disagreement with recent theoretical results, that predict no coherent on–axis emission [10].

An alternative approach to NHG for producing coherent harmonic emission is the harmonic generation with an external laser, described in this chapter, i.e. CHG.

The experimental setup used in this investigation is reported in Fig.6.29. A diaphragm of 1.4 mm is placed after 16 m from the second undulator, before the detector. The diaphragm is used to select only the portion of radiation emitted within a small cone close to the undulator axis (angular acceptance of the order of 0.09 mrad). By moving the diaphragm, it is possible to characterize the transverse distribution of the produced radiation. The monochromator and the PMT are located about 40 m downstream the radiator.

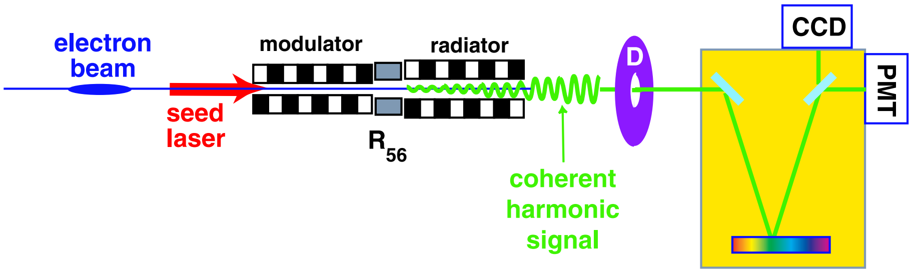

Figure 6.29: *Sketch of the experimental setup used for the investigation of harmonic generation. The produced coherent harmonic radiation passes through a diaphragm (D) and is transported into a diagnostic area, where temporal (PMT) and spectral (CCD) analysis are performed. The position of the diaphragm defines the angle of emission with respect to the undulator's axis considered for the measurement.*

As mentioned before, the Elettra optical klystron is very flexible and, depending on the undulator configuration, different harmonic generation schemes can be studied. The laser-electron interaction in the modulator produces bunching at odd and even harmonics. As a consequence, in the radiator, coherent emission occurs at any selected harmonics, no matter the modulator polarization. In this set of measurements, we use the second harmonic (about 400 nm) of the Ti:Sapphire laser.

The main experimental parameters are reported in Table 6.3.

Electron beam	
Energy	1.095 GeV
Energy spread	$\simeq 0.1\%$ $(\delta\gamma/\gamma)$
Revolution period	864 ns
Bunch length (ΔT_{bun})	35 ps (FWHM)
Peak current (I)	15-30 A
Seed laser	
Wavelength	399 nm
Power	5 GW
Pulse length (ΔT_{las})	120 fs (FWHM)
Polarization	horiz.– circ.
Repetition rate	1 kHz

Table 6.3: *Main CHG experimental parameters.*

6.3.2 Experimental results

Since the radiator is very short, the power generated in CHG and NHG configurations are similar, when NHG is feasible. The coherent signals obtained in CHG and NHG configurations are compared between them for different harmonic numbers and polarizations.

The third harmonic signals detected by the PMT in the case of CHG and NHG are reported in Fig.6.30a-b.

In both cases, the radiator is set for horizontal polarization.

Measurements have been done with a large aperture of the monochromator slits and, as a consequence, are not affected by the bandwidth of the detector, which is close to the that of the spontaneous emission ($\simeq$ 5nm).

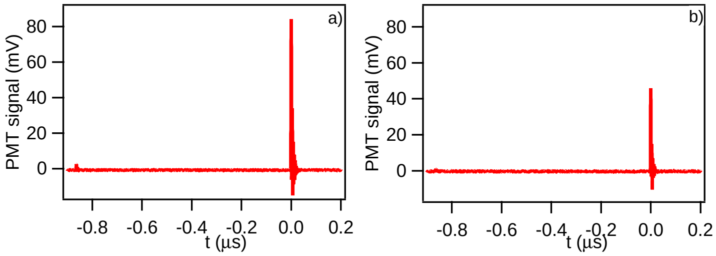

Figure 6.30: *Comparison between the third harmonic radiation produced in CHG (a) and NHG (b) configurations. In both cases the modulator and the seed laser are in horizontal polarization. The radiator is tuned to the third harmonic in horizontal polarization (a) and to the fundamental in horizontal polarization (b).*

As expected, the difference between the coherent signals produced with CHG and NHG is only a factor 2. However, as already mentioned, one of the most significant advantages of the CHG scheme with respected to NHG is the possibility to freely choose the harmonic and the polarization of the produced radiation.

We now investigate the possibility to produce on-axis harmonic radiation at even harmonics using NHG. According to theoretical predictions [5], the signal should be zero in the case of linearly polarized undulators. As already mentioned, the existence of a non-zero signal in the case of helical undulators is still an open question [11, 9, 12].

As expected, our measurements show that the second harmonic in planar undulator configuration is virtually zero (see Fig. 6.31c), i.e. about a factor 20 smaller than the signal measured in similar experimental condition using CHG (see Fig. 6.31a). In fact, such a small signal can be attributed to a contamination from off-axis radiation, due to nonzero dimensions of our diaphragm. Similar results have been found in the case of circularly polarized undulators, both for the second (Figs. 6.31b,d) and the third harmonics. Results presented in Fig.6.31 provide an experimental validation of the theoretical results reported in Ref. [12], that predict no harmonic coherent on–axis signal generated by helical undulators. As before, the small residual signal in Fig 6.31d can be considered as a contamination coming from off-axis radiation.

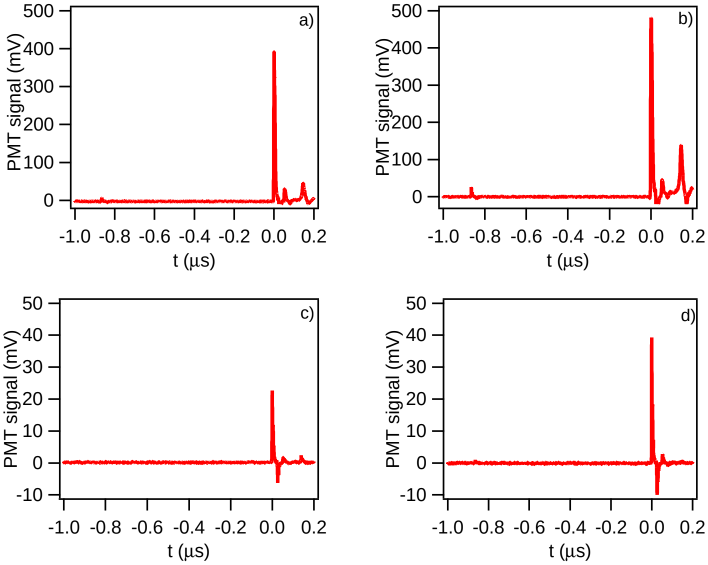

Figure 6.31: *Coherent harmonic signals produced at the second harmonic of the seed wavelength in CHG (a,b) and NHG (c,d) configurations. Figures (a,c) refer to a condition where the seed laser, the modulator and the radiator are in planar polarization, while Figs.(b,d) refer to a condition where both the seed and all undulators are set in circular polarization. Data reported in Figs.(a) and (c) refer to the same experimental conditions, and can be used for a relative comparison. The same holds for Figs.(b) and(d).*

In order to better characterize the process of harmonic generation, we also performed measurements of the spatial distribution of the coherent radiation for the case of the second harmonic produced by CHG and NHG. Measurements have been performed by moving the diaphragm in order to collect off-axis radiation on the PMT.

Figure 6.32 shows the intensities of coherent signals measured in the case of CHG (squares) and NHG (dots), as a function of the collection angle. It is important to note that, due to the relatively large aperture of the diaphragm (0.09 mrad), in the case of NHG one can expect a noticeable contamination coming from off-axis radiation. For that reason it is important to take into account the aperture of the diaphragm also for the

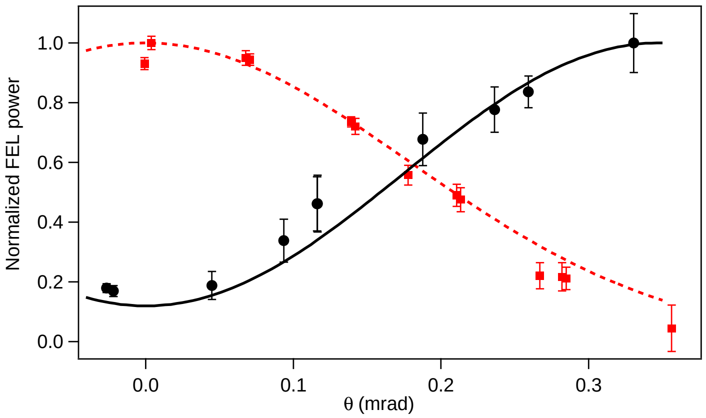

Figure 6.32: *Measured angular distribution of the second harmonic in the case of CHG (squares) and NHG (dots) with helical undulators. Measurements are well fitted by theoretical curves, which have been obtained by integrating the expected Gaussian profile (dashed line, CHG case) and the profile predicted in [12] (continuous line, NHG case), over an angle of* 0.09 *mrad.*

theoretical curves we want to use for fitting the data. The CHG data are well fitted by a function corresponding to the integration over a window of 0.09 mrad of a Gaussian beam profile with a divergence of 0.3 mrad (dashed line in Fig. 6.32). It is worth noting that a Gaussian beam with a divergence of 0.3 mrad correspond to a beam waist of about 200 μm, which is in agreement with the dimension of our electron beam. An indication of the goodness of the fit between experimental data and the theoretical curve is provided by the statistical analysis of our measurements. In the case of CHG, the reduced χ^2 error [13] is largely smaller than 1, i.e. $\chi^2 \simeq 0.04$.

The NHG data fit with the integration over the same window of the distribution function predicted in [12] for the second NHG in helical undulator. The theoretical curve (Fig. 6.32 continuous line) was calculated using the parameters of our experimental setup. In this case, the goodness parameter for the fit is $\chi^2 \simeq 0.06$.

It is important to note that the goodness fitting parameter χ^2 becomes larger if we consider the possibility to have together with the off-axis distribution [12] an on-axis Gaussian distribution. In particular the χ^2 becomes the double when fitting the data with a distribution that consider the presence of a Gaussian which is 10% of the off-axis distribution. The χ^2 become a factor 20 larger in the case the Gaussian is 20% of the off-axis distribution.

Spatial profiles with strong off-axis contents similar to the second NHG in helical polarization presented in Fig. 6.32 have been seen also for the second NHG in planar polarization and for the third NHG in helical polarization (data not shown).

In conclusion, the presented results for the nonlinear harmonic generation in helical undulators are in quantitative agreement with recent theoretical results [12], that predict no coherent harmonic emission on axis in helical undulators.

This work has been submitted for pubblication.

Bibliography

[1] http://pbpl.physics.ucla.edu/ reiche/

[2] G. D. Ninno *et al.*, *Nucl. Instr. and Meth. A* **507** 274-280 (2003)

[3] Takashi Tanaka and Hideo Kitamura, http://radiant.harima.riken.go.jp/spectra/

[4] S.G. Biedron *”et al.* Phys. Rev. ST AB **5**, 030701 (2002)

[5] M.J. Schmitt and C.J. Elliott, Phys. Rev. A **34**, 4843 (1986)

[6] R. Bonifacio, L. De Salvo and P. Pierini, Nucl. Instrum. Methods A **293**, 627 (1990)

[7] D.F. Alferov, Yu.A. Bashmakov and E.G. Bessonov, Sov. Phys. Tech. Phys. **18**, 1336 (1974).

[8] E.L. Saldin, E.A. Schneidmiller and M.V. Yurkov, Phys. Rev. ST AB **9**, 030702 (2006).

[9] H.P. Freund, P.G. O’Shea and S.G. Biedron, Phys. Rev. Lett. **94**, 074802 (2005).

[10] G. Geloni, E. Saldin, E. Schneidmiller and M. Yurkov, Opt. Commun. **271**, 207 (2007).

[11] B.M. Kincaid, J. of App. Phy., **48**, 2684 (1977).

[12] G. Geloni, E. Saldin, E, Schneidmiller and M. Yurkov, Nucl. Instr. Meth. A **581**, 856 (2007).

[13] J.R. Taylor, *”An Introduction to Error Analysis”*, University Science Books (1982).

Chapter 7

Proof–of–principle Experiments

In this chapter we briefly present the results obtained using the VUV ultra-short coherent pulses obtained in seeded "single-pass" configuration at the Elettra storage-ring FEL.

7.1

For many applications in condensed matter physics, as well as in photochemistry and atomic and molecular physics, going beyond 250 nm is critical in spectroscopic applications. Beyond this energy one overcomes the work function in most solids and in clusters of metals and metalloids, making it possible to eject electrons from the target into the vacuum with the optical excitation. It is not within the aim of this dissertation to overview the whole range of possible scientific applications opened by SRFEL and laser seeded SR CHG. Nonetheless a brief summary will be given of the principal expectations that the opening of such a source can bring to research groups active in the experimental sciences at the ELETTRA laboratory.

The small spectral width ($\Delta\lambda/\lambda \sim 10^{-6}$ in FEL mode, Fourier Transform Limited in seeded SR CHG) in conjunction with the high photon flux and the repetition rate (MHz or KHz in FEL or SR-CHG, respectively), can offer a unique instrument for high resolution and time resolved experiments. The time structure of the electron bunches (few bunch, single bunch) appears immediately suitable for time resolved analysis of particles resulting from photon-matter interaction (ions, electrons, photons). This is also fundamental in optimizing acquisition times and detection efficiency when in Time Of Flight techniques are adopted in investigations on low density systems, such as free clusters and metastable species in the gas phase. Besides spectroscopic investigation of electronic structure in gas phase and condensed matter physics (see e.g., [1]) many other applications are possible also in other disciplines, such as chemistry and biology.

Imaging techniques will obviously profit from the availability of radiation with high flux and higher coherence at shorter wavelength [2, 3]. Additionally spectroscopic and imaging techniques performed in a time-resolved manner in the ps-μs range (anisotropy decay, fluorescence spectroscopy, non-linear dynamics) can benefit from a coherent ultrafast radiation from the storage ring. The extraction of information on the dynamics both of the internal motion and of electronic excitations for systems like proteins, enzymes, nucleic acids (see e.g., [4]) is a wide area of contemporary science that continuously grows and requires cutting edge experiments where precise synchronization of different light sources is fundamental. The contemporary presence of fs laser source, coherent synchrotron light emitted by the EUFOS source and "conventional" synchrotron radiation present at Elettra represents a unique and fantastic opportunity not only for developing new experiments, but an entire user community that can fruitfully merge laser and synchrotron radiation scientists. Finally a VUV source of such high brightness could also be useful for non spectroscopic applications such as the study of thin film modification due to UV irradiation during growth, or applications to photo-lithography processes.

In the following paragraphs we briefly describe the first two experiments that have been carried out exploiting the present performance of the laser seeded CHG. We have decided to choose prototype experiments in the fields of molecular physics and of condensed phase photoemission. The experiments have been performed in collaboration with Users groups already operating at Elettra at the Gas Phase photoemission beamline and NanoSpectroscopy beamline, respectively, and that have shown interest in developing research programs that in the next future can fruitfully exploit the SR-CHG radiation.

7.2 VUV Photoionization Mass Spectrometry

Photoionization Mass Spectrometry is a widely used technique for characterization of the electronic structure of isolated systems in the gas phase. The EUFOS experimental program foresees a series of experiments on free clusters in collaboration with the Molecular Beam and Nanocrystalline Materials Laboratory coordinated by Prof. Paolo Milani (University of Milan, Italy). The new compact and portable apparatus specifically designed for spectroscopic experiments on free clusters at the Elettra storage ring is equipped with a Pulsed MicroPlasma Cluster Source and a linear Time Of Flight Mass Spectrometer (TOF/MS) installed inside the photon-cluster interaction chamber. The experimental set-up was successfully exploited on the Gas Phase Photoemission beamline at Elettra to obtain Near Edge X-ray Absorption Spectroscopy Fine Structure (NEXAFS) spectra of free Titanium clusters [5] and carbon clusters [6] by means of the PhotoElectron PhotoIon COincidence (PEPICO) Technique. A schematic of the experimental apparatus installed at the EUFOS end station is shown in fig. 7.1(a), whereas the TOF PEPICO set-up appears in fig. 7.1(b).

In the first ever attempted single photon photoionization measurement on a Storage Ring Free Electron Laser we have run a somehow simpler prototype experiment, in order to obtain the TOF mass spectrum of pyrimidine organic molecule. Pyrimidine was purchased from SigmaAldrich with a stated purity of >99%. At the working temperature of 295 K the sample is liquid and it was stored in a glass container connected to the ionization chamber through a stainless steel gas inlet system. After performing several freeze-pump-thaw cycles in situ to eliminate all traces of contaminants, a small flow of molecular vapor was let in the interaction region of the TOF mass spectrometer through an external leak valve. Experiments were performed when the target gas pressure in the chamber stabilized near $2{\cdot}10^{-5}$ mbar.

The Elettra electron bunch was seeded with photons at 398 nm from the Ti:Sa fs-laser. The CHG radiation obtained at 133 nm was used to ionize pyrimidine molecules within the plates of a TOF mass spectrometer. Pyrimidine as a target sample was chosen on the basis of its ionization potential, 9.3 eV, that perfectly matches the EUFOS radiation obtained seeding Elettra electron bunches with the second harmonic of the Ti:Sa laser.

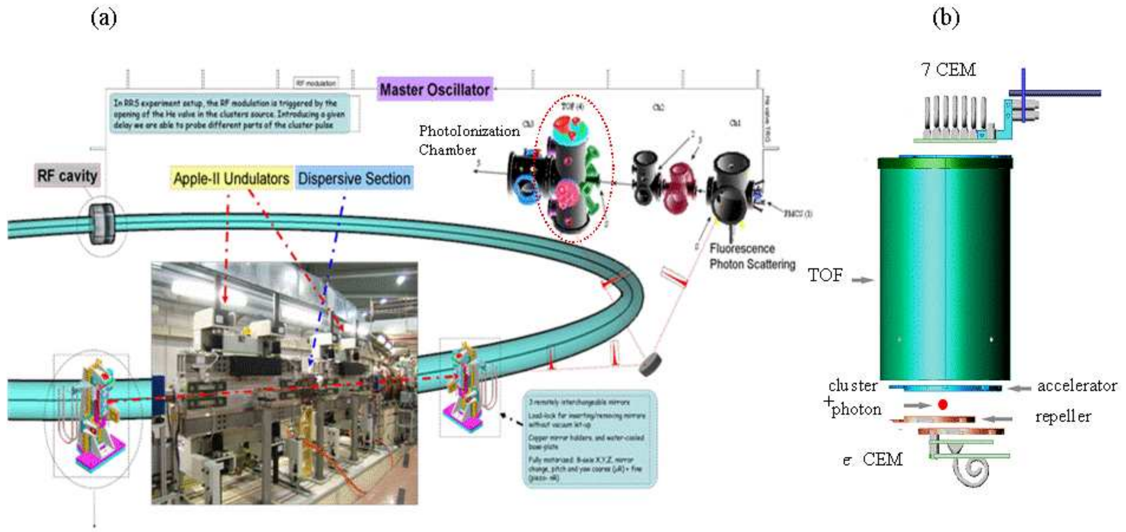

Figure 7.1: *Schematic of the Cluster Experiment with Synchrotron Radiation installed as the EUFOS end-station. (a) The set up is equipped with different vacuum chambers and allows for fluorescence and photoionization experiments on isolated systems in the Gas Phase. (b) View of the the PEPICO set-up contained in the PhotoIonization chamber.*

In this way we expected to obtain a clean mass spectrum were only the molecular parent peak is expected, since no internal energy can be left in the molecular ion that may induce further fragmentation processes [7]. Electron and Ions arrival times at the detectors have been recorded with a multi-hit Time-to-Digital Converter (TDC) electronic card and are shown in fig. 7.2(a). The signal ratio obtained from SR-CHG relative to spontaneous SR in this condition is 26. The pyrimidine ion mass spectrum can then be reconstructed with a software data analysis that correlates electron and ion coincidence hits [5] and it is shown in fig. 7.2(b).

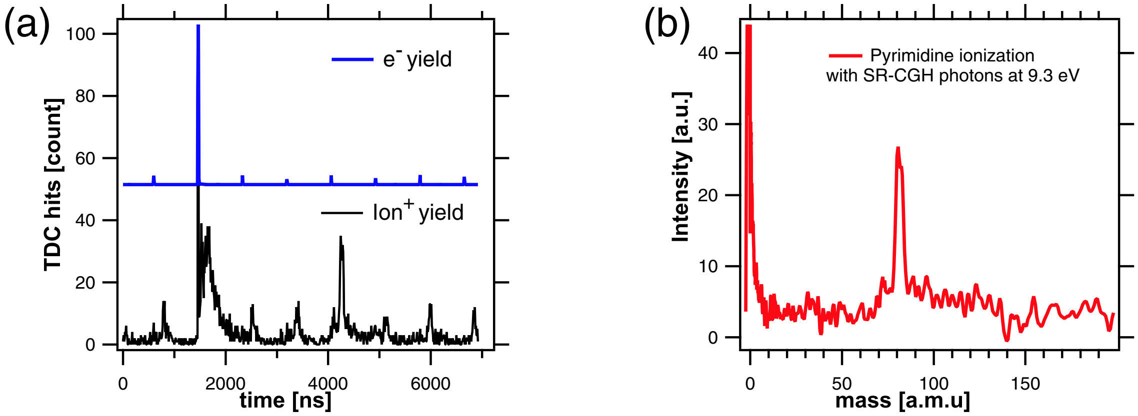

Figure 7.2: *TOF Mass Spectrum of Pyrimidine obtained with laser seeded CHG-SR at 9.3 eV. (a) signal acquired with the TDC from the electron and ion detectors as a function of time (b) Mass spectrum obtained from time correlation analysis of the TDC hits.*

The relatively low quality of the mass spectrum is not due to the low signal to noise ratio in the independent ion and electron channels, but to an unfortunate and not yet optimized synchronization of the TDC with the fs laser clock. The spectrum was obtained on the last day of the run, with the last available injection at Elettra on the 7th October 2007. A clear signal due the pyrimidine parent ion appears in the TOF spectrum at 79 a.m.u. and it clearly demonstrates the feasibility of photo-ionization experiments in the gas phase with the EUFOS source.

7.3 VUV PhotoElectron Microscopy

As it has been already mentioned, the availability of CHG sources is expected to bring great benefit in wide variety of disciplines, e.g. condensed matter, material science, plasma physics and chemistry. In particular, the time structure and intensity of CHG is attractive for the implementation of stroboscopic methods in photoelectron and imaging techniques. In particular, the use of ultra-short VUV and/or X-ray femtosecond pulses has tremendous potential in diffractive imaging microscopy, because it can tackle complex transient phenomena with femtosecond time resolution. The EUFOS source shares the undulator source with NanoSpectroscopy beamline that is equipped with two end-stations dedicated to photo-emission electron microscopy at Elettra.

A proof-of-principle spectro-microscopy experiment with CHG from the EUFOS source was attempted using photoemission electron microscopy, using one of the microscopes in operation at the NanoSpectroscopy beamline. This instrument, called SPELEEM (Spectroscopic Photoemission and Low Energy Electron Microscope) combines energy-filtered photoemission electron microscopy (PEEM) with micro-spectroscopy (micro-XPS), reaching a best energy resolution of about 0.2 eV and lateral resolution of few tens of nm. PEEM, which detects photoelectrons emitted from a specimen illuminated with UV-light or X-rays, can suffer from space charge problems. In the specific case of CHG, space charge results from the very high photoelectron yield at the microscope, resulting from to the high peak power of the source. Whereas CHG has never been employed in combination with PEEM, few examples of UV-FEL PEEM are reported. Using the DUKE-FEL at average power of few tens mW using photon energy in the range 3 to 6.3 eV, space charge did not hamper the PEEM performance [4, 8, 9, 10].

Another challenge of CHG-PEEM is the limited repetition rate of the source (1 kHz), at least compared to that of standard synchrotron radiation (1 MHz). In our PEEM experiments data acquisition was synchronous to the photoemission signal generated by seeded or non-seeded pulses. This was obtained by gating the multi-channel plate imaging detector at the CHG repetition rate. PEEM images were obtained by accumulating the signal from pulses at fixed time delay from the reference bunch marker. We have also considered the photoelectron yield generated by the non coherent radiator harmonics coming from the same electron bunch that experiences the laser seeding process. This contribution was evaluated performing acquisitions gated on the radiation generated from a single electron bunch without laser seeding and it was then subtracted from all the images acquired while laser seeding was on.

Valence band photoemission spectra of an epitaxially grown Ag thin film measured using CHG at 9.3 eV with circular polarization are shown in fig. 7.3a. The strong enhancement of the seeded signal results in a PES spectrum that is up to a factor of 36 more intense than that of SR when the modulator is set to the 3rd harmonic of the laser seed. The different contribution from seeded and non seeded synchrotron single bunch radiation are also shown. Fig. 7.3b shows an analogous spectra obtained from photoemission experiments performed with the 4th harmonic of the laser seed (12.4 eV), that confirms the expected decrease of the laser seeding efficiency when increasing the harmonic order of the radiation.

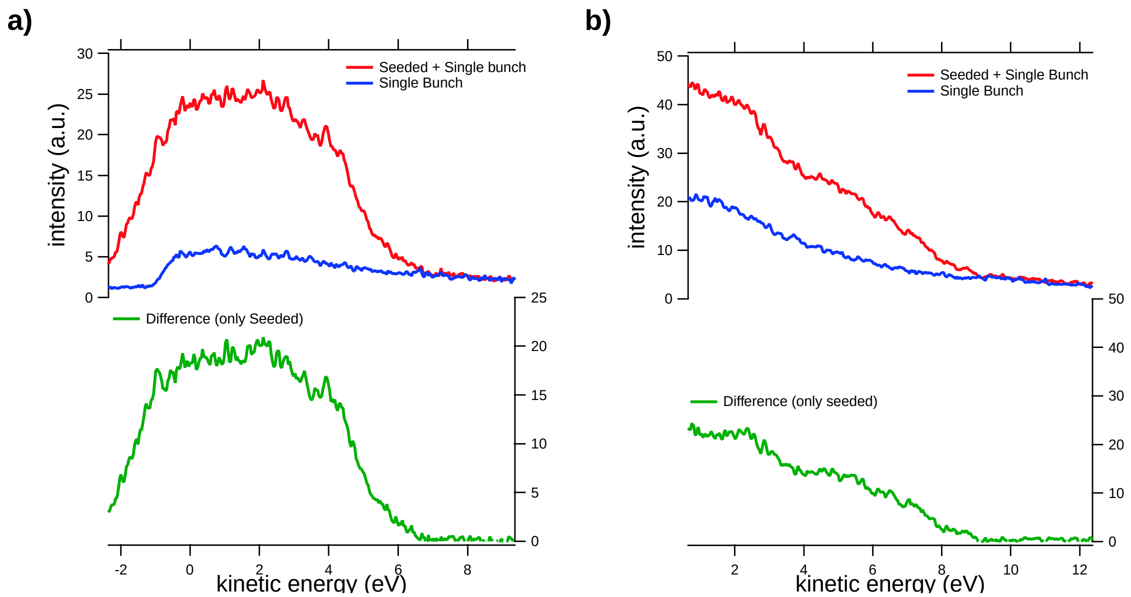

Figure 7.3: *PhotoEmission experiment on an Ag thin film illuminated with laser seeded SR, when the modulator gap is set to the 3rd harmonic (fig. a, 9.3 eV) and 4th harmonic (fig. b, 12.4 eV) of the radiator The different contribution from CHG and non coherent single bunch radiation are also show.*

To demonstrate CHG-PEEM imaging, we recorded topographic images of a patterned SiO2 sample. Fig. 7.4 shows PEEM images at field of view $20\,\mu$m, obtained using laser seeded synchrotron radiation (fig. 7.4a), only "normal" non seeded synchrotron radiation and the image resulting from the only CHR light (fig. 7.4c), respectively. In these images, the bright zones correspond to sidewalls of SiO2 pillars (height of 100 nm), which are illuminated at grazing incidence (16 degrees) by the photon beam. A quantitative comparison between the two images indicates similar values of the lateral resolution and thus proves feasibility of CHG-PEEM imaging, at least at intermediate lateral resolution.

Our results obtained with the SPELEEM photoemission microscope are obviously still very preliminary. Apparently, higher order contamination and a non negligible space-charge broadening affect their quality, thus requiring further and careful investigation before photoelectron microscopy with laser seeded SR can be applied routinely. Nonetheless a fundamental result has been achieved, that opens new horizons for microscopy experiments exploiting the femtosecond time resolution of the CHG source.

This proof–of–principle experiment togheter with the characterization of the source (discussed in Ch. 6) have been submitted for pubblication.

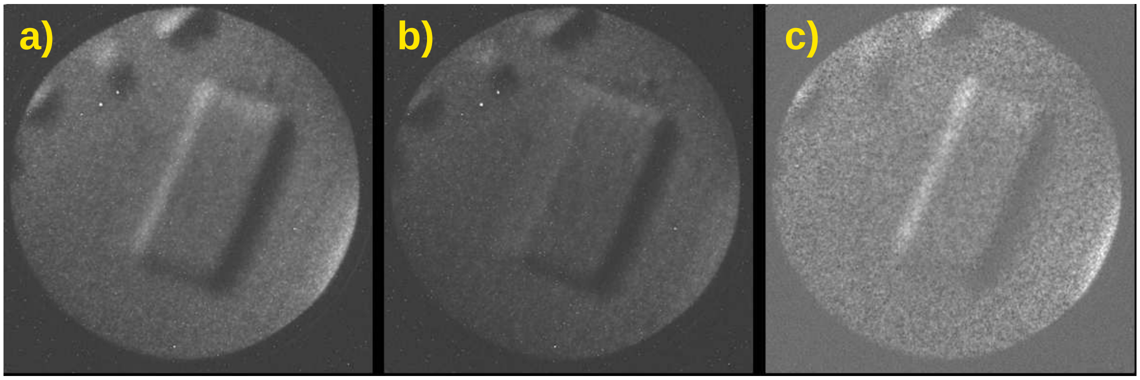

Figure 7.4: *Morphological image (scale bar is 5 μm) of a* SiO_2 *sample illuminated at 9.3 eV photon energy, with single bunch laser seeded synchrotron radiation (a), non seeded synchrotron radiation (b). Fig. c represents the image from pure CHG-SR photons, obtained through subtraction of Fig. b to Fig. a.*

Bibliography

[1] M. Marsi *et al.*, *Surface Review and Letts.* **9** (2002) 599

[2] Neutze, R., R. Wouts, D. van der Spoel, E. Weckert and J. Hajdu, *Nature* **406** (2000) 757; M. Giglio, M. Carpineti and A. Vailati, *Phys. Rev. Lett.* **85** (2000) 1416

[3] H. N. Chapman *et al.*, *Nature* **448** (2007) 676

[4] G. S. Edwards *et al.*, *Photochem. and Photobio.* **81** (2005) 711

[5] P. Piseri *et al.*, *New Journal of Physics* **8** (2006) 136

[6] P. Rudolf *et al.*, (2007) to be published

[7] M. Schwell, H. W. Jochims H. Baumgrtel, F. Dulieu and S. Leach, *Planetary and Space Sciente* **54** (2006) 1073

[8] A. Locatelli, L. Aballe, T. O. Mentes, M. Kiskinova, E. Bauer, *Surface and Interface Analysis* **38** (2006) 1554-1557, see also at: http://www.elettra.trieste.it/nanospectroscopy/microscope/SPELEEM.html

[9] W. C. Yang *et al.*, *Phys. Rev. Lett.* **90** 136102

[10] W. C. Yang *et al.*, *Phys. Rev. B* **69** 045421

Conclusions and perspectives

Harmonic Generation using Free-Electron Lasers is motivated by the fundamental and challenging need of generating good quality radiation in VUV/X-ray spectral region, beyond the reach of conventional light sources. Good quality means: high flux, spatial and temporal coherence, adjustable duration (great interest mainly to short - fs - pulses) and good stability. Achieving this challenging goal will provide the opportunity to open the path to more detailed investigations of many new areas of science.
Due to the lack of mirrors in VUV/X-ray spectral region, the standard approach relies on single-pass configurations, i.e. Self-Amplified-Spontaneous-Emission (SASE), Coherent Harmonic Generation (CHG) and High Harmonic Generation (HHG). CHG is based on the frequency up-conversion of a high-power seeding signal focused into an undulator, which is normally the first one of an optical klystron configuration, and synchronized with the incoming electron bunch. Contrary to SASE, CHG is capable of producing temporally and spectrally coherent pulses. When implemented on linear accelerators, both SASE and CHG are characterized by a poor shot-to-shot stability. Indeed, they show strong sensitivity to fluctuations of initial conditions, e.g., electron-beam energy, energy spread, current, emittance (and seed characteristics in the case of CHG). In linac-based devices fluctuations are in general quite strong.

Physics of single-pass free electron lasers has been studied theoretically for many years but very few experimental results are presently available (Desy for SASE and Brookhaven for CHG). On the other hand, many proposals and several funded projects exist to build such sources. So, there is a great interest in experimental results benchmarking theory and opening up new perspectives.

Motivated by the above considerations, we have performed a detailed experimental study of the CHG using a Free-Electron Laser. For this work, the FEL installed on the Elettra storage ring has been operated in two modes, both as oscillator and in seeded single-pass mode. The results show that a FEL based on a storage ring can be a competitive light source.

In oscillator configuration, a thorough investigation of several operational parameters has been performed in order to optimize the FEL dynamics in free-running mode. Diagnostics for light detection on different time scales has been also implemented. Giant pulses have been studied with two different Q-switch techniques (RF modulation and Chopper). The power increase in Q-switch mode allows to generate harmonic radiation. Simulations have been performed to study the coupled FEL-electron evolution.

In seeded configuration, the first part of the work has been devoted to the design of the experimental layout and the numerical study of expected performance. After this preliminary stage, we have installed the experiment, starting from housing the seed laser (a Ti:Sapphire laser) in a temperature-controlled room, until the implementation of the

synchronization system. Several shifts have been dedicated to the improvement of the spatial and temporal overlap before observing a first evidence of CHG. The first results of the generation of coherent pulses have been obtained at the third harmonic (265 nm) of the external seed. After the characterization of the source we have added a nonlinear crystal in the laser setup in order to generate the second harmonic and we have used this radiation as a seed to reach shorter wavelengths.
The work performed during the last year includes the signal optimization vs. adjustable parameters (e.g., beam current, seed power, seed pulse duration,seed repetition rate, dispersive section strength, electron beam energy, radiation polarization, ...), the study of the electron beam dynamics during coherent harmonic generation and the comparison between experiments and theory/simulations. Moreover, the coherent harmonic radiation at 130 nm has been utilized in two proof-of-principle experiments.
The Elettra FEL is nowadays the only coherent source able to provide ultra-short and stable radiation with variable polarization down to 99.5 nm (the fourth harmonic of the seed laser). The number of photons per pulse ($\sim 10^9$) exceeds by two order of magnitude the synchrotron emission and allows to use the coherent radiation obtained for experiment similar to those proposed for the fourth generation light sources. The light source we have implemented using the existing Elettra optical klystron can be easily extended to a wavelength range below 90 nm. Using different a seed laser (e.g. a parametric amplifier), we expect that it will also be possible to increase the tunability of the facility.

In conclusion, SRFELs are potentially powerful sources generating coherent radiation in the VUV/X-ray spectral region, as well as ideal test facilities for new generation light sources. This work provides important and new experimental results supporting to the idea of FELs as new generation light sources. We have demonstrated that seeded coherent harmonic generation on electron storage rings can significantly extend the potential of the presently available light sources, allowing to open new investigation realms in both basic and applied fields. Moreover, FELs belong to the very broad category of long-range interacting system and SRFELs are also intriguing nonlinear dynamical systems.

Appendix

Coherence of optical pulses

Longitudinal (temporal) coherence

The coherence length L_c is the maximum separation at wich a fixed phase relationship between the amplitudes of a wave at two different points is retained. The coherence length is related to the coherence time τ_c by $L_c = c\tau_c$. The coherence time is a measure of the monochromaticity of the light, since by Fourier transformation:

$$\tau_c \simeq \frac{1}{\Delta\nu_L} \quad \text{and} \quad L_c \simeq \frac{c}{\Delta\nu_L}. \tag{7.1}$$

The longitudinal coherence can be measured by means of a Michelson interferometer, which allows interference between waves at longitudinally different positions in a wavefront to be studied.

Transverse (spatial) coherence

The transverse coherence implies a definite fixed phase relationship between points separated by a distance L transverse to the direction of beam propagation. The transverse coherence length has a similar physical meaning to the longitudinal coherence length and is defined as:

$$L_{tc} \sim \frac{\lambda}{\theta_{beam}} \sim \pi\omega_0. \tag{7.2}$$

The spatial coherence can be demonstrated in a classic Young's slits interference experiment.

Fourier limit

Considering an electromagnetic wave with the field E defined as:

$$E(t) = E_0 e^{-\frac{t^2}{2\sigma^2}}, \tag{7.3}$$

the intensity is

$$I(t) = I_0 e^{-\frac{t^2}{\sigma^2}}, \tag{7.4}$$

with $FWHM_I^t = 2\sqrt{\ln 2}\sigma$. Performing a FFT of the electric field one obtains:

$$E(\nu) = E_0^\nu e^{-2\pi^2\sigma^2\nu^2} \tag{7.5}$$

and hence

$$I(\nu) = I_0^{\nu} e^{-4\pi^2\sigma^2\nu^2} \tag{7.6}$$

with $FWHM_I^{\nu} = \sqrt{\ln 2}/\pi\sigma$. The product of the temporal times the frequency part gives:

$$\Delta t \cdot \Delta\nu = FWHM_I^t \cdot FWHM_I^{\nu} = \frac{2\ln 2}{\pi} = 0.441 \tag{7.7}$$

where $\nu = c/\lambda$. The relation that will be used in the following chapters is:

$$c\Delta t \cdot \frac{\Delta\lambda}{\lambda^2} = 0.441 \tag{7.8}$$

where Δt and $\Delta\lambda$ are FWHM quantities and are measured respectively in s and m.

List of Figures

List of Tables